Nuclear Energy Research Initiative (NERI) Program
DE-FG03-99SF21922

An Innovative Reactor Analysis Methodology Based on a Quasidiffusion Nodal Core Model

Dmitriy Y. Anistratov[†],PI, Marvin L. Adams[‡], Todd S. Palmer[*], Kord S. Smith[**],Co-PI's,
Kevin Clarno[‡], Hikaru Hiruta[†], and Razvan Nes[*], graduate students

[†]Department of Nuclear Engineering, North Carolina State University
[‡]Department of Nuclear Engineering, Texas A&M University
[*]Department of Nuclear Engineering, Oregon State University
[**]Studsvik Scandpower, Inc.

Final Report

August 15, 1999 - December 31, 2002

Contents

1 Executive Summary **4**
- 1.1 Research Objectives . . . 4
- 1.2 Main Research Results . . . 4

2 Technical Summary **6**
- 2.1 Introduction . . . 6
- 2.2 Approximation of the Transport Solution by Form and Spectrum Shape Functions . . . 7
- 2.3 The Quasidiffusion Method for Solving the Transport Equation . . . 8
- 2.4 Improved Boundary Conditions for Assembly-Level Transport Calculations . 8
- 2.5 Homogenization Methodology and Consistent Spatial Coarse-Mesh Discretization for the Low-Order Equations of the Quasidiffusion Method . . . 9
- 2.6 Methodology for Solving the Low-Order Equations of the Quasidiffusion Method 10

3 Capturing The Effects Of Unlike Neighbors In Single-Assembly Calculations **12**
- 3.1 Introduction - The Interface Problem . . . 12
- 3.2 Reactor Analysis Methodology: Present And Proposed . . . 13
- 3.3 Results . . . 14
  - 3.3.1 Spatial Superposition of Colorsets . . . 14
  - 3.3.2 Albedo Boundary Conditions to Simulate the Effects of a Single Perturbed Neighbor . . . 18
  - 3.3.3 2D Albedo Boundary Condition Coupled with Spatial Superposition . 23
- 3.4 Conclusions . . . 26

4 Recent Improvements in Boundary Conditions for Single-Assembly Calculations **29**
- 4.1 Introduction . . . 29
- 4.2 Estimation of Albedo . . . 29
- 4.3 Results . . . 31
- 4.4 Summary . . . 32

5 Consistent Spatial Discretization of the Low-Order Quasidiffusion Equations on Coarse Grids **34**
- 5.1 Abstract . . . 34
- 5.2 Introduction . . . 34

5.3 The Few-Group Low-Order Quasidiffusion Equations . . . 35
5.3.1 The LOQD Equations . . . 35
5.3.2 Generation of Few-Group Data . . . 36
5.3.3 Fine-Mesh Transport Solution . . . 36
5.4 Coarse-Mesh Finite-Element Discretization Method for the LOQD Equations 37
5.5 Advanced Consistent Coarse-Mesh Discretization . . . 39
5.6 Numerical Results . . . 42
5.6.1 Test Problems that Simulate the Interaction of MOX and Uranium Assemblies . . . 42
5.6.2 Stability of Consistent Discretization to Variation of Group Data . . . 43
5.7 Conclusions . . . 44

6 Splitting Method for Solving the Coarse-Mesh Discretized Low-Order Quasidiffusion Equations 55
6.1 Abstract . . . 55
6.2 Introduction . . . 55
6.3 The Few-Group Low-Order Quasidiffusion Equations . . . 57
6.4 Splitting Method for Solving the LOQD Equations . . . 58
6.5 Calculation of Discontinuity Factors and Interface Conditions for Global Calculations . . . 60
6.5.1 Discontinuity Factors . . . 60
6.5.2 Interface Conditions . . . 61
6.6 Independent Coarse-Mesh Discretization of the LOQD Equations in Split Form 62
6.6.1 Discretization of the D-Problem Equations . . . 62
6.6.2 Discretization of the Q-Problem Equations . . . 64
6.7 Numerical Results . . . 65
6.8 Discussion . . . 68

7 A Coupled Nodal/Finite Volume Discretization of the 2D Quasidiffusion Low-Order Equations for Reactor Calculations 77
7.1 The Quasidiffusion Equations . . . 77
7.2 The Splitting Procedure for the Solution of the QDLO Equations in 2D . . . 79
7.3 Discretizing the "D" Problem: Extending the Advanced Nodal Discretization of Palmtag . . . 85
7.4 Discretizing The "Q" Problem: Applying the Finite Volume Methodology of Gol'din . . . 90
7.5 Testing the Nodal Methodology for the "D" Problem . . . 93
7.6 Testing the Coupled Methodology . . . 99

Chapter 1

Executive Summary

1.1 Research Objectives

The present generation of reactor analysis methods uses few-group nodal diffusion approximations to calculate full-core eigenvalues and power distributions. The cross sections, diffusion coefficients, and discontinuity factors (collectively called "group constants") in the nodal diffusion equations are parameterized as functions of many variables, ranging from the obvious (temperature, boron concentration, etc.) to the more obscure (spectral index, moderator temperature history, etc.). These group constants, and their variations as functions of the many variables, are calculated by assembly-level transport codes. The current methodology has two main weaknesses that this project addressed. The first weakness is the diffusion approximation in the full-core calculation; this can be significantly inaccurate at interfaces between different assemblies. This project used the nodal diffusion framework to implement nodal quasidiffusion equations, which can capture transport effects to an arbitrary degree of accuracy. The second weakness is in the parameterization of the group constants; current models do not always perform well, especially at interfaces between unlike assemblies. The project developed a theoretical foundation for parameterization and homogenization models and used that theory to devise improved models. The new models were extended to tabulate information that the nodal quasidiffusion equations can use to capture transport effects in full-core calculations.

1.2 Main Research Results

Improved Boundary Conditions for Assembly-Level Transport Codes: We have developed an extension of present-day reactor-analysis methodology that systematically accounts for the effects that different neighbors have on a given assembly's few-group constants. The new technique centers on energy- and angle-dependent albedos that simulate the effect of the unlike neighbors. Each set of albedos defines a branch case and thus fits into the framework of present-day methodology. The parameter varied in each new branch case is the fractional difference in the neighbor's concentration of an isotope or mixture. (The base case corresponds to a zero difference in all concentrations - an identical neighbor - which produces the usual reflecting boundary condition.) The key simplification is that the albedos are generated by a one-dimensional transport calculation with a homogenized assembly and

homogenized neighbor.

We have found that the albedo produced from 1D homogenized (1DH) calculations does an extremely good job of capturing the effects of different neighbors in the rather restricted case of lattices that are uniform in one direction (in which the only large-scale variation is in the other direction). In fully 2D problems, the 1DH albedos are accurate near the center of an interface but in general lose accuracy at corners. This loss of accuracy in the albedo produces large errors in corner-pin powers in the worst cases. We have found that very simple modifications to the 1DH albedos can dramatically reduce these large errors. This encouraging result has led us to pursue systematic (but simple) modifications that are theoretically sound and that produce very accurate results.

Our complete methodology relies on albedos to estimate the changes in few-group parameters that are induced by differences in a neighboring assembly's composition. Another part of the methodology is to assume superposition and thus build the change in a parameter by summing the partial changes from a variety of differences in a neighbor's composition.

Homogenization Methodology for the Low-Order Equations of the Quasidiffusion (QD) Method: We have developed a coarse-mesh discretization of the low-order QD (LOQD) equations that is consistent with the given fine-mesh differencing method for the LOQD equations in the sense that it preserves average values of the fine-mesh scalar flux over the given coarse cells as well as reaction rates, the first and second spatial Legendre moments of the fine-mesh scalar flux over coarse intervals, currents at edges of coarse cells, and the fine-mesh multiplication factor. All these facts are rigorous mathematical results. The definition of discontinuity factors has been derived. The resulting discretization scheme enables one to approximate accurately the large-scale behavior of the transport solution within assemblies.

The developed method can be applied to a general transport method as well, if this method preserves the particle balance. If a fine-mesh solution is obtained directly from a transport differencing method, and it is used to calculate spatially averaged cross sections and special functionals defined in the method, then the resulting coarse-mesh solution of the LOQD equations will be consistent with the given transport method. The reason is that the coarse-mesh scheme was derived by algebraically consistent discretization based on the discrete particle balance equation, and thus this scheme works also for any transport method whose solution satisfies the discrete balance equation.

The developed coarse-mesh algorithm can be coupled with other parts of a complete reactor analysis methodology (generation of tables of constants, interpolation using tables, pin-power reconstruction).

Numerical Method for Solving QD Low-Order Equations: We have developed a splitting method that can efficiently solve coarse-mesh discretized low-order quasidiffusion (LOQD) equations. The LOQD problem can reproduce exactly the transport scalar flux and current. The developed method splits the LOQD problem into two parts: (i) the D-problem that captures a significant part of transport solution in the central parts of assemblies and can be reduced to a diffusion-type equation, and (ii) the Q-problem that accounts for the complicated behavior of the transport solution near assembly boundaries. Independent coarse-mesh discretizations are applied: the D-problem equations are approximated by means of a finite-element method, whereas the Q-problem equations are discretized using a finite-volume method. Numerical results demonstrate the efficiency of the presented methodology.

Chapter 2

Technical Summary

2.1 Introduction

The overall goal of the proposed project is to make significant specific progress toward the next generation of methods for the analysis of nuclear reactors. While there are many aspects of present-generation methods that could be improved, we focused upon two areas – the full-core few-group diffusion-like calculation and the assembly-level many-group transport calculation – and upon the interface between them.

Present-day methods use few-group nodal diffusion approximations to calculate full-core eigenvalues and power distributions. Nodal diffusion equations contain "group constants" – few-group cross sections, diffusion coefficients, and discontinuity factors. Group constants are modeled as simple functions of many parameters (such as boron concentration, fuel temperature, etc.), each of which is either input to the full-core calculation or estimated during it. These group constants and their variations as functions of the many parameters are created from assembly-level calculations that solve two-dimensional transport problems. Given this background, we can re-state our specific objectives as follows: *(1) Create a full-core few-group coarse-mesh diffusion-like method that will produce essentially the same results as a full-core many-group fine-mesh transport calculation. (2) Create a methodology that permits single-assembly transport calculations to construct all information that the full-core calculation needs to achieve the first goal.*

Present-day reactor-analysis methodology has two main weaknesses that keep it from performing at the high standards indicated by our objectives. One weakness is the diffusion approximation in the full-core calculation, which can cause significant errors at interfaces. We overcame this weakness by putting *quasidiffusion* equations into the nodal diffusion framework, allowing full-core calculations to capture transport effects to an arbitrary degree of precision. The second weakness is in the simple models used to "functionalize" the group constants; many of the current models do not always perform well, especially at interfaces between unlike assemblies, and those that seem to perform well lack a sound theoretical foundation. In this project we developed a theoretical foundation for these functional models, use that theory to assess current models, and further use it to devise improved models. The new models were extended to provide information that the nodal quasidiffusion equations need to capture transport effects in full-core calculations.

There is strong incentive for a reactor analysis methodology to require only single-

assembly calculations from its assembly-level many-group transport calculations. If multi-assembly "colorsets" are required, the amount of data that must be stored becomes much larger and bookkeeping becomes cumbersome. Reactor analysts greatly prefer a methodology that stores one table of group constants for each type of fuel assembly; this is why we have specified "single-assembly" calculations in our second main objective above. The restriction to single-assembly transport calculations places a significant burden upon the methodology: the effects of an unlike neighboring assembly upon a given assembly's group constants must be accurately estimated without knowledge of the neighbor. Capturing such "interface effects" is one of the major challenges that we addressed in this project.

Main results of this NERI project were published in the proceedings of the following ANS conferences [1-8]: *2000 ANS Winter Meeting*, Washington DC; *Int. Conf. on the New Frontiers of Nuclear Technology: Reactor Physics, Safety and High-Performance Computing (PHYSOR 2002)*, Seoul, Korea, Oct. 7-10 (2002); *Nuclear Mathematical and Computational Sciences: A Century in Review - A Century Anew*, Gatlinburg, Tennessee, April 6-11, 2003; *2003 ANS Winter Meeting*, New Orleans. The latest results will be submitted this year for publication in *Nuclear Science and Engineering* and proceedings of *PHYSOR 2004* (Chicago).

2.2 Approximation of the Transport Solution by Form and Spectrum Shape Functions

Let us define: $\varphi_g(\vec{r})$ as a fine-mesh fine-group transport scalar flux, $\varphi_G(\vec{r}) = \sum_{g\in G} \varphi_g(\vec{r})$ as a fine-mesh few-group transport solution, $\Phi_G(\vec{r})$ as a coarse-mesh few-group transport solution. Then, we have:

$$\varphi_g(\vec{r}) = \Phi_G(\vec{r}) \frac{\varphi_G(\vec{r})}{\Phi_G(\vec{r})} \frac{\varphi_g(\vec{r})}{\varphi_G(\vec{r})}. \tag{2.1}$$

$F_{spec} = \varphi_g/\varphi_G$ is a spectrum shape function that often depends only weakly on position within a single assembly. The form function $F_{form} = \varphi_G/\Phi_G$ is a detailed fine-mesh solution superimposed upon coarse-mesh shape. It is often depends weakly on neighbors, etc.. The spectrum and form functions are generated by single-assembly transport calculations as functions of various parameters that affect them. Current methods perform their single-assembly calculations with reflective boundary conditions, which effectively means that an assembly is surrounded by an infinite sea of identical assemblies. This makes it difficult to obtain the form and spectrum functions that will be accurate if in the full core there is a neighboring assembly that is significantly different.

We addressed this difficulty by using more general boundary conditions in the single-assembly calculations, thus removing the approximation of identical neighbors. Part of the research was to determine how best to do this. We used energy- and angle-dependent albedo boundary conditions. If the albedo boundary conditions capture the effects that different neighbors have on the form and spectrum shape functions, and if the full-core calculations obtain the correct leakage at node surfaces, then the result should be a very accurate analysis method.

2.3 The Quasidiffusion Method for Solving the Transport Equation

The proposed methodology is based on the quasidiffusion (QD) method for solving the transport equation. The basic idea behind the QD method is to effectively reduce the dimensionality of the problem by averaging the transport equation over angular and energy variables. The QD system of equations is closed by special linear–fractional functionals that depend weakly upon the transport solution. The resulting nonlinear problem of the QD method is equivalent to the original linear transport problem. The moment QD equations can be reduced to equations whose structure is similar to that of the diffusion equations. These features of the QD method make it a natural and efficient approach for developing reactor core analysis methodology based on transport theory and for implementation of it in the framework of existing diffusion theory codes. The QD approach has been successfully used to solve multigroup neutron transport equation with anisotropic scattering and fission, problems of reactor kinetics, burnup, and radiative hydrodynamics.

2.4 Improved Boundary Conditions for Assembly-Level Transport Calculations

We have developed extensions of present-day reactor-analysis methodology that systematically account for the effects that different neighbors have on a given assembly's few-group constants. One extension is branch cases that generate the effect of unlike neighbors on a given assembly's group constants. Another extension is to use superposition of the effects of neighboring assemblies to reduce the number of branch calculations that are needed to tabulate the effects of all possible neighbor permutations. Finally, we also use energy-, angle-, and position-dependent albedos to simulate the presence of the unlike neighbors in our branch calculations. We have developed and tested a procedure for efficiently estimating these albedos.

We envision two neighbor-assembly branches for each type of neighboring assembly, one for an adjacent configuration and one for diagonal. For each type and configuration we further envision a small number of branches on the neighbor's burnup and one branch with the neighbor containing a control rod. Other branches might be necessary in some applications. For each branch case we estimate an albedo and perform a single-assembly calculation; this fits into the framework of present-day methodology. (The base case corresponds to all identical neighbors - which produces the usual reflecting boundary condition.) The keys to computational efficiency are rapid estimation of albedos, the use of superposition, and keeping the number of branch cases reasonably low. The keys to accuracy are accurate estimation of albedos and careful attention to the limits of the superposition approximation.

We have found that spatial superposition of the effects of adjacent and diagonal neighbors provides an excellent approximation to the effects of multiple neighbors on the assembly cross sections and the diagonal (xx and yy) Eddington-tensor components. There is a large relative error in the superposition approximation of the very small off-diagonal (xy) component, the significance of which has not yet been determined.

We have found that the albedos produced from 1D homogenized calculations do a reasonably good job of capturing the effects of a different neighbor except near assembly corners, although it appears likely that explicit representation of the water gap will add enough accuracy to warrant its complexity. We have devised a 2D homogenized diffusion approximation combined with a fixed-source long-characteristics transport sweep to obtain 2D correction factors for the 1D albedo. This does not cause the off-diagonal tensor component to be accurate, but it does improve the cross sections and diagonal tensor components. Our estimated albedos produce significant improvements over the reflecting condition, but we believe that further significant improvement is possible, and we are actively pursuing such improvement.

We are currently working to couple our assembly-level results with full-core quasi-diffusion calculations to assess the impact of the errors that remain in our cross sections and Eddington tensors. If this assessment shows that further assembly-level improvements will noticeably improve the accuracy of the overall methodology, then we believe we can accomplish these improvements, beginning with simple improvements to our albedo boundary conditions.

In summary, we believe the new methodology described here is promising, and we expect to continue to refine it, couple it to other pieces of a full reactor-analysis system, and test the coupled system.

2.5 Homogenization Methodology and Consistent Spatial Coarse-Mesh Discretization for the Low-Order Equations of the Quasidiffusion Method

We have developed a high-order coarse-mesh finite-element method for discretization of the QD low-order equations that is consistent with the given fine-mesh transport differencing method in the sense that it preserves the fine-mesh values of cell-average scalar flux, cell-edge current, multiplication factor, and reaction rates. On the basis of this method, we have developed an advanced consistent coarse-mesh finite-element method that preserves extra two spatial Legendre moments of the fine-mesh transport scalar flux over coarse-mesh cells. All these facts are rigorous mathematical results. The definition of discontinuity factors has been derived. The resulting discretization scheme enables one to approximate accurately the large-scale behavior of the transport solution within assemblies.

The developed method can be applied to a general transport method as well, if this method preserves the particle balance. If a fine-mesh solution is obtained directly from a transport differencing method, and it is used to calculate spatially averaged cross sections and functionals, then the resulting coarse-mesh solution of the LOQD equations will be consistent with the given transport method. The reason is that the coarse-mesh scheme was derived by algebraically consistent discretization based on the discrete particle balance equation, and thus this scheme works also for any transport method whose solution satisfies the discrete balance equation.

We have analyzed the developed methods on a set of test problems that simulate the interaction of MOX and uranium assemblies. These tests included assemblies with enrichment variations, and water holes that introduce within-assembly flux variations. In spite of this the CMFE-2 method is able to generate solution that mimic accurately the large-scale

behavior of the transport solution within assembly.

The proposed methodology can be extended to multidimensional geometries, multigroup case, finite-element methods based on higher order expansions of the coarse-mesh scalar flux that creates an option of preserving more spatial moments of the fine-mesh transport solution over coarse cells. The developed method is a part of a new methodology for reactor core calculations, and this method will be coupled with other pieces of this methodology, including usage of group data obtained by means of single-assembly calculations that use efficient albedo boundary conditions. Another important issue is possibility of improvement of pin-power reconstruction using the discretization methods that preserve extra spatial moments of the fine-mesh transport solution within assembly. We are working now on such extensions.

2.6 Methodology for Solving the Low-Order Equations of the Quasidiffusion Method

We have developed a splitting method to solve the coarse-mesh discretized LOQD equations. The method effectively splits a problem into two parts. The D-problem captures a significant portion of the transport solution in the central part of assembly, and the Q-problem accounts for the complicated behavior of the transport solution in the vicinity of assembly boundaries. The calculation of discontinuity factors for the splitting method has been introduced, and corresponding interfacial conditions have been formulated for this particular method. Each part of the LOQD equations in the split form has been approximated by a different discretization scheme. The D-problem equations were approximated by means of the high-order finite element method. The Q-problem equations were discretized by using a finite volume method with second-order accuracy. Numerical results showed high accuracy of the proposed splitting method with the considered independent discretization of the equations of D- and Q- problems.

The successful performance of the splitting method in 1D geometry stimulates the efforts in extension of this method to multidimensional geometries. In 2D and 3D cases the solution of the LOQD equations discretized with high-order methods is rather computationally intensive problem. According to the proposed approach, one can split the LOQD problem into a D-problem that can be solved with current efficient methodologies for diffusion-type of equations and a Q-problem that can be discretized with a second-order finite-volume method because the solution of this problem is a small correction to solution of D-problem. Special interface conditions allow spatial decomposition of the Q-problem such that it can be solved in each coarse cell (part of assembly) independently of other cells. Thus, the presented splitting method enables us to reduce significantly computational costs for obtaining solution that very accurately accounts for transport effects in full-reactor calculations.

It is important to note that the proposed splitting method can be also utilized to upgrade current codes for full-reactor core calculations that are based on the diffusion theory. In such case, it is necessary to add solution of Q-problem and modify the definition of the diffusion coefficient as well as of the fission source term to account for the Q-problem solution. As a result, one gets a code based on transport theory calculations, provided that all extra group data and functionals are supplied from assembly-level calculations.

Bibliography

[1] D.Y. Anistratov and M.L. Adams, "Consistent Coarse-Mesh Discretization of the Low-Order Equations of the Quasidiffusion Method," *Trans. Am. Nucl. Soc.,* **83**, 250-251 (2000).

[2] K. T. Clarno and M. L. Adams, "Improved Boundary Conditions for Assembly-Level Transport Codes," *Int. Conf. on the New Frontiers of Nuclear Technology: Reactor Physics, Safety and High-Performance Computing (PHYSOR 2002)*, Seoul, Korea, Oct. 7-10 (2002).

[3] R. Nes and T. S. Palmer, "An Advanced Nodal Discretization for the Quasi-Diffusion Low-Order Equations," *Int. Conf. on the New Frontiers of Nuclear Technology: Reactor Physics, Safety and High-Performance Computing (PHYSOR 2002)*, Seoul, Korea, Oct. 7-10 (2002).

[4] D. Y. Anistratov, "Homogenization Methodology for the Low-Order Equations of the Quasidiffusion Method," *Int. Conf. on the New Frontiers of Nuclear Technology: Reactor Physics, Safety and High-Performance Computing (PHYSOR 2002)*, Seoul, Korea, Oct. 7-10 (2002).

[5] K. T. Clarno and M. L. Adams, "Capturing the Effects of Unlike Neighbors In Single-Assembly Calculations," *Nuclear Mathematical and Computational Sciences: A Century in Review - A Century Anew*, Gatlinburg, Tennessee, April 6-11, 2003.

[6] H. Hiruta, D. Y. Anistratov, and M. L. Adams, "Splitting Method for Solving the Coarse-Mesh Discretized Low-Order Quasidiffusion Equations," *Nuclear Mathematical and Computational Sciences: A Century in Review - A Century Anew*, Gatlinburg, Tennessee, April 6-11, 20 pp., 2003.

[7] D. Y. Anistratov, "Consistent Spatial Discretization of the Low-Order Quasidiffusion Equations on Coarse Grids," *Nuclear Mathematical and Computational Sciences: A Century in Review - A Century Anew*, Gatlinburg, Tennessee, April 6-11, 20 pp., 2003.

[8] K. T. Clarno and M. L. Adams, "Recent Improvements in Boundary Conditions for Single-Assembly Calculations," *Trans. Am. Nucl. Soc.,* **89**, (2003) (to appear).

Chapter 3

Capturing The Effects Of Unlike Neighbors In Single-Assembly Calculations

3.1 Introduction – The Interface Problem

One of the main challenges that a reactor analysis methodology faces is obtaining the power distribution and averaged cross sections for an assembly whose neighboring assemblies are significantly different. If the neighbors are identical to the assembly in question, then an excellent approximation to the solution in the assembly can be obtained by solving a two-dimensional single-assembly problem with reflecting boundaries. However, if a neighboring assembly is significantly different, the reflecting boundary condition does not accurately model reality.

Reactor analysts have tried many different approaches to approximating the effects of unlike neighbors on an assembly's averaged cross sections. The most straightforward is to run multi-assembly calculations ("colorsets"), one for each four-assembly permutation that will appear in the core [1,2]. While straightforward in principle, this approach is computationally unwieldy, taxing to the user, and it does not eliminate the need to branch and interpolate on conditions in the neighboring assemblies. Thus, most analysis systems attempt to retain the single-assembly calculation and somehow account for the effects of different neighbors.

In this chapter we describe our recent efforts to capture and tabulate the effects of different neighbors on the important parameters of a given assembly. This includes all parameters needed by the core-level *quasi-diffusion* equations that are described in other chapters. We describe our algorithms and present results from many difficult test problems containing MOX and UO_2 assemblies.

Part of the assembly-level methodology described here is to use the following detailed angle- and energy-dependent albedo boundary conditions to represent the effects of an unlike neighbor:

$$\psi_g(\underline{r}_s,\underline{\Omega}) = \gamma_g(\underline{r}_s,\underline{\Omega})\psi_g(\underline{r}_s,\underline{\Omega}'),\ \underline{\Omega}' \circ \text{ exiting direction that reflects onto } \underline{\Omega}. \quad (1)$$

Here ψ is angular flux and γ is our specialized albedo. (A *general* albedo function would relate each incoming $(g,\underline{\Omega})$ to *all* outgoing $(g',\underline{\Omega}')$.) While albedo boundary conditions have been explored before, our approach is different and offers several advantages, as we describe below. Another part of our system is to invoke superposition to estimate the combined effects of the

eight neighboring assemblies that surround a given assembly. In this paper we carefully study the accuracy of the superposition approximation, independent of the accuracy of any albedo boundary conditions.

In the next section we explain the core-level quasi-diffusion approach to reactor analysis and the data requirements that this approach places upon the assembly-level code. In a subsequent section we describe the results of our multiple analyses. Part of this is a study of the use of superposition of effects of unlike neighboring assemblies, which can significantly reduce the number of required analyses. We also study an albedo approximation that simulates the effects of neighbors in a representative set of colorsets. We then provide the results from an analysis that combines spatial superposition and our albedo approximation of the boundary condition. The final section contains a summary and draws conclusions.

3.2 Reactor Analysis Methodology: Present And Proposed

Today's reactor-analysis methodology is reasonably accurate, despite the use of reflecting boundaries for single-assembly calculations and two-group coarse-mesh diffusion for core-level calculations. Even on the most difficult commercial-reactor problems, the current methodology produces pin-power distributions that err by only a few percent [3,4]. This suggests that radical changes in the methodology are not needed; rather, we should carefully extend the existing methodology to try to capture most of the effects of different neighbors in our assembly calculations and most of the transport effects in our core-level calculations. This should eliminate most of the error in today's calculations.

Today's methodology employs single-assembly calculations to generate "base-case" few-group constants (cross sections, diffusion coefficients, and discontinuity factors), where "base-case" means a given set of parameters such as temperatures, power density, soluble boron or void concentration, etc. The variation of the constants with respect to changes in each parameter is estimated by solving one or more "branch cases" for each parameter. In a branch case on soluble boron concentration, for example, all other parameters are held at their base values, the boron concentration is changed, and the single-assembly calculation is performed. A branch on parameter p generates an estimate of dC/dp for each few-group constant C. The parameters that are tabulated are those that are needed to perform the core-level calculation and to reconstruct pin-by-pin powers.

In this chapter we describe the single-assembly portion of a larger effort to develop an improved reactor-analysis methodology that is a natural extension of today's methodology. The larger effort replaces the core-level diffusion calculation with a core-level *quasi*-diffusion (QD) calculation.[3-5] QD uses diffusion-like equations that contain transport information in the form of "Eddington" tensors; if the correct tensors are used, then the QD equations yield the correct transport solution. In 2D problems, each component of the tensor is an angular-flux-weighted average of the product of two direction cosines:

$$E_{uv}(\vec{r}) = \frac{\int_{4p} \Omega_u \Omega_v \psi(\vec{r},\Omega)\, d\Omega}{\int_{4p} \psi(\vec{r},\Omega)\, d\Omega}, \quad u = x \text{ or } y, \quad v = x \text{ or } y. \tag{2}$$

Thus, in addition to the usual few-group cross sections and discontinuity factors, our new single-assembly methodology must generate appropriately averaged Eddington tensors to prepare for later core-level QD calculations.

Our new single-assembly methodology also adds branch cases on parameters that describe the difference between the given assembly and its neighbors. Each branch case will be a single-assembly calculation with albedo boundary conditions that represent the effects of the unlike neighbor, either adjacent or diagonal to the given assembly. The result will be the same type of dC/dp values as are currently generated; there are simply additional p's to consider, p's that describe the unlike neighboring assemblies.

3.3 Results

The most difficult real-world commercial LWR problems involve LEU assemblies interspersed with MOX assemblies. We have considered several such problems to test our new methodology. We first explore the possibility of superimposing the effects of a single unlike neighbor to represent the effects of multiple unlike neighbors. We then test a two-dimensional albedo that we have developed to approximate the effects of a single unlike neighbor, either adjacent or diagonal to the current assembly. Finally, we combine the albedo boundary condition with the superposition approximation and test the ability of the resulting complete methodology to capture the effects of a set of unlike neighbors.

All of our two-dimensional transport results were obtained with a modified version of TALC, a long-characteristics assembly-level transport code written previously at Texas A&M University [5,6]. Each TALC calculation employed 12 flat-source regions per pin cell, 16 energy groups, 4 polar angles, 8 azimuthal angles per quadrant, and 0.5-mm spacing between rays. Each assembly in our test problems was a uniform lattice of geometrically identical pin cells – there were no water holes. Macroscopic cross sections were calculated from a pin-cell analysis using CASMO-3. The UO_2 fuel pins are all 4.0% enriched. The MOX assembly contains an enrichment grading that ranges from 6% to 10% in total Pu content. The corner pins had 6%, the outer rows had 8%, and the interior had 10%. The circular pins were represented exactly.

3.3.1 Spatial Superposition of Colorsets

In a "colorset" analysis, an assembly-level calculation is performed for each four-assembly permutation that will appear in the core. Each calculation requires up to ten times the CPU time of a single-assembly calculation and more input from the user. We propose to use spatial superposition of the effects of single unlike neighbors to approximate the effects of multiple unlike neighbors and thus reduce the number of calculations that are needed to cover the entire parameter space of neighboring assemblies.

3.3.1.1 Superimposing the effects of perturbed neighbors

For each assembly in the core, a "base" calculation of the current assembly is performed using reflecting boundaries to determine the "base" few-group constants (C_{base}). Suppose for the moment that we were willing to perform colorset calculations. Then only a single "colorset" calculation, with three of the given assemblies and one unlike neighbor, would be needed in order to determine the effects of a UO_2 neighbor on an adjacent MOX assembly (red underline in Figure 3.1) as well as a diagonally opposite one (blue italics in Figure 3.1). That is, one such colorset calculation would yield the change in few-group constants due to an adjacent neighbor $(dC/dp)_{adjacent}$ and the change due to a diagonal neighbor $(dC/dp)_{diagonal}$.

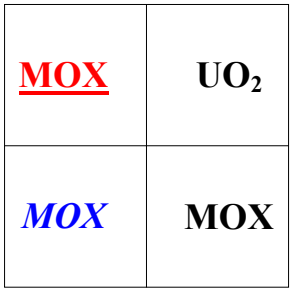

Figure 3.1 The basic colorset for determining direct effects of a UO_2 on a MOX assembly.

To estimate the effects of multiple perturbed neighbors, we would like to invoke superposition of the effects of single-assembly perturbations. To test the validity of such a superposition we consider three two-dimensional test configurations, as shown in Figure 3.2. For instance, if a given assembly were surrounded by unlike assemblies (an isolated configuration), then the formula to determine the few-group constants would be:

$$C_{isolated} = C_{base} + \left(dC/dp\right)_{adjacent} + \left(dC/dp\right)_{diagonal} + \left(dC/dp\right)^{T}_{adjacent}. \qquad (3)$$

Because some of the constants (Eddington tensor and boundary current) are spatially and directionally dependant, a transpose-type operation on the adjacent perturbation is required to simulate a neighbor below, as opposed to on the right of, the given assembly.

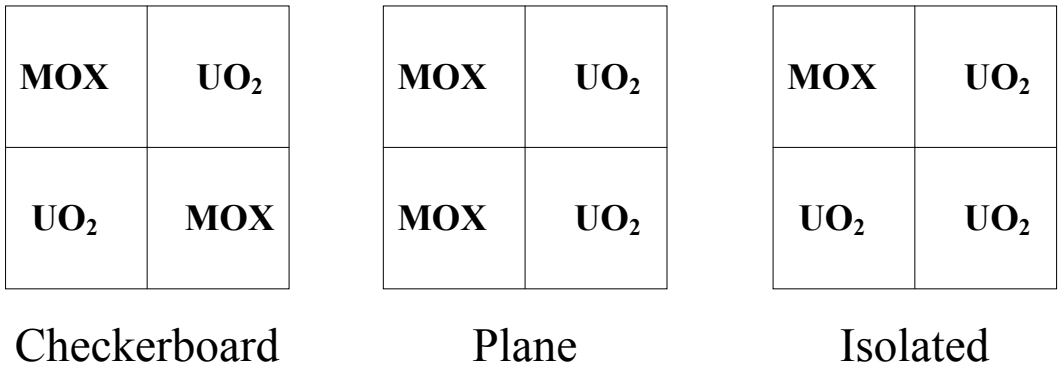

Figure 3.2 The three 2D test configurations for a MOX assembly.

3.3.1.2 Results of the superposition tests

We have tested the accuracy of superposition for each of the three test configurations shown in Figure 3.2, which are tests for computing parameters in the MOX assembly. We have repeated this test for three similar configurations for computing UO_2 parameters. These configurations simply replace each MOX assembly with a UO_2 assembly and vice versa. Thus, we have tested superposition for six different configurations.

For each of the six test configurations, the few-group assembly-averaged cross-sections and Eddington tensors were calculated directly from a four-assembly TALC run to determine the reference value for each of the constants. A "base" case was calculated using a single assembly with reflecting boundaries. Then a fourth four-assembly calculation (basic configuration, shown in Figure 3.1) was performed to determine the effects on the assembly from an unlike adjacent and unlike diagonal neighbor. Sets of dC/dp's were calculated for these configurations. The base-case parameters and the dC/dp's were then combined as in Eq. 3 to estimate the few-group parameters in the given assembly, and these estimated parameters were compared against the reference values.

The relative cross section errors were similar across all three test configurations for each assembly type. Thus, the results presented for the plane configuration, in Table 3.1, are representative of all three. All of the relative errors of the cross sections are reduced by a factor of 10 or more as compared to the reflecting-boundary case, and the maximum error (which always occurred in the downscattering cross section) in both the UO_2 and the MOX is reduced by a factor of 50. Therefore, the spatial superposition of the effects of a neighbor on cross sections appear to provide an excellent approximation to the exact value, especially when compared against the reflecting-boundary cross sections used in today's methodology. This is very encouraging.

The relative errors of the assembly-averaged transport constants (components of the Eddington tensor) are shown in Table 3.2. The diagonal (E_{xx} and E_{yy}) constants are near 1/3, as expected, and are well approximated by the superposition (maximum error is 0.5%). Superposition errors are an order of magnitude lower than the reflecting-boundary (base) errors. The off-diagonal E_{xy} value is exactly zero in the base UO_2 (because of no enrichment grading

and reflecting boundaries) and very small in the "base" MOX assembly. Therefore, there is no off-diagonal transport data conveyed when simply using the "base" case and the relative error is always ~100%. The superposition does not do a good job of approximating the E_{xy}'s, especially when an unlike "diagonal" assembly is involved. There is a strong effect on E_{xy} with a single unlike assembly diagonal to the given assembly, but this effect is significantly reduced when another unlike assembly is introduced adjacent to the current assembly, as in the plane or isolated configuration. However, in these test problems E_{xy} is very small relative to E_{xx} or E_{yy}, and it is not clear that a large relative error in this component will seriously harm the accuracy of the full-core calculation. This is an issue that we are now investigating.

Table 3.1 Relative errors in the MOX and UO_2 cross sections in plane configurations.

		Relative Error	
	Reference Value	Superposition	Reflecting
MOX Assembly			
2 Group K-inf	1.164	0.00%	-0.12%
Fast Group			
Total	0.506	0.00%	0.24%
Absorption	0.017	0.02%	1.04%
Nu*Fission	0.014	0.00%	0.35%
Fission	0.005	0.00%	0.36%
Inscatter	0.479	0.00%	0.16%
Downscatter	0.011	0.05%	2.19%
Thermal Group			
Total	1.606	0.03%	0.39%
Absorption	0.361	-0.02%	-0.24%
Nu*Fission	0.593	-0.02%	-0.23%
Fission	0.207	-0.02%	-0.21%
Inscatter	1.242	0.04%	0.60%
UO2 Assembly			
2 Group K-inf	1.270	0.02%	-0.26%
Fast Group			
Total	0.508	-0.01%	-0.20%
Absorption	0.010	-0.01%	-0.49%
Nu*Fission	0.008	0.05%	-0.57%
Fission	0.003	0.04%	-0.60%
Inscatter	0.483	-0.01%	-0.13%
Downscatter	0.015	0.03%	-2.09%
Thermal Group			
Total	1.292	0.00%	-0.26%
Absorption	0.106	-0.01%	-0.54%
Nu*Fission	0.169	-0.02%	-0.54%
Fission	0.070	-0.02%	-0.54%
Inscatter	1.184	0.00%	-0.24%

Table 3.2 Relative errors in the MOX and UO_2 Eddington components.

	Reference Value			Spatial Superposition			Reflecting		
	Checker	Plane	Isolated	Checker	Plane	Isolated	Checker	Plane	Isolated
MOX Assembly									
Fast									
E_xx	0.335	0.337	0.336	0.03%	-0.03%	-0.02%	-0.85%	-0.23%	-0.68%
E_xy	2.E-04	-2.E-05	2.E-04	6%	-418%	99%	90%	230%	87%
E_yy	0.335	0.337	0.336	0.03%	-0.01%	-0.02%	-0.85%	-0.25%	-0.68%
Thermal									
E_xx	0.334	0.335	0.336	-0.51%	0.27%	-0.23%	4.85%	5.10%	5.30%
E_xy	2.E-03	-4.E-05	4.E-04	-17%	610%	-180%	104%	-56%	114%
E_yy	0.334	0.321	0.336	-0.51%	0.04%	-0.23%	4.85%	1.00%	5.30%
UO2 Assembly									
Fast									
E_xx	0.341	0.339	0.340	0.01%	-0.02%	-0.02%	0.81%	0.19%	0.62%
E_xy	-4.E-05	6.E-05	1.E-04	-129%	146%	151%	100%	100%	100%
E_yy	0.341	0.339	0.340	0.01%	-0.01%	-0.02%	0.81%	0.24%	0.62%
Thermal									
E_xx	0.361	0.361	0.361	-0.10%	0.06%	-0.05%	-1.25%	-1.27%	-1.28%
E_xy	-9.E-04	-4.E-05	-7.E-04	17%	248%	53%	100%	100%	100%
E_yy	0.361	0.365	0.361	-0.10%	-0.02%	-0.05%	-1.25%	0.01%	-1.28%

3.3.2 Albedo Boundary Conditions to Simulate the Effects of a Single Perturbed Neighbor

Because of the CPU and user-interface requirements, most reactor analysis code systems today attempt to retain a single-assembly calculation and somehow account for the effects of different neighbors. We propose to work within this framework and to approximate the effects of a neighbor using a "specialized" albedo boundary condition.

3.3.2.1 One-dimensional albedo approximation

Consider Figure 3.3's two-dimensional approximation of a real assembly (denoted "L" below) with an unlike neighbor (denoted "R") on one side. If we knew exactly what materials were in region "R", we could solve a two-assembly transport problem to obtain the angular flux, ψ_g, at the interface. At that point we could define:

$$g_g\left(\underline{r}_s,\underline{\Omega}\right) = \psi_g\left(\underline{r}_s,\underline{\Omega}\right) / \psi_g\left(\underline{r}_s,\underline{\Omega}'\right). \tag{4}$$

(If R were a mirror image of L, then γ would equal 1 for each group and angle.) If this energy- and angle-dependent albedo were used as a boundary condition for assembly L, then a single-assembly solution in L would be identical to the two-assembly solution. We wish to avoid solving multi-assembly problems; thus, this definition at first appears to be of little value.

The effect of a "different" neighbor is fairly localized to a good approximation (because thermal neutron mean-free paths are very small compared to the assembly width); thus, much of

the interface physics is effectively one-dimensional in space. Further, because γ is a ratio of angular fluxes, it should be relatively insensitive to symmetric changes in geometric details. We therefore propose to estimate the albedo by solving a 1D problem with two homogeneous regions, as depicted in Figure 3.4. Each region has the width of a half-assembly, and we employ reflecting boundaries on the outer edges.

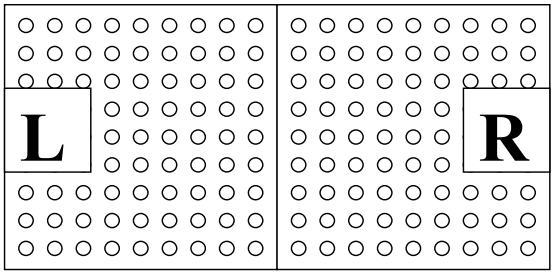

Figure 3.3 Interface between unlike assemblies

This problem is simple enough that an accurate numerical solution will incur relatively low computational cost. We are using a linear-discontinuous finite-element (LD FE) method in space, multi-group in energy, and discrete-ordinates in angle, with logarithmically spaced spatial zoning at the interface, to quickly calculate the solution, which we then use to estimate the albedo:

$$g_g\left(\underline{r}_s,\underline{\Omega}\right)= g_g\left(\underline{r}_s,\mu,\varphi\right)\approx \psi_g^{1DH}\left(\underline{r}_s,\mu\right)/\psi_g^{1DH}\left(\underline{r}_s,-\mu\right),\quad \mu=\text{cosine}\left(\underline{\Omega}\cdot\underline{n}\right)<0\,. \qquad (5)$$

This approximation provides a significant improvement over the reflecting boundary "base" case, but it still yields appreciable errors near the "corner" interface among four assemblies, as one might expect [7]. Therefore, a two-dimensional modification to the 1D albedo is required to achieve the accuracy we seek.

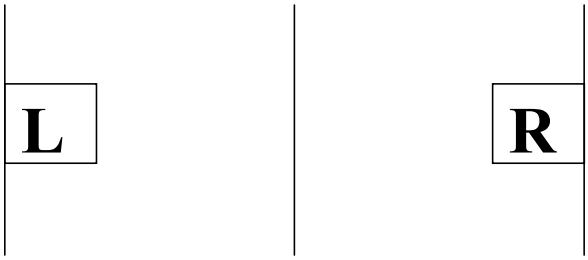

Figure 3.4 Approximate 1D model of interface between assemblies

3.3.2.2 Two-dimensional albedo modification

Because the 1D homogeneous albedo produces a very good approximation to the boundary condition away from corner points, a simple modification should be able to account for the 2D effects, which are strongest at corners. Our procedure for obtaining an improved albedo begins by arranging the given assembly (denoted MOX) and the neighbor (denoted UO_2) as shown in Figure 3.2. Each quarter-assembly is spatially homogenized into pin cells and a simple multi-group, finite-volume diffusion calculation is used to estimate the multi-group, pin-averaged flux shape. This calculation is inexpensive compared to a single-assembly fine-mesh fine-group transport calculation.

The pin cells are then represented as multi-group flat-source regions, with the scattering and fissions sources derived from the finite-volume diffusion solution. Using one simplified long-characteristics sweep, for each azimuthal and polar angle from the assembly-level code's quadrature set, the angular flux at the center of each pin-cell edge on both the L/L and the L/R interfaces are calculated. These angular fluxes are used to calculate a multi-group, pin-cell-edge two-dimensional albedo $g_g^{2D}(R_s, \underline{\Omega})$ for each direction used in the assembly-level code.

This 2D albedo is then used to modify the existing 1D homogenous albedo. The albedo of the pin cell nearest the center of the interface between adjacent assemblies is assumed to be exactly the 1D homogenous albedo. The ratio of the 2D albedo on a given pin-cell edge to the 2D albedo at the center-pin edge is then used to modify the 1D albedo:

$$g_g(R_s, \underline{\Omega}) = g_g^{1DH}(\underline{\Omega}) * \left[\frac{g_g^{2D}(R_s, \underline{\Omega})}{g_g^{2D}(R_c, \underline{\Omega})} \right], \tag{6}$$

where R_s is any pin-cell edge along the interface and R_c is the centerline pin cell.

We construct the albedo as in Eq. (6) along both the L/R and L/L interface in the configuration of Figure 3.2. Different combinations of these albedos and reflecting boundary conditions allow us to model a single adjacent R neighbor or a single diagonal R neighbor; all other R-neighbor configurations can then be built from superposition.

3.3.2.3 Results of the two-dimensional albedo approximation

For both assemblies in a "basic" colorset configuration, the few-group, assembly-averaged cross-sections and Eddington tensors were calculated to determine the reference value of the "diagonal" and "adjacent" assemblies. A "base" case was calculated using a single assembly with reflecting boundaries. The resulting multi-group assembly-averaged cross sections were used in both the LD FE code, to determine the 1D homogenous albedo, and the diffusion code, to determine an approximate albedo boundary condition for the "diagonal" and "adjacent" configurations. Two single-assembly calculations, using the two-dimensional boundary conditions, were calculated to determine the approximate few-group, assembly-averaged cross-sections and Eddington tensors. Also, a single-assembly calculation using the 1D homogeneous boundary condition was used to provide a "1D" approximation of the constants due to an

adjacent unlike assembly. The 1D and 2D constants were compared, along with the "base" (reflecting-boundary) constants, to the reference values.

The relative cross section errors, shown in Table 3.3, are very small in both "adjacent" and "diagonal" configurations, but the 2D albedo does improve accuracy. In the "adjacent" case, the sign of the error, for nearly all cross sections, changes from the "base" to the "1D approximation", which leads to the expectation that an improved 1D albedo might significantly improve the results. The 2D modification reduces the error of the 1D approximation; the maximum error is less than 1% using the 2D albedo. The most significant improvement occurs in the thermal group in the UO_2 assembly, where the relative error drops to less than 0.02%. In the "diagonal" case, the 2D approximation reduces the error for nearly all cross sections, but with very little change, especially in the fast group, to already small errors.

Table 3.3 2D approximation of MOX and UO_2 assemblies in diagonal and adjacent configurations.

	Adjacent				Diagonal		
		2D	1D	Reflect		2D	Reflect
	Reference	*Relative Error*			Reference	*Relative Error*	
MOX Assembly							
2 Group K-inf	**1.164**	0.06%	0.07%	-0.07%	**1.164**	-0.03%	-0.04%
Fast Group							
Total	**0.506**	-0.14%	-0.17%	0.12%	**0.506**	0.09%	0.12%
Absorption	**0.017**	-0.42%	-0.55%	0.77%	**0.016**	0.15%	0.26%
Nu*Fission	**0.014**	-0.11%	-0.14%	0.26%	**0.014**	0.07%	0.09%
Fission	**0.005**	-0.12%	-0.15%	0.26%	**0.005**	0.07%	0.10%
Inscatter	**0.479**	-0.12%	-0.13%	0.06%	**0.479**	0.09%	0.11%
Downscatter	**0.011**	-0.89%	-1.25%	1.69%	**0.010**	0.19%	0.47%
Thermal Group							
Total	**1.606**	-0.10%	-0.19%	0.37%	**1.600**	-0.05%	0.00%
Absorption	**0.362**	0.10%	0.29%	-0.12%	**0.362**	0.06%	-0.10%
Nu*Fission	**0.593**	0.09%	0.30%	-0.11%	**0.594**	0.06%	-0.11%
Fission	**0.208**	0.09%	0.29%	-0.09%	**0.207**	0.06%	-0.10%
Inscatter	**1.241**	-0.16%	-0.34%	0.53%	**1.235**	-0.08%	0.03%
UO2 Assembly							
2 Group K-inf	**1.270**	0.03%	0.07%	-0.25%	**1.273**	0.03%	-0.03%
Fast Group							
Total	**0.509**	0.11%	0.14%	-0.10%	**0.509**	-0.08%	-0.09%
Absorption	**0.010**	0.21%	0.26%	-0.30%	**0.010**	-0.14%	-0.18%
Nu*Fission	**0.008**	0.10%	0.16%	-0.47%	**0.008**	-0.04%	-0.15%
Fission	**0.003**	0.13%	0.19%	-0.48%	**0.003**	-0.05%	-0.16%
Inscatter	**0.483**	0.10%	0.12%	-0.04%	**0.483**	-0.08%	-0.08%
Downscatter	**0.015**	0.58%	0.85%	-1.67%	**0.015**	-0.14%	-0.44%
Thermal Group							
Total	**1.292**	-0.02%	0.04%	-0.23%	**1.295**	0.03%	-0.02%
Absorption	**0.106**	-0.04%	0.07%	-0.49%	**0.106**	0.06%	-0.04%
Nu*Fission	**0.170**	-0.04%	0.07%	-0.49%	**0.170**	0.06%	-0.03%
Fission	**0.070**	-0.04%	0.07%	-0.49%	**0.070**	0.06%	-0.03%
Inscatter	**1.184**	-0.02%	0.04%	-0.22%	**1.186**	0.03%	-0.02%

The relative errors in the assembly-averaged Eddington tensors are shown in Table 3.4. The relative errors in the diagonal (E_{xx} and E_{yy}) components are, in each approximation, not large (under 5%). The 2D albedo reduces the maximum error (thermal-group MOX E_{xx}) by a factor of five to less than 1%. E_{xx} is the transport constant in the direction of the unlike neighbor. The 1D albedo improves the E_{xx} in both assemblies and groups, with a more significant change in the thermal groups. The 2D albedo further reduces the error in the thermal constants, but has the opposite effect in the fast group. A similar trend is seen in the diagonal assembly: a poor modification in the fast groups and an over-modified albedo in the thermal groups (as evidenced by a change in sign of the error).

E_{xy} is approximately zero in the base case; therefore, its error is nearly 100%. Similarly, the 1D approximation of the UO_2 assembly has no effect on E_{xy}, because it is simply a 1D modification to a uniformly enriched assembly. The MOX error is actually increased. The 2D approximation shows improvement in the thermal groups, but decreases the accuracy in the fast groups; the fast UO_2 E_{xy} even has the incorrect sign. We are currently investigating the cause of this poor E_{xy} behavior as well as the significance of such errors when E_{xy} is this small.

The 1D albedo improves accuracy compared to the reflecting-boundary approximation, but is not sufficient to account for the two-dimensional transport effects of the off-diagonal (E_{xy}) component of the Eddington tensor. In addition, the 1D albedo overestimates the effects of the neighbor because it uses an assembly-averaged cross section for an assembly with graded enrichment, which leads to a change in sign of the error. Our 2D modification to the albedo reduces this error in several instances, especially in the thermal group, but in its current form it does not correctly model the off-diagonal Eddington tensor either. We are investigating simple strategies for further improvements.

Table 3.4 2D approximation of the Eddington tensor in the adjacent and diagonal configurations.

	Adjacent				Diagonal		
		2D	1D	Reflect		2D	Reflect
	Exact	*Relative Error*			Exact	*Relative Error*	
MOX Assembly							
Fast Group							
E_xx	**0.337**	-0.34%	-0.20%	-0.42%	**0.339**	0.24%	0.22%
E_xy	**1.E-04**	257%	153%	80%	**-2.E-04**	135%	112%
E_yy	**0.337**	-0.19%	-0.15%	-0.46%	**0.339**	0.24%	0.22%
Thermal Group							
E_xx	**0.334**	-0.88%	-1.82%	4.65%	**0.319**	-0.27%	0.22%
E_xy	**1.E-03**	-75%	146%	106%	**-8.E-04**	-103%	92%
E_yy	**0.321**	-0.33%	-0.87%	0.75%	**0.319**	-0.27%	0.22%
UO2 Assembly							
Fast Group							
E_xx	**0.339**	0.19%	0.20%	0.38%	**0.337**	-0.28%	-0.17%
E_xy	**-4.E-05**	565%	100%	100%	**2.E-05**	2665%	100%
E_yy	**0.339**	0.23%	0.13%	0.42%	**0.337**	-0.28%	-0.17%
Thermal Group							
E_xx	**0.361**	-0.01%	0.04%	-1.25%	**0.365**	0.05%	-0.08%
E_xy	**-4.E-04**	-67%	100%	100%	**4.E-04**	-68%	100%
E_yy	**0.366**	-0.03%	0.13%	0.10%	**0.365**	0.05%	-0.08%

In summary, the 2D albedo that we have devised is a computationally efficient way to capture most of the effects that unlike neighbors have on a given assembly. Albedo-based single-assembly calculations produce significantly more accurate few-group cross sections and somewhat more accurate Eddington tensors. We have hypotheses about the causes of the largest remaining errors and ideas for simple ways to improve our albedos and reduce those errors. We will study these in the near future.

3.3.3 2D Albedo Boundary Condition Coupled with Spatial Superposition

To fully utilize the single-assembly calculation with albedo boundary conditions and minimize the number of required branches, we must combine spatial superposition with the 2D albedo approximation. In this subsection we test this combination for each of our six test configurations (three for a MOX assembly and three for UO_2). For each configuration we generate a reference solution with a four-assembly TALC calculation. All other solutions in this subsection use TALC only for single-assembly calculations, some with albedo boundary conditions as described above.

A summary of the cross section results is shown in Table 3.5. The highest cross section error is consistently found in the downscatter cross section, so we display this error. In general, there is a reduction in the error as the boundary condition improves from reflecting to 1D albedo to 2D albedo, but the error in the 2D approximation is much greater than the error from the

Table 3.5 Cross-section errors from all tested approximations.

	MOX		UO2	
	Downscatter	2-Group K-inf	Downscatter	2-Group K-inf
Reference values				
Checkerboard	0.0107	1.1632	0.0147	1.2671
Plane	0.0106	1.1635	0.0149	1.2702
Isolated	0.0108	1.1627	0.0146	1.2670
Spatial Superposition				
Checkerboard	-0.05%	0.00%	-0.06%	0.00%
Plane	0.05%	0.00%	0.03%	0.02%
Isolated	0.04%	0.00%	0.01%	0.03%
2D Albedo with Spatial Superposition				
Checkerboard	-1.81%	0.12%	1.12%	0.07%
Plane	-0.66%	0.03%	0.47%	0.07%
Isolated	-1.53%	0.08%	1.06%	0.12%
1D Albedo with Spatial Superposition				
Checkerboard	-2.50%	0.14%	1.68%	0.14%
Plane	-0.74%	0.03%	0.44%	0.06%
Isolated	-1.95%	0.10%	1.30%	0.14%
Reflecting Boundaries				
Checkerboard	3.28%	-0.15%	-3.45%	-0.51%
Plane	2.19%	-0.12%	-2.09%	-0.26%
Isolated	3.80%	-0.19%	-3.85%	-0.51%

superposition of the colorsets (reported in earlier tables). We must investigate further to determine whether further improvements are needed in our albedo boundary conditions; it is possible that they are accurate enough that a different part of our overall methodology is now the limiting factor. As mentioned above, we believe we can devise simple modifications to improve our albedos if this is needed.

The Eddington-tensor results are displayed in Tables 3.6 and 3.7 for UO_2 and MOX, respectively. The E_{xx} and E_{yy} components are very accurate and improve with each improvement in the boundary condition. E_{xx} suffers from inaccuracy as described previously; further investigation will determine whether this is significant. [Note that today's reactor analyses use diffusion theory, which corresponds to E_{xy} =0 and $E_{xx} = E_{yy} = 1/3$.]

Table 3.6 Eddington-tensor errors from all approximations: UO_2 assembly.

	Fast Group			Thermal Group		
	E_xx	E_xy	E_yy	E_xx	E_xy	E_yy
Reference values						
Checkerboard	0.3407	-4.E-05	0.3407	0.3606	-9.E-04	0.3606
Plane	0.3386	6.E-05	0.3387	0.3606	-4.E-05	0.3652
Isolated	0.3400	1.E-04	0.3400	0.3605	-7.E-04	0.3605
Spatial Superposition						
Checkerboard	0.01%	-129%	0.01%	-0.10%	17%	-0.10%
Plane	-0.02%	146%	-0.01%	0.06%	247%	-0.01%
Isolated	-0.02%	151%	-0.02%	-0.04%	53%	-0.04%
2D Albedo with Spatial Superposition						
Checkerboard	0.43%	1163%	0.43%	-0.14%	-38%	-0.14%
Plane	-0.11%	458%	-0.06%	0.10%	365%	0.00%
Isolated	0.13%	106%	0.13%	-0.04%	23%	-0.04%
1D Albedo with Spatial Superposition						
Checkerboard	0.35%	100%	0.35%	0.07%	100%	0.07%
Plane	0.01%	100%	-0.05%	0.02%	100%	0.03%
Isolated	0.15%	100%	0.15%	0.05%	100%	0.05%
Reflecting Boundaries						
Checkerboard	0.81%	100%	0.81%	-1.25%	100%	-1.25%
Plane	0.19%	100%	0.24%	-1.27%	100%	0.01%
Isolated	0.62%	100%	0.62%	-1.28%	100%	-1.28%

Table 3.7 Eddington tensor from the superposition of all approximations in the MOX

	Fast Group			Thermal Group		
	E_xx	E_xy	E_yy	E_xx	E_xy	E_yy
Reference values						
Checkerboard	0.3354	2.E-04	0.3354	0.3344	2.E-03	0.3344
Plane	0.3375	-2.E-05	0.3374	0.3353	-4.E-05	0.3214
Isolated	0.3360	2.E-04	0.3360	0.3360	4.E-04	0.3360
Spatial Superposition						
Checkerboard	0.03%	6%	0.03%	-0.51%	-17%	-0.51%
Plane	-0.03%	-418%	-0.01%	0.27%	610%	0.04%
Isolated	-0.02%	99%	-0.02%	-0.23%	-180%	-0.23%
2D Albedo with Spatial Superposition						
Checkerboard	-0.51%	274%	-0.51%	-1.71%	-102%	-1.71%
Plane	-0.13%	-687%	0.04%	-0.87%	281%	-0.57%
Isolated	-0.31%	299%	-0.31%	-1.68%	-314%	-1.68%
1D Albedo with Spatial Superposition						
Checkerboard	-0.32%	166%	-0.32%	-3.15%	149%	-3.15%
Plane	-0.01%	-248%	0.05%	-1.33%	-1019%	-0.61%
Isolated	-0.15%	185%	-0.15%	-2.66%	289%	-2.66%
Reflecting Boundaries						
Checkerboard	-0.85%	90%	-0.85%	4.85%	104%	4.85%
Plane	-0.23%	230%	-0.25%	5.10%	-56%	1.00%
Isolated	-0.68%	87%	-0.68%	5.30%	114%	5.30%

3.4 Conclusions

We have developed extensions of present-day reactor-analysis methodology that systematically account for the effects that different neighbors have on a given assembly's few-group constants. One extension is branch cases that generate the effect of unlike neighbors on a given assembly's group constants. Another extension is to use superposition of the effects of neighboring assemblies to reduce the number of branch calculations that are needed to tabulate the effects of all possible neighbor permutations. Finally, we also use energy-, angle-, and position-dependent albedos to simulate the presence of the unlike neighbors in our branch calculations. We have developed and tested a procedure for efficiently estimating these albedos.

We envision two neighbor-assembly branches for each type of neighboring assembly, one for an adjacent configuration and one for diagonal. For each type and configuration we further envision a small number of branches on the neighbor's burnup and one branch with the neighbor containing a control rod. Other branches might be necessary in some applications. For each branch case we estimate an albedo and perform a single-assembly calculation; this fits into the framework of present-day methodology. (The base case corresponds to all identical neighbors – which produces the usual reflecting boundary condition.) The keys to computational efficiency are rapid estimation of albedos, the use of superposition, and keeping the number of branch cases reasonably low. The keys to accuracy are accurate estimation of albedos and careful attention to the limits of the superposition approximation.

We have found that spatial superposition of the effects of adjacent and diagonal neighbors provides an excellent approximation to the effects of multiple neighbors on the assembly cross sections and the diagonal (*xx* and *yy*) Eddington-tensor components. There is a large relative error in the superposition approximation of the very small off-diagonal (*xy*) component, the significance of which has not yet been determined.

We have found that the albedos produced from 1D homogenized calculations do a reasonably good job of capturing the effects of a different neighbor except near assembly corners, although it appears likely that explicit representation of the water gap will add enough accuracy to warrant its complexity. We have devised a 2D homogenized diffusion approximation combined with a fixed-source long-characteristics transport sweep to obtain 2D correction factors for the 1D albedo. This does not cause the off-diagonal tensor component to be accurate, but it does improve the cross sections and diagonal tensor components. Our estimated albedos produce significant improvements over the reflecting condition, but we believe that further significant improvement is possible, and we are actively pursuing such improvement.

We are currently working to couple our assembly-level results with full-core quasi-diffusion calculations to assess the impact of the errors that remain in our cross sections and Eddington tensors. If this assessment shows that further assembly-level improvements will noticeably improve the accuracy of the overall methodology, then we believe we can accomplish these improvements, beginning with simple improvements to our albedo boundary conditions.

In summary, we believe the new methodology described here is promising, and we expect to continue to refine it, couple it to other pieces of a full reactor-analysis system, and test the coupled system. We hope to report on further progress in future communications.

Bibliography

[1] D. Knott et al., "CASMO-4 Methodology Manual," STUDSVIK/SOA-95/02, Studsvik of America (1995).

[2] K. Smith, "MOX Analysis Methods in SIMULATE-3," *Trans. Am. Nucl. Soc.*, **76**, pp.181 (1997).

[3] K. Rempe, K. Smith, "Mixed-Oxide and BWR Pin Power Reconstruction in SIMULATE-3," *PHYSOR 90*, Marseille, France, April 1990, Vol. 2, p. VIII-11.

[4] S. Palmtag, A. Henry, "Advanced Nodal Methods for MOX Fuel Analysis," Massachusetts Institute of Technology, Nuclear Engineering Department, Ph.D. Thesis, September 1997.

[5] M. R. Zika, "Iterative Acceleration for Two-Dimensional Long Characteristics Transport Problems," Texas A&M University, Department of Nuclear Engineering, PhD dissertation (M. L. Adams, advisor) (1997).

[6] M. R. Zika and M. L. Adams, "Transport Synthetic Acceleration for Long-Characteristics Assembly-Level Transport Problems," *Nucl. Sci. Eng.*, **134**, pp.135-158 (2000).

[7] K. T. Clarno and M. L. Adams, "Improved Boundary Conditions for Assembly-Level Transport Codes," *Int. Conf. on the New Frontiers of Nuclear Technology: Reactor Physics, Safety and High-Performance Computing* (PHYSOR 2002), Seoul, Korea, October 2002, pp. 11A-01.

Chapter 4

Recent Improvements in Boundary Conditions for Single-Assembly Calculations

4.1 Introduction

A major challenge in reactor analysis is obtaining the local power shape and homogenized few-group constants for an assembly whose neighbors are significantly different. If the neighbors are similar to the assembly in question, then the solution in the assembly is well-approximated by solving a single-assembly problem with reflecting boundaries. However, if an assembly's neighbor is significantly different, the reflecting boundary condition produces inaccuracies.

In recent papers [1][2] we reported some attempts to reduce this inaccuracy. Our strategy is to add branch cases that account for unlike neighbors, much like branch cases now account for other deviations from "base-case" conditions. Each neighbor-branch considers a known assembly touching the given assembly along a surface or at a corner. The desired solution could be obtained by solving a four-assembly "colorset" with three given assemblies and one different neighbor. We wish to avoid the expense of this four-assembly fine-mesh transport solution by using a one-assembly calculation with albedo boundary conditions that simulate the neighbor.

Here we describe an improved procedure for generating albedos for the single-assembly calculation and compare the results against reference solutions and against previous results from [2]. Our test problems show that the new albedos yield substantial improvements in few-group constants.

This work is part of a larger collaborative project that uses *quasi-diffusion* equations for core-level analysis [3][4][5]. To support this project our single-assembly calculation must produce components of the "Eddington tensor," defined as follows, where $u=x$ or y, $v = x$ or y.

$$E_{uv}(\vec{r}) = \frac{\int_{4p} \Omega_u \Omega_v \psi(\vec{r},\vec{\Omega})\, d\Omega}{\int_{4p} \psi(\vec{r},\vec{\Omega})\, d\Omega}.$$

4.2 Estimation of Albedo

Our albedo boundary condition is implemented in a long-characteristics transport code as follows:

$$y_g\left(\vec{r},\vec{\Omega}\right) = g_{g,e}\left(\vec{\Omega}\right) y\left(\vec{r},\vec{\Omega}'\right), \vec{r} \in \text{edge } e. \tag{2}$$

Here g is the energy-group index and $\vec{\Omega}'$ is the direction that reflects onto $\vec{\Omega}$ on edge e. (The reflecting condition is $g_{g,e}\left(\vec{\Omega}\right) = 1$ for all g, e, and $\vec{\Omega}$.) The question addressed here is how to inexpensively but accurately estimate $g_{g,e}\left(\vec{\Omega}\right)$.

As in previous work [2], we assume that reflecting-boundary calculations have been performed for all assemblies before any neighbor branches are calculated. Thus, when a neighbor branch is calculated, homogenized cross sections are available for the neighbor assembly.

Let "A" denote the given assembly with neighbor "N." We arrange one "N" and three "A" assemblies (or quarter-assemblies if symmetry permits) into a 2x2 array. We assume that each quarter-assembly has four homogeneous regions: the corner pincell, two edge rows of pincells, and the interior. Figure 4.1 shows a sketch of this simplified colorset.

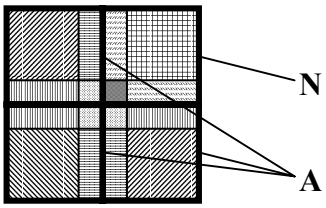

Fig. 4.1 Sketch of simplified four-assembly colorset showing homogeneous regions.

We solve the k-eigenvalue problem for this simplified colorset using cell-centered finite-volume diffusion with one mesh cell per pin cell, using reflecting (zero-current) boundary conditions on the outer surfaces. This calculation, which uses the same energy groups as the single-assembly transport, produces an estimate of the scattering + fission source in each pin cell. We then perform an inexpensive long-characteristic transport calculation to obtain angular fluxes at the midpoints of pin-cell edges that will need albedos (i.e., on two surfaces of one "A" assembly). The calculation for direction $\vec{\Omega}$ marches backward from each edge midpoint in direction $-\vec{\Omega}$, accumulating contributions until it has traversed at least 10 mean-free paths, at which point further contributions are neglected. Ratios of edge-center angular fluxes produce the albedos, $g_{g,e}\left(\vec{\Omega}\right)$.

One difference from previous work [2] is the use of nine separate homogenized regions in each assembly in the simplified colorset calculation. Previously each assembly was fully homogenized. This difference is important for non-uniform assemblies. Previously we forced the albedo at the center of the surface between two assemblies to equal an albedo calculated from

a simple 1D transport calculation, reasoning that far from corners the effects should be largely one-dimensional and that the transport calculation should add accuracy. We have now found that in the high-energy groups, even far from corners, the effects are not one-dimensional. Our new method, therefore, does not employ a 1D transport calculation in its estimation of albedos.

4.3 Results

We consider two assembly types: MOX with three enrichment zones and U with uniform enrichment. Problem A generates MOX constants given a U assembly diagonally opposed (touching a corner); B generates MOX constants given an adjacent U assembly (sharing a surface); C generates U constants given an adjacent MOX assembly. In Table 4.1I we compare few-group constants generated by our previous and new methods against reference results, which are generated by applying our fine-mesh long-characteristic code [6] to each full colorset. We also compare results from reflecting-boundary calculations (albedo=1). The "old" albedo of [2] improves the 2-group homogenized cross sections compared to the standard reflecting-boundary method. The new albedo produces further improvements. The largest cross-section error in the table is 1.69% for reflecting, 0.63% for the old albedo, and 0.26% for the new albedo. All methods produce accurate E_{xx} and E_{yy} values. Only the new albedo produces accurate thermal-group E_{xy} values. No method shown here produces accurate fast-group E_{xy} values. We expect to address this issue in a future communication.

All methods produce accurate E_{xx} and E_{yy} values. Only the new albedo produces accurate thermal-group E_{xy} values. No method shown here produces accurate fast-group E_{xy} values. We expect to address this issue in a future communication.

TABLE I. Errors in results from various methods. (1 = fast; 2 = thermal)

Con-stant	Test Problem											
	A				B				C			
	Ref. Val.	% Relative Error or *value*			Ref. Val.	% Relative Error or *value*			Ref.Val	% Relative Error or *value*		
		Albedo =1	Old Alb.	New Alb.		Albedo =1	Old Alb.	New Alb.		Albedo =1	Old Alb.	New Alb.
2-grp k_∞	1.164	–0.04	–0.04	–0.03	1.164	–0.07	0.09	0.05	1.270	–0.25	0.01	–0.01
$\Sigma_{t,1}$	0.506	0.12	0.10	0.09	0.506	0.11	–0.13	–0.07	0.509	–0.10	0.11	0.09
$\Sigma_{a,1}$	0.016	0.26	0.19	0.17	0.017	0.76	–0.38	–0.10	0.010	–0.30	0.20	0.16
$\nu\Sigma_{f,1}$	0.014	0.09	0.08	0.07	0.014	0.25	–0.10	0.01	0.008	–0.43	0.10	0.06
$\Sigma_{1\to2}$	0.010	0.47	0.29	0.25	0.011	1.69	–0.63	–0.09	0.015	–1.69	0.42	0.26
$\Sigma_{t,2}$	1.600	0.00	-0.03	-0.03	1.607	0.41	0.04	–0.09	1.291	–0.27	–0.04	–0.05
$\Sigma_{a,2}$	0.362	–0.10	0.03	0.02	0.362	–0.12	–0.05	0.12	0.106	–0.58	–0.04	–0.07
$\nu\Sigma_{f,2}$	0.594	–0.11	0.03	0.01	0.594	–0.10	–0.05	0.13	0.170	–0.58	–0.03	–0.06
$E_{xx,1}$	0.333	0.03	0.02	0.02	0.333	–0.03	–0.03	0.29	0.333	0.03	–0.02	–0.01
$E_{yy,1}$	0.333	0.03	0.02	0.02	0.333	–0.03	–0.02	–0.11	0.333	0.02	0.05	0.05
$E_{xy,1}$	–7E-5	*1E-5*	*2E-5*	*3E-5*	4.E-5	*1E-5*	*–1E-4*	*–9E-5*	–7E-6	*–1E-9*	*8E-5*	*1E-4*
$E_{xx,2}$	0.332	0.03	0.02	0.02	0.336	1.34	–0.19	0.56	0.333	–0.48	–0.01	–0.01
$E_{yy,2}$	0.332	0.03	0.02	0.02	0.330	–0.66	0.08	–0.19	0.336	0.00	–0.03	–0.03
$E_{xy,2}$	–4E-4	*–3E-5*	*–4E-4*	*–4E-4*	5.E-4	*–3E-5*	*4E-4*	*5E-4*	–2E-4	*–2E-9*	*–2E-4*	*–2E-4*

4.4 Summary

Our new method for estimating albedos allows the efficient generation of homogenized cross sections that more accurately include the effects of unlike neighbors. In its current stage of evolution the method does not produce accurate *xy* components of the Eddington tensor in the fast energy group.

Bibliography

[1] K. T. Clarno, M. L. Adams, Int. Conf. on the New Frontiers of Nuclear Technology: Reactor Physics, Safety and High-Performance Computing (PHYSOR 2002), Seoul, Korea, October 2002.

[2] K. T. Clarno, M. L. Adams, Proc. International Conf. on Nuclear Mathematical and Computational Sciences, Gatlinburg, TN, April 6-10 (2003).

[3] D. Y. Anistratov, Int. Conf. on the New Frontiers of Nuclear Technology: Reactor Physics, Safety and High-Performance Computing (PHYSOR 2002), Seoul, Korea, October 2002.

[4] H. Hiruta, D. Y. Anistratov, M. L. Adams, *Proc. International Conf. on Nuclear Mathematical and Computational Sciences*, Gatlinburg, TN, April 6-10 (2003)

[5] R. Nes, T. S. Palmer, Int. Conf. on the New Frontiers of Nuclear Technology: Reactor Physics, Safety and High-Performance Computing (PHYSOR 2002), Seoul, Korea, October 2002.

[6] M. R. Zika, M. L. Adams, *Nucl. Sci. Eng.*, **134**, 135-158 (2000).

Chapter 5

Consistent Spatial Discretization of the Low-Order Quasidiffusion Equations on Coarse Grids

5.1 Abstract

In this chapter we develop a spatial discretization method for the low-order quasidiffusion equations on coarse grids for full-core reactor calculations. The proposed method reproduces accurately the complicated large-scale behavior of the transport solution within assemblies. The resulting discretization is spatially consistent with a fine-mesh discretization of the transport equation in the sense that it preserves zeroth, first and second spatial Legendre moments of the fine-mesh transport solution over coarse-mesh cells along with the surface currents, and eigenvalue. Numerical results that demonstrate accuracy of the proposed methodology are presented.

5.2 Introduction

The present computational methodologies for reactor analysis are based on full-core and assembly-level calculations. Full-core calculations generate eigenvalues and power distributions for a reactor core using few-group diffusion equation approximated on coarse grids. Each grid cell represents a large part of an assembly. The group data (i.e. cross sections, diffusion coefficients, discontinuity factors and other functionals) are obtained from assembly-level transport calculations in which the many-group transport equation is solved in isolated assembly with reflective boundary conditions on fine spatial grids.

An alternative approach was recently developed [1, 2, 3, 4, 5, 6]. To account for the complicated transport effects in full-core calculations, a new methodology is based on low-order quasidiffusion (LOQD) equations [7, 8, 9]. This approach is also combined with single-assembly transport calculations that use special albedo boundary conditions which enable one to simulate efficiently effects of an unlike neighboring assembly on assembly's group data [2, 6].

The LOQD equations can capture transport effects to an arbitrary degree of accuracy. These equations can be reduced to a diffusion-like form. These features make the LOQD

equations very attractive for using them as a background for methodology for reactor core calculations. In full reactor core calculations, it is necessary to use discretization methods that are very accurate on coarse meshes. In this paper we develop methods for approximating of the LOQD equations on coarse grids. It is necessary for such method to preserve the averaged reaction rates, surface-averaged group currents, and eigenvalue [10]. The way to improve accuracy of coarse-mesh calculations is to put more physics into coarse-mesh solution. This can be achieved by developing coarse-mesh discretization methods that reproduce accurately the large-scale behavior of the transport solution within assemblies that is characterized by a set of its pin-cell average values.

In this paper we present a finite-element discretization scheme of the low-order equations of the quasidiffusion (QD) method on coarse grids. On the basis of this scheme, we develop a coarse-mesh discretization of the LOQD equations that preserves exactly several spatial moments of the fine-mesh transport solution over coarse-mesh cells (e.g., assembly or quarter assembly). We analyze the behavior of the proposed method on numerical test problems that simulate the interaction of MOX and uranium assemblies with enrichment variations and water holes, and consider sensitivity of the coarse-mesh solution to perturbations in group data.

The reminder of the paper is organized as follows. In Sec. 5.3 we formulate the few-group LOQD equations. In Sec. 5.4 we derive a basic coarse-mesh finite element method for the LOQD equations that preserves zeroth moment of the fine-mesh transport solution as well as surface currents and eigenvalue. In Sec. 5.5 we present an advanced coarse-mesh finite-element method that preserves extra spatial moments of the fine-mesh transport solution. In Sec. 5.6 we demonstrate numerical solutions of test problems that simulate the interaction of MOX and uranium assemblies. We conclude with a discussion in Sec. 5.7.

5.3 The Few-Group Low-Order Quasidiffusion Equations

5.3.1 The LOQD Equations

We consider a few-group k-eigenvalue transport problem for 1D slab geometry with vacuum boundary conditions, $0 \le x \le X$, $g = 1, ..., M_g$. The LOQD equations [7, 9, 11, 12] for the group scalar flux ϕ^g and current J^g are

$$\frac{d}{dx} J^g + \Sigma_t^g \phi^g = \sum_{p=1}^{M_g} \Sigma_{s,0}^{p \to g} \phi^p + \frac{1}{k_{eff}} \chi^g \sum_{p=1}^{M_g} \nu_f^p \Sigma_f^p \phi^p \ , \tag{5.1}$$

$$\frac{d}{dx} \left(E^g \phi^g \right) + \Sigma_t^g J^g = 0 \ , \tag{5.2}$$

$$J^g(0) = C_L^g \phi^g(0) \ , \quad J^g(X) = C_R^g \phi^g(X) \ . \tag{5.3}$$

The functionals E^g, C_L^g and C_R^g are calculated by means of the few-group transport solution

$$E^g = \int_{-1}^{1} \mu^2 \psi^g d\mu \Big/ \int_{-1}^{1} \psi^g d\mu \ , \tag{5.4}$$

$$C_L^g = \int_{-1}^{0} \mu\psi^g d\mu \Big/ \int_{-1}^{0} \psi^g d\mu \Bigg|_{x=0} \quad , \quad C_R^g = \int_{0}^{1} \mu\psi^g d\mu \Big/ \int_{0}^{1} \psi^g d\mu \Bigg|_{x=X} \tag{5.5}$$

where ψ^g is the group angular flux. The LOQD problem (5.1)-(5.3) exactly reproduces the transport scalar flux and current provided that the functionals are exact.

5.3.2 Generation of Few-Group Data

The LOQD equations are used in combination with assembly-level transport calculations that utilize the albedo boundary conditions without making color-set calculations, to simulate interaction with adjacent assembly in a reactor core.

Let us consider that each coarse-mesh cell represents a whole assembly. To generate fine-mesh transport solution for a given assembly (coarse cell) and calculate the averaged cross sections and functionals for the few-group coarse-mesh discretized LOQD equations, we perform a set of single-assembly fine-group transport calculations on fine spatial mesh with albedo boundary conditions ($0 \le x \le X$)

$$\psi^m(0,\mu) = \gamma_L^m(\mu)\psi^m(0,-\mu)\,, \text{ for } \mu > 0\,, \quad \psi^m(X,\mu) = \gamma_R^m(\mu)\psi^m(X,-\mu)\,, \text{ for } \mu < 0 \tag{5.6}$$

where γ_L^m, γ_R^m are albedos. The resulting boundary conditions for the fine-group LOQD equations have the following form:

$$J^m(0) = \frac{1-\lambda_{L,1}^m}{1+\lambda_{L,0}^m} C_L^m \phi^m(0)\,, \quad \lambda_{L,n}^m = \int_0^1 \mu^n \gamma_L^m(-\mu)\psi^m(0,\mu)d\mu \Big/ \int_0^1 \mu^n \psi^m(0,\mu)d\mu\,, \tag{5.7}$$

$$J^m(X) = \frac{1-\lambda_{R,1}^m}{1+\lambda_{R,0}^m} C_R^L \phi^m(X)\,, \quad \lambda_{R,n}^m = \int_{-1}^0 \mu^n \gamma_R^m(-\mu)\psi^m(X,\mu)d\mu \Big/ \int_{-1}^0 \mu^n \psi^m(X,\mu)d\mu\,, \tag{5.8}$$

where $n = 0, 1$. In this methodology various albedos are used to simulate interface phenomena between different assemblies [1, 2, 6].

5.3.3 Fine-Mesh Transport Solution

Assume that the reference fine-mesh transport solution of a given problem is known from calculations by means of some transport differencing method, and we have the fine-mesh transport solution defined by fine-mesh eigenvalue k_{eff}^{fm}, discrete grid functions of fine-mesh scalar flux $\phi_h^{g,fm}$, and current $J_h^{g,fm}$, which are defined as

$$J_h^{g,fm} = \{J_{i-1/2}^{g,fm}, i = 1, ..., N_x^{fm} + 1\}\,, \tag{5.9}$$

$$\phi_h^{g,fm} = \{\phi_i^{g,fm}, i = 1, ..., N_x^{fm};\ \phi_{j-1/2}^{g,fm}, i = 1, ..., N_x^{fm} + 1\}\,. \tag{5.10}$$

where the fine mesh is given by $\{x_{i-1/2}^{fm},\ i = 1, ..., N_x^{fm} + 1,\ x_{1/2}^{fm} = 0,\ x_{N_x^{fm}+1/2}^{fm} = X\}$.

5.4 Coarse-Mesh Finite-Element Discretization Method for the LOQD Equations

Let us define the following coarse mesh $\{x_{j-1/2},\ j=1,...,N_x^{cm}+1\}$. The width of the jth coarse-mesh interval is $H_j = x_{j+1/2} - x_{j-1/2}$. The LOQD equations are approximated by means of a coarse-mesh finite-element (CMFE) method based on the following expansion of the coarse-mesh scalar flux

$$\Phi_j^g(x) = \sum_{l=0}^{2}(2l+1)\varphi_j^{(l),g}P_l(\zeta_j(x)) + \varphi_j^{(3),g}\sinh(\varkappa_j^g(x-x_j)) + \varphi_j^{(4),g}\cosh(\varkappa_j^g(x-x_j))\,, \quad (5.11)$$

where P_l are Legendre polynomials,

$$\zeta_j(x) = 2(x-x_j)/H_j\,, \quad x_j = 0.5(x_{j+1/2}+x_{j-1/2})\,, \quad 1 \le j \le N_x^{cm}\,, \quad (5.12)$$

and

$$\varkappa_j^g = \sqrt{(\langle\Sigma_t\rangle_j^g - \langle\Sigma_{s,0}\rangle_j^{g\to g})\langle\Sigma_t\rangle_j^g / \langle E\rangle_j^g}\,. \quad (5.13)$$

Note that we use brackets $\langle\bullet\rangle$ for quantities spatially averaged over coarse cells and defined as

$$\langle\mathcal{A}\rangle_j^g = \sum_{i\in\omega_j}\mathcal{A}_i^g\phi_i^{g,fm}h_i \Big/ \sum_{i\in\omega_j}\phi_i^{g,fm}h_i\,, \quad (5.14)$$

where

$$\omega_j = \{i : x_{j-1/2} \le x_{i-1/2}^{fm} < x_{j+1/2}\} \quad (5.15)$$

is a set of indices of fine-mesh cells that belong to the jth coarse-mesh cell, $h_i = x_{i+1/2}^{fm} - x_{i-1/2}^{fm}$ is the width of the ith fine-mesh cell.

To derive a scheme for the LOQD equations, we integrate the balance equation (5.1) with weights $P_l(\zeta_j(x))$ $l=0,1,2$ over coarse interval $x_{j-1/2} \le x \le x_{j+1/2}$. Using Eq.(5.2), we get the following set of coarse-cell spatial moments of the balance equation:

$$J_{j+1/2}^g - J_{j-1/2}^g + \langle\Sigma_t\rangle_j^g H_j\Phi_j^{(0),g} = H_j\sum_{p=1}^{M_g}\langle\Sigma_{s,0}\rangle_j^{p\to g}\Phi_j^{(0),p} + \frac{H_j}{k_{eff}}\sum_{p=1}^{M_g}\langle\chi\nu_f\Sigma_f\rangle_j^{p,g}\Phi_j^{(0),p}\,, \quad (5.16)$$

$$J_{j+1/2}^g + J_{j-1/2}^g + \frac{2}{\langle\Sigma_t\rangle_j^g H_j}\left(\{E\}_j^{g,+}\Phi_j^g(x_{j+1/2}) - \{E\}_j^{g,-}\Phi_j^g(x_{j-1/2})\right) + \langle\Sigma_t\rangle_j^g H_j\Phi_j^{(1),g} = \quad (5.17)$$

$$H_j\sum_{p=1}^{M_g}\langle\Sigma_{s,0}\rangle_j^{p\to g}\Phi_j^{(1),p} + \frac{H_j}{k_{eff}}\sum_{p=1}^{M_g}\langle\chi\nu_f\Sigma_f\rangle_j^{p,g}\Phi_j^{(1),p}\,,$$

$$J_{j+1/2}^g - J_{j-1/2}^g + \frac{6}{\langle\Sigma_t\rangle_j^g H_j}\left(\{E\}_j^{g,+}\Phi_j^g(x_{j+1/2}) + \{E\}_j^{g,-}\Phi_j^g(x_{j-1/2}) - 2\langle E\rangle_j^g\Phi_j^{(0),g}\right) + \langle\Sigma_t\rangle_j^g H_j\Phi_j^{(2),g} = \quad (5.18)$$

$$H_j\sum_{p=1}^{M_g}\langle\Sigma_{s,0}\rangle_j^{p\to g}\Phi_j^{(2),p} + \frac{H_j}{k_{eff}}\sum_{p=1}^{M_g}\langle\chi\nu_f\Sigma_f\rangle_j^{p,g}\Phi_j^{(2),p}\,,$$

where

$$\Phi_j^{(l),g} = \frac{1}{H_j} \int\limits_{x_{j-1/2}}^{x_{j+1/2}} P_l(\zeta_j(x)) \Phi_j^g(x) dx \,, \quad l = 0, 1, 2 \tag{5.19}$$

are spatial moments of the coarse-mesh scalar flux. The definitions of $\{E\}_j^{g,-}$ and$\{E\}_j^{g,+}$ are given below.

On the basis of Eq. (5.2), we formulate the relationship between the current, scalar flux and its derivative at the coarse-cell edges

$$\{E\}_j^{g,-} \left. \frac{d\Phi_j^g}{dx} \right|_{x=x_{j-1/2}} + \left\{ \frac{dE}{dx} \right\}_j^{g,-} \Phi_j^g(x_{j-1/2}) + \{\Sigma_t\}_j^{g,-} J_{j-1/2}^g = 0 \,, \tag{5.20}$$

$$\{E\}_j^{g,+} \left. \frac{d\Phi_j^g}{dx} \right|_{x=x_{j+1/2}} + \left\{ \frac{dE}{dx} \right\}_j^{g,+} \Phi_j^g(x_{j+1/2}) + \{\Sigma_t\}_j^{g,+} J_{j+1/2}^g = 0 \,. \tag{5.21}$$

The coefficients of these equations are calculated by means of pin-cell average data. Such quantities are denoted by $\{\bullet\}$. Assume that there are Z_j pin cells in the jth coarse interval. We define the pin-cell averaged quantities of the following form:

$$\{\mathcal{A}\}_j^{g,pin\#m} = \sum_{i \in \omega_j^{pin\#m}} \mathcal{A}_i^g \phi_i^{g,fm} h_i \Big/ \sum_{i \in \omega_j^{pin\#m}} \phi_i^{g,fm} h_i \,, \tag{5.22}$$

where $\omega_j^{pin\#m}$ is a set of indices of fine-mesh intervals that belong to the mth pin cell. In Eqs. (5.17)-(5.21) the functional E^g and total cross section are averaged over boundary pin cells

$$\{E\}_j^{g,-} = \{E\}_j^{g,pin\#1} \,,\; \{E\}_j^{g,+} = \{E\}_j^{g,pin\#Z_j} \,,\; \{\Sigma_t\}_j^{g,-} = \{\Sigma_t\}_j^{g,pin\#1} \,,\; \{\Sigma_t\}_j^{g,+} = \{\Sigma_t\}_j^{g,pin\#Z_j} \,, \tag{5.23}$$

and

$$\left\{ \frac{dE}{dx} \right\}_j^{g,-} = 2 \left(\{E\}_j^{g,pin\#2} - \{E\}_j^{g,pin\#1} \right) \Big/ \left(H_j^{pin\#2} + H_j^{pin\#1} \right) \,, \tag{5.24}$$

$$\left\{ \frac{dE}{dx} \right\}_j^{g,+} = 2 \left(\{E\}_j^{g,pin\#Z_j} - \{E\}_j^{g,pin\#Z_j-1} \right) \Big/ \left(H_j^{pin\#Z_j} + H_j^{pin\#Z_j-1} \right) \,, \tag{5.25}$$

where $H_j^{pin\#m}$ is the width of the mth pin cell. The equations (5.20) and (5.21) with group data defined by (5.23)-(5.25) enable us to approximate the large-scale behavior of the transport solution next to boundaries of coarse intervals. Note that the homogenization algorithms developed by Kord Smith [14] use group data that is averaged over boundary pin cells.

To complete the system of discretized equations of the proposed method, we define the discontinuity conditions for the scalar flux

$$G_j^{g,+} \Phi_j^g(x_{j+1/2}) = G_{j+1}^{g,-} \Phi_{j+1}^g(x_{j+1/2}) \,, \quad j = 1, ..., N_x^{cm} - 1 \,, \tag{5.26}$$

and boundary conditions (5.3)

$$J_{1/2}^g = C_L^g G_1^{g,-} \Phi_1^g(x_{1/2}) \,, \quad J_{N_x^{cm}+1/2}^g = C_R^g G_{N_x^{cm}}^{g,+} \Phi_{N_x^{cm}}^g(x_{N_x^{cm}+1/2}) \,. \tag{5.27}$$

As a result the coarse-mesh discretization method consists of the spatial moment equations (5.16)-(5.18), equations (5.20) and (5.21) at the edges of coarse cells, the discontinuity conditions (5.26), and the QD boundary conditions (5.27). Substituting the expansion (5.11) into these equations, one obtains the final set of algebraic equations for $\varphi_j^{(l),g}$, $l = 0, ..., 4$, $j = 1, ..., N_x^{cm}$ and $J_{j-1/2}^g$, $j = 1, ..., N_x^{cm} + 1$, $(g = 1, ..., M_g)$.

The discontinuity factors are defined as the ratio

$$G_j^{g,\pm} = \phi_h^{g,fm}(x_{j\pm1/2}) \Big/ \tilde{\Phi}_j^g(x_{j\pm1/2}) \,. \tag{5.28}$$

where $\phi_h^{g,fm}(x_{j\pm1/2})$ is the fine-mesh transport scalar flux at $x = x_{j\pm1/2}$. Here we utilize an auxiliary function $\tilde{\Phi}_j^g(x)$

$$\tilde{\Phi}_j^g(x) = \sum_{l=0}^{2}(2l+1)\tilde{\varphi}_j^{(l),g} P_l(\zeta_j(x)) + \tilde{\varphi}_j^{(3),g}\sinh(\varkappa_j^g(x-x_j)) + \tilde{\varphi}_j^{(4),g}\cosh(\varkappa_j^g(x-x_j)) \tag{5.29}$$

which is the solution of Eqs. (5.17)-(5.21) in each jth coarse cell provided that the cell-edge currents, cell average scalar flux, and eigenvalue equal to their fine-mesh values.

The coarse-mesh discrete LOQD equations (5.16)-(5.18), (5.20)-(5.21), (5.26) and (5.27) are consistent with the given transport differencing method that generates the reference numerical transport solution $\phi_h^{g,fm}$ and $J_h^{g,fm}$ in the sense that the coarse-mesh solution $\Phi_j^g(x)$ preserves the average value of the fine-mesh scalar flux and reaction rates over each coarse-mesh cell, fine-mesh currents on edges of coarse cells, and fine-mesh k-eigenvalue, i.e.

$$\Phi_j^{(0),g} = \frac{1}{H_j}\sum_{i\in\omega_j}\phi_i^{fm}h_i \,, \tag{5.30}$$

$$k = k^{fm} \,, \tag{5.31}$$

$$J_{j-1/2}^g = J_h^{g,fm}(x_{j-1/2}) \,, \quad J_{j+1/2}^g = J_h^{g,fm}(x_{j+1/2}) \,, \tag{5.32}$$

$$\langle\Sigma_t\rangle_j^g H_j\Phi_j^{(0),g} = \sum_{i\in\omega_j}\Sigma_{t,i}^g\phi_i^{g,fm}h_i \,, \quad \langle\Sigma_{s,0}\rangle_j^{p\to g}\Phi_j^{(0),p}H_j = \sum_{i\in\omega_j}\Sigma_i^{p\to g}\phi_i^{p,fm}h_i \,, \tag{5.33}$$

$$\langle\chi\nu_f\Sigma_f\rangle_j^{p,g}\Phi_j^{(0),p}H_j = \sum_{i\in\omega_j}\chi_i^g\nu_{f,i}^p\Sigma_{i,f}^p\phi_i^{p,fm}h_i \,. \tag{5.34}$$

Note that in terms of spatial moments of the scalar flux, the resulting coarse-mesh finite-element method (5.16)-(5.18), (5.20)-(5.21), (5.26) and (5.27) preserves only zeroth moment of fine-mesh transport solution. Hereafter we refer to this method as CMFE-0, where the number indicates the maximum order of the spatial moment of the fine-mesh transport solution preserved by the method.

5.5 Advanced Consistent Coarse-Mesh Discretization

We now develop an advanced consistent coarse-mesh discretization method that preserves extra spatial moments of the fine-mesh transport solution, namely, first and second spatial Legendre moments of the fine-mesh scalar flux over each coarse cell,

$$\Phi_j^{(l),g} = \phi_j^{(l),g,fm} \,, \quad l = 1, 2 \,, \tag{5.35}$$

where

$$\phi_j^{(l),g,fm} = \frac{1}{H_j} \sum_{i \in \omega_j} \bar{\mathcal{P}}_i^{l,j} \phi_i^{g,fm} h_i \tag{5.36}$$

is the discrete form of spatial Legendre moments of the fine-mesh scalar flux over $x_{j-1/2} \leq x \leq x_{j+1/2}$, and

$$\bar{\mathcal{P}}_i^{l,j} = \frac{1}{h_i} \int\limits_{x_{i-1/2}^{fm}}^{x_{i+1/2}^{fm}} P_l(\zeta_j(x)) dx \,. \tag{5.37}$$

To formulate a scheme with the desired properties, we use the above method as a basis and add special consistency terms in the first and second spatial moments on the balance equations. The proposed CMFE method is defined by

$$J_{j+1/2}^g - J_{j-1/2}^g + \langle \Sigma_t \rangle_j^g H_j \Phi_j^{(0),g} = H_j \sum_{p=1}^{M_g} \langle \Sigma_{s,0} \rangle_j^{p \to g} \Phi_j^{(0),p} + \frac{H_j}{k_{eff}} \sum_{p=1}^{M_g} \langle \chi \nu_f \Sigma_f \rangle_j^{p,g} \Phi_j^{(0),p} \,, \tag{5.38}$$

$$J_{j+1/2}^g + J_{j-1/2}^g + \frac{2}{\langle \Sigma_t \rangle_j^g H_j} \left(\{E\}_j^{g,+} \Phi_j^g(x_{j+1/2}) - \{E\}_j^{g,-} \Phi_j^g(x_{j-1/2}) \right) +$$

$$\langle \Sigma_t \rangle_j^g H_j \Phi_j^{(1),g} + \left(\alpha_j^{(1),g} + \beta_{t,j}^{(1),g} \right) H_j \Phi_j^{(0),g} = \tag{5.39}$$

$$H_j \sum_{p=1}^{M_g} \langle \Sigma_{s,0} \rangle_j^{p \to g} \Phi_j^{(1),p} + \frac{H_j}{k_{eff}} \sum_{p=1}^{M_g} \langle \chi \nu_f \Sigma_f \rangle_j^{p,g} \Phi_j^{(1),p} + H_j \sum_{p=1}^{M_g} \left(\beta_{s,j}^{(1),p \to g} + \frac{1}{k_{eff}} \beta_{f,j}^{(1),p,g} \right) \Phi_j^{(0),p} \,,$$

$$J_{j+1/2}^g - J_{j-1/2}^g + \frac{6}{\langle \Sigma_t \rangle_j^g H_j} \left(\{E\}_j^{g,+} \Phi_j^g(x_{j+1/2}) + \{E\}_j^{g,-} \Phi_j^g(x_{j-1/2}) - 2 \langle E \rangle_j^g \Phi_j^{(0),g} \right) +$$

$$\langle \Sigma_t \rangle_j^g H_j \Phi_j^{(2),g} + \left(\alpha_j^{(2),g} + \beta_{t,j}^{(2),g} \right) H_j \Phi_j^{(0),g} = \tag{5.40}$$

$$H_j \sum_{p=1}^{M_g} \langle \Sigma_{s,0} \rangle_j^{p \to g} \Phi_j^{(2),p} + \frac{H_j}{k_{eff}} + \sum_{p=1}^{M_g} \langle \chi \nu_f \Sigma_f \rangle_j^{p,g} \Phi_j^{(2),p} H_j \sum_{p=1}^{M_g} \left(\beta_{s,j}^{(2),p \to g} + \frac{1}{k_{eff}} \beta_{f,j}^{(2),p,g} \right) \Phi_j^{(0),p} \,,$$

$$\{E\}_j^{g,-} \left. \frac{d\Phi_j^g}{dx} \right|_{x = x_{j-1/2}} + \left\{ \frac{dE}{dx} \right\}_j^{g,-} \Phi_j^g(x_{j-1/2}) + \{\Sigma_t\}_j^{g,-} J_{j-1/2}^g = 0 \,, \tag{5.41}$$

$$\{E\}_j^{g,+} \left. \frac{d\Phi_j^g}{dx} \right|_{x = x_{j+1/2}} + \left\{ \frac{dE}{dx} \right\}_j^{g,+} \Phi_j^g(x_{j+1/2}) + \{\Sigma_t\}_j^{g,+} J_{j+1/2}^g = 0 \,. \tag{5.42}$$

$$\widehat{G}_j^{g,+} \Phi_j^g(x_{j+1/2}) = \widehat{G}_{j+1}^{g,-} \Phi_{j+1}^g(x_{j+1/2}) \,, \quad j = 1, ..., N_x^{cm} - 1 \,, \tag{5.43}$$

$$J_{1/2}^g = C_L^g \widehat{G}_1^{g,-} \Phi_1^g(x_{1/2}) \,, \quad J_{N_x^{cm}+1/2}^g = C_R^g \widehat{G}_{N_x^{cm}}^{g,+} \Phi_{N_x^{cm}}^g(x_{N_x^{cm}+1/2}) \,. \tag{5.44}$$

Here we use new discontinuity factors $\widehat{G}^{g,\pm}$ that are determined by means of different auxiliary function compared to one used to calculate $G^{g,\pm}$ in the CMFE-0 method.

The $\alpha_j^{(l),g}$, $\beta_{t,j}^{(l),g}$, $\beta_{s,j}^{(l),p \to g}$ and $\beta_{f,j}^{(l),p,g}$ are consistency terms that are defined such that the resulting scheme preserves: (i) fine-mesh values of the transport currents at edges of

coarse cells, (ii) zeroth, first and second spatial Legendre moments of the fine-mesh transport scalar flux over each coarse cell. To derive such terms and get spatial moments equations consistent with the fine-mesh discretization scheme, we performed the operation of taking spatial moments of the balance equation (5.1) in discrete form by multiplying the fine-mesh discretized balance equation by $\bar{P}_i^{l,j}$ l=1,2, (Eq.(5.37)) and summing it over all fine-mesh cells that belong to the jth coarse interval

$$\sum_{i\in\omega_j}\bar{\mathcal{P}}_i^{l,j}\left(J_{i+1/2}^{g,fm}-J_{i-1/2}^{g,fm}\right)+\sum_{i\in\omega_j}\bar{\mathcal{P}}_i^{l,j}\Sigma_{t,i}^{g}\phi_i^{g,fm}h_i=$$

$$\sum_{p=1}^{M_g}\sum_{i\in\omega_j}\bar{\mathcal{P}}_i^{l,j}\Sigma_{s,0,i}^{p\to g}\phi_i^{p,fm}h_i+\frac{1}{k_{eff}}\sum_{p=1}^{M_g}\sum_{i\in\omega_j}\bar{\mathcal{P}}_i^{l,j}\chi_i^{g}\nu_{f,i}^{p}\Sigma_{f,i}^{p}\phi_i^{p,fm}h_i\,, \tag{5.45}$$

$$j=1,...,N_x^{cm}\,.$$

As a result we define the following functionals:

$$\alpha_j^{(1),g}=\left[\sum_{i\in\omega_j}\bar{\mathcal{P}}_i^{1,j}\left(J_{i+1/2}^{g,fm}-J_{i-1/2}^{g,fm}\right)-J_h^{g,fm}(x_{j+1/2})-J_h^{g,fm}(x_{j-1/2})-\right.$$

$$\left.\frac{2}{\langle\Sigma_t\rangle_j^g H_j}\left(\{E\}_j^{g,+}\frac{\phi_h^{g,fm}(x_{j+1/2})}{\widehat{G}_j^{g,+}}-\{E\}_j^{g,-}\frac{\phi_h^{g,fm}(x_{j-1/2})}{\widehat{G}_j^{g,-}}\right)\right]\Bigg/\sum_{i\in\omega_j}\phi_i^{g,fm}h_i\,, \tag{5.46}$$

$$\alpha_j^{(2),g}=\left[\sum_{i\in\omega_j}\bar{\mathcal{P}}_i^{2,j}\left(J_{i+1/2}^{g,fm}-J_{i-1/2}^{g,fm}\right)-J_h^{g,fm}(x_{j+1/2})+J_h^{g,fm}(x_{j-1/2})-\right.$$

$$\left.\frac{6}{\langle\Sigma_t\rangle_j^g H_j}\left(\{E\}_j^{g,+}\frac{\phi_h^{g,fm}(x_{j+1/2})}{\widehat{G}_j^{g,+}}+\{E\}_j^{g,-}\frac{\phi_h^{g,fm}(x_{j-1/2})}{\widehat{G}_j^{g,-}}-2\langle E\rangle_j^g\phi_j^{(0),g,fm}\right)\right]\Bigg/\sum_{i\in\omega_j}\phi_i^{g,fm}h_i\,, \tag{5.47}$$

$$\beta_{t,j}^{(l),g}=\sum_{i\in\omega_j}\left[\Sigma_{t,i}^{g}-\langle\Sigma_t\rangle_j^g\right]\bar{\mathcal{P}}_i^{l,j}\phi_i^{g,fm}h_i\Bigg/\sum_{i\in\omega_j}\phi_i^{g,fm}h_i\,, \tag{5.48}$$

$$\beta_{s,j}^{(l),p\to g}=\sum_{i\in\omega_j}\left[\Sigma_{s,0,i}^{p\to g}-\langle\Sigma_{s,0}\rangle_j^{p\to g}\right]\bar{\mathcal{P}}_i^{l,j}\phi_i^{p,fm}h_i\Bigg/\sum_{i\in\omega_j}\phi_i^{p,fm}h_i\,, \tag{5.49}$$

$$\beta_{f,j}^{(l),p,g}=\sum_{i\in\omega_j}\left[\chi_i^{g}\nu_{f,i}^{p}\Sigma_{f,i}^{p}-\langle\chi\nu_f\Sigma_f\rangle_j^{p,g}\right]\bar{\mathcal{P}}_i^{l,j}\phi_i^{p,fm}h_i\Bigg/\sum_{i\in\omega_j}\phi_i^{p,fm}h_i\,, \tag{5.50}$$

$$l=1,2\,.$$

Note that we assumed that the discontinuity factors are known.

To define the discontinuity factors $\widehat{G}_j^{g,\pm}$, we use an auxiliary function

$$\widehat{\Phi}_j^g(x)=\sum_{l=0}^{2}(2l+1)\widehat{\varphi}_j^{(l),g}P_l(\zeta_j(x))+\widehat{\varphi}_j^{(3),g}\sinh(\varkappa_j^g(x-x_j))+\widehat{\varphi}_j^{(4),g}\cosh(\varkappa_j^g(x-x_j)) \tag{5.51}$$

which is the solution of Eqs. (5.38)-(5.44) for the jth coarse cell such that it reproduces the average value of the fine-mesh transport scalar flux, the first and second spatial Legendre moments of the fine-mesh transport scalar flux, and currents on edges of this coarse cell. To calculate the coefficients of expansion of $\widehat{\Phi}_j^g(x)$, we need to solve the following set of equations in terms of $\widehat{\varphi}_j^{(l),g}$, $l = 0, ..., 4$ in the jth cell:

$$\{E\}_j^{g,-} \left.\frac{d\widehat{\Phi}_j^g}{dx}\right|_{x=x_{j-1/2}} + \left\{\frac{dE}{dx}\right\}_j^{g,=} \widehat{\Phi}_j^g(x_{j-1/2}) = -\{\Sigma_t\}_j^{g,-} J_h^{g,fm}(x_{j-1/2})\,, \tag{5.52}$$

$$\{E\}_j^{g,+} \left.\frac{d\widehat{\Phi}_j^g}{dx}\right|_{x=x_{j+1/2}} + \left\{\frac{dE}{dx}\right\}_j^{g,+} \widehat{\Phi}_j^g(x_{j+1/2}) = -\{\Sigma_t\}_j^{g,+} J_h^{g,fm}(x_{j+1/2})\,, \tag{5.53}$$

$$\widehat{\Phi}_j^{(l),g} = \phi_j^{(l),g,fm}\,, \quad l = 0, 1, 2\,. \tag{5.54}$$

The discontinuity factors are defined as the ratio

$$\widehat{G}_j^{g,\pm} = \phi_h^{g,fm}(x_{j\pm1/2}) \Big/ \widehat{\Phi}_j^g(x_{j\pm1/2})\,. \tag{5.55}$$

The following theorem is true for the derived advanced consistent coarse-mesh discretization method:

Theorem *The coarse-mesh discrete low-order QD equations (5.38)-(5.44), with discontinuity factors (5.55), cross sections and functionals defined by (5.14), (5.23)-(5.25) and (5.46)-(5.50) are consistent with the given transport differencing method that generates the reference fine-mesh transport solution $\phi_h^{g,fm}$ and $J_h^{g,fm}$ in the sense that the coarse-mesh solution $\Phi_j^g(x)$ preserves the average value of the fine-mesh scalar flux and reaction rates over each coarse-mesh cell, the first and second spatial Legendre moments of the fine-mesh scalar flux over coarse intervals, fine-mesh currents at edges of coarse cells, and fine-mesh k-eigenvalue, i.e.*

$$\Phi_j^{(l),g} = \phi_j^{(l),g,fm}\,, \quad l = 0, 1, 2\,, \quad J_{j\pm1/2}^g = J_h^{g,fm}(x_{j\pm1/2})\,, \quad k_{eff} = k_{eff}^{fm}\,, \tag{5.56}$$

$$\langle\Sigma_t\rangle_j^g H_j \Phi_j^{(0),g} = \sum_{i\in\omega_j} \Sigma_{t,i}^g \phi_i^{g,fm} h_i\,, \quad \langle\Sigma_{s,0}\rangle_j^{p\to g} H_j \Phi_j^{(0),p} = \sum_{i\in\omega_j} \Sigma_{s,0,i}^{p\to g} \phi_i^{p,fm} h_i\,, \tag{5.57}$$

$$\langle\chi\nu_f\Sigma_f\rangle_j^{p,g} H_j \Phi_j^{(0),p} = \sum_{i\in\omega_j} \chi_i^g \nu_{f,i}^p \Sigma_{f,i}^p \phi_i^{p,fm} h_i\,. \tag{5.58}$$

Thus, the resulting coarse-mesh finite-element method preserves up to the second Legendre spatial moment of the fine-mesh transport scalar flux over coarse-cells. We refer to this method as CMFE-2.

5.6 Numerical Results

5.6.1 Test Problems that Simulate the Interaction of MOX and Uranium Assemblies

We present numerical results of Kord Smith's test problems in 1D slab geometry with two energy groups [14]. In these test problems, model uranium and MOX assemblies are used.

There are two half-assemblies next to each other with reflective boundary conditions on the outside. A MOX half-assembly is on the left and a uranium half-assembly is on the right. Each half-assembly consists of 8 pin cells. A fuel pin cell is 1.25 cm wide with fuel pin (0.625 cm) located in its center and surrounded by water. The half-assembly width is 10 cm. Table 5.1 shows cross sections of different types of fuels and water. Figures 5.1-5.5 demonstrate design of assemblies for each test problem. Test 1 and 2 consists of assemblies with the same type of fuel pins. Test 3 and 4 differ from Test 2 by design of MOX assemblies. These tests simulate variation in enrichment near the interface with a uranium assembly. Test 5 has a MOX assembly with a water hole.

The fine-mesh solutions were calculated by the QD method using a second order finite-volume scheme for the LOQD equations and step characteristic method for the transport equation to calculate the QD functionals [13]. The fine spatial mesh consists of 128 equal cells, i.e. 8 mesh cells per pin cell. The angular mesh has 10 intervals. The multiplication factor equals 1.5. The coarse mesh consists of one cell per half-assembly; thus, $N_x^{cm} = 2$.

Figures 5.6-5.15 show the fine-mesh transport scalar fluxes versus position, pin-cell average values of the scalar flux represented as a histogram plot, and coarse-mesh solutions obtained by means of the CMFE-0 and CMFE-2 methods. Tables 5.2-5.11 present the relative difference in pin-cell average values of the fine-mesh transport solution and coarse-mesh LOQD solution calculated by the CMFE-0 and CMFE-2 methods. In each assembly pin cells are numbered from left to right. The largest absolute values of relative differences in pin-cell average values of the fine-mesh transport solution and coarse-mesh LOQD solution in MOX assemblies are listed in Table 5.12.

The results of Tests 1 an 2 demonstrate that both methods generate very accurate coarse-mesh solutions, if assemblies consist of the same type of fuel pins. In Tests 3 and 4 that simulate spatial variation of fuel enrichment in MOX assembly, the CMFE-2 method approximates accurately the large-scale behavior of the transport solution characterized by the pin-cell average values. The resulting coarse-mesh solution of the CMFE-2 is significantly more accurate compared to the coarse-mesh solution obtained by the CMFE-0 method that preserves only zeroth spatial moment of the scalar flux. In Test 5 with the water hole in the MOX assembly the CMFE-2 method mimics the large-scale behavior of the fine-mesh transport solution and generates coarse-mesh solution with sufficiently good accuracy. These results demonstrate that the preservation of extra spatial moments of the fine-mesh transport solution leads to significant improvement in accuracy of the coarse-mesh solution.

5.6.2 Stability of Consistent Discretization to Variation of Group Data

In calculations of the presented test problems, all necessary assembly-averaged cross sections and functionals (discontinuity factors, quasidiffusion functionals, consistency terms, etc.) were exact, because they were generated by means of fine-mesh transport solutions of corresponding coupled assemblies. In terms of the methodology for full-core calculations described above, this means that exact albedos were used in single-assembly calculations to generate assembly group data. However, in realistic calculations the assembly group data are arranged in form of tables, and necessary quantities are determined by means of interpolation of tabulated data. Thus, it is interesting to study the stability of solution obtained

by means of CMFE-2 to variation in cross sections and functionals of this method, to find out how this can influence the accuracy of the coarse-mesh solution generated by CMFE-2.

To perform this kind of analysis, we calculated Test 3 with the group data for the MOX assembly obtained by using perturbed averaging function. The group data were obtained by means of transport solutions of two assembly problems similar to Test 3 but in which the neighboring uranium assembly had perturbed σ_f^2 (Test 6) or ν_f^2 (Tests 7), namely, decreased by 5% and 10%. Figures 5.16-5.19 show the results of Tests 6 and 7.

From these results we notice that the obtained solutions in each case is very close to the solution of Test 3 in which exact group data were used. Thus, the proposed advanced consistent coarse-mesh discretization method, CMFE-2, demonstrates stability to variation in averaging function that is used for calculating group data, and, as a result, to variation in group data.

5.7 Conclusions

We have presented a high-order coarse-mesh finite-element (CMFE-0) method for discretization of the QD low-order equations that is consistent with the given fine-mesh transport differencing method in the sense that it preserves the fine-mesh values of cell-average scalar flux, cell-edge current, multiplication factor, and reaction rates. On the basis of this method, we have developed an advanced consistent coarse-mesh finite-element (CMFE-2) method that preserves extra two spatial Legendre moments of the fine-mesh transport scalar flux over coarse-mesh cells.

We have analyzed the developed methods on a set of test problems that simulate the interaction of MOX and uranium assemblies. These tests included assemblies with enrichment variations, and water holes that introduce within-assembly flux variations. In spite of this the CMFE-2 method is able to generate solution that mimic accurately the large-scale behavior of the transport solution within assembly.

The proposed methodology can be extended to multidimensional geometries, multigroup case, finite-element methods based on higher order expansions of the coarse-mesh scalar flux that creates an option of preserving more spatial moments of the fine-mesh transport solution over coarse cells. The developed method is a part of a new methodology for reactor core calculations, and this method will be coupled with other pieces of this methodology, including usage of group data obtained by means of single-assembly calculations that use efficient albedo boundary conditions. Another important issue is possibility of improvement of pin-power reconstruction using the discretization methods that preserve extra spatial moments of the fine-mesh transport solution within assembly. We are working now on such extensions.

Table 5.1: **Cross Sections Data**

Notation	Material	Σ_t^1	$\Sigma_{s,0}^{1\to1}$	$\Sigma_{s,0}^{1\to2}$	Σ_f^1	ν_f^1	Σ_t^2	$\Sigma_{s,0}^{2\to2}$	$\Sigma_{s,0}^{2\to1}$	Σ_f^2	ν_f^2
M1	MOX fuel	0.2	0.2	0	0	0	0.6	0	0	0.6	1.5
M2	MOX fuel	0.2	0.185	0.015	0	0	1.2	0.9	0	0.3	1.5
M3	MOX fuel	0.2	0.185	0.015	0	0	1.13	0.9	0	0.23	1.5
M4	MOX fuel	0.2	0.185	0.015	0	0	1.07	0.9	0	0.17	1.5
U1	Uranium fuel	0.2	0.2	0	0	0	0.2	0	0	0.2	1.5
U2	Uranium fuel	0.2	0.185	0.015	0	0	1.0	0.9	0	0.1	1.5
W	Water	0.2	0.17	0.03	0	0	1.1	1.1	0	0	0

pin 1	pin 2	pin 3	pin 4	pin 5	pin 6	pin 7	pin 8	pin 1	pin 2	pin 3	pin 4	pin 5	pin 6	pin 7	pin 8
M1	M1	M1	M1	M1	M1	M1	M1	U1	U1	U1	U1	U1	U1	U1	U1

Figure 5.1: Test 1, design of assemblies.

pin 1	pin 2	pin 3	pin 4	pin 5	pin 6	pin 7	pin 8	pin 1	pin 2	pin 3	pin 4	pin 5	pin 6	pin 7	pin 8
M2	M2	M2	M2	M2	M2	M2	M2	U2	U2	U2	U2	U2	U2	U2	U2

Figure 5.2: Test 2, design of assemblies.

pin 1	pin 2	pin 3	pin 4	pin 5	pin 6	pin 7	pin 8	pin 1	pin 2	pin 3	pin 4	pin 5	pin 6	pin 7	pin 8
M2	M2	M2	M2	M2	M2	M2	U2	U2	U2	U2	U2	U2	U2	U2	U2

Figure 5.3: Test 3, design of assemblies.

pin 1	pin 2	pin 3	pin 4	pin 5	pin 6	pin 7	pin 8	pin 1	pin 2	pin 3	pin 4	pin 5	pin 6	pin 7	pin 8
M2	M2	M2	M2	M2	M2	M3	M4	U2	U2	U2	U2	U2	U2	U2	U2

Figure 5.4: Test 4, design of assemblies.

pin 1	pin 2	pin 3	pin 4	pin 5	pin 6	pin 7	pin 8	pin 1	pin 2	pin 3	pin 4	pin 5	pin 6	pin 7	pin 8
M2	M2	M2	W	W	M2	M2	M2	U2	U2	U2	U2	U2	U2	U2	U2

Figure 5.5: Test 5, design of assemblies.

Table 5.2: **Test 1. CMFE-0 Method, Relative Difference in Pin-Cell Average Values.**

Assembly	Group	Pin # 1	Pin # 2	Pin # 3	Pin # 4	Pin # 5	Pin # 6	Pin # 7	Pin # 8
MOX	1	$1{\cdot}10^{-4}$	$4{\cdot}10^{-4}$	$5{\cdot}10^{-4}$	$2{\cdot}10^{-4}$	$-4{\cdot}10^{-4}$	$-9{\cdot}10^{-4}$	$-4{\cdot}10^{-4}$	$5{\cdot}10^{-4}$
MOX	2	$3{\cdot}10^{-3}$	$4{\cdot}10^{-3}$	$4{\cdot}10^{-3}$	$4{\cdot}10^{-3}$	$4{\cdot}10^{-3}$	$1{\cdot}10^{-3}$	$-5{\cdot}10^{-3}$	$-1{\cdot}10^{-2}$
U	1	$6{\cdot}10^{-4}$	$6{\cdot}10^{-6}$	$8{\cdot}10^{-5}$	$4{\cdot}10^{-5}$	$-1{\cdot}10^{-4}$	$-2{\cdot}10^{-4}$	$-2{\cdot}10^{-4}$	$-1{\cdot}10^{-4}$
U	2	$1{\cdot}10^{-2}$	$4{\cdot}10^{-3}$	$-1{\cdot}10^{-3}$	$-3{\cdot}10^{-3}$	$-3{\cdot}10^{-3}$	$-2{\cdot}10^{-3}$	$-2{\cdot}10^{-3}$	$-3{\cdot}10^{-3}$

Table 5.3: **Test 1. CMFE-2 Method. Relative Difference in Pin-Cell Average Values.**

Assembly	Group	Pin # 1	Pin # 2	Pin # 3	Pin # 4	Pin # 5	Pin # 6	Pin # 7	Pin # 8
MOX	1	$-7{\cdot}10^{-4}$	$3{\cdot}10^{-5}$	$6{\cdot}10^{-4}$	$6{\cdot}10^{-4}$	$4{\cdot}10^{-5}$	$-5{\cdot}10^{-4}$	$-4{\cdot}10^{-4}$	$3{\cdot}10^{-4}$
MOX	2	$-4{\cdot}10^{-3}$	$-2{\cdot}10^{-3}$	$7{\cdot}10^{-4}$	$3{\cdot}10^{-3}$	$4{\cdot}10^{-3}$	$4{\cdot}10^{-3}$	$-3{\cdot}10^{-4}$	$-5{\cdot}10^{-3}$
U	1	$-3{\cdot}10^{-4}$	$-4{\cdot}10^{-4}$	$2{\cdot}10^{-4}$	$5{\cdot}10^{-4}$	$5{\cdot}10^{-4}$	$2{\cdot}10^{-4}$	$-2{\cdot}10^{-4}$	$-4{\cdot}10^{-4}$
U	2	$-2{\cdot}10^{-2}$	$1{\cdot}10^{-2}$	$1{\cdot}10^{-2}$	$2{\cdot}10^{-3}$	$-6{\cdot}10^{-3}$	$-7{\cdot}10^{-3}$	$-2{\cdot}10^{-3}$	$4{\cdot}10^{-3}$

Table 5.4: **Test 2. CMFE-0 Method. Relative Difference in Pin-Cell Average Values.**

Assembly	Group	Pin # 1	Pin # 2	Pin # 3	Pin # 4	Pin # 5	Pin # 6	Pin # 7	Pin # 8
MOX	1	$5{\cdot}10^{-5}$	$5{\cdot}10^{-4}$	$6{\cdot}10^{-4}$	$1{\cdot}10^{-4}$	$-7{\cdot}10^{-4}$	$-1{\cdot}10^{-3}$	$-3{\cdot}10^{-4}$	$9{\cdot}10^{-4}$
MOX	2	$-2{\cdot}10^{-4}$	$-2{\cdot}10^{-4}$	$-2{\cdot}10^{-4}$	$-2{\cdot}10^{-4}$	$-1{\cdot}10^{-4}$	$-3{\cdot}10^{-4}$	$-1{\cdot}10^{-3}$	$2{\cdot}10^{-3}$
U	1	$5{\cdot}10^{-4}$	$-3{\cdot}10^{-4}$	$-8{\cdot}10^{-5}$	$7{\cdot}10^{-5}$	$-2{\cdot}10^{-5}$	$-1{\cdot}10^{-4}$	$-3{\cdot}10^{-5}$	$8{\cdot}10^{-5}$
U	2	$5{\cdot}10^{-4}$	$1{\cdot}10^{-4}$	$-7{\cdot}10^{-4}$	$-4{\cdot}10^{-4}$	$8{\cdot}10^{-5}$	$3{\cdot}10^{-4}$	$2{\cdot}10^{-4}$	$-5{\cdot}10^{-5}$

Table 5.5: **Test 2. CMFE-2 Method. Relative Difference in Pin-Cell Average Values.**

Assembly	Group	Pin # 1	Pin # 2	Pin # 3	Pin # 4	Pin # 5	Pin # 6	Pin # 7	Pin # 8
MOX	1	$-7{\cdot}10^{-4}$	$1{\cdot}10^{-4}$	$8{\cdot}10^{-4}$	$6{\cdot}10^{-4}$	$-1{\cdot}10^{-4}$	$-7{\cdot}10^{-4}$	$-3{\cdot}10^{-4}$	$4{\cdot}10^{-4}$
MOX	2	$-3{\cdot}10^{-3}$	$-6{\cdot}10^{-4}$	$2{\cdot}10^{-3}$	$3{\cdot}10^{-3}$	$3{\cdot}10^{-3}$	$9{\cdot}10^{-4}$	$-2{\cdot}10^{-3}$	$-2{\cdot}10^{-3}$
U	1	$-2{\cdot}10^{-4}$	$-7{\cdot}10^{-4}$	$1{\cdot}10^{-4}$	$6{\cdot}10^{-4}$	$6{\cdot}10^{-4}$	$2{\cdot}10^{-4}$	$-2{\cdot}10^{-4}$	$-5{\cdot}10^{-4}$
U	2	$-1{\cdot}10^{-3}$	$-2{\cdot}10^{-4}$	$4{\cdot}10^{-5}$	$8{\cdot}10^{-4}$	$1{\cdot}10^{-3}$	$8{\cdot}10^{-4}$	$-2{\cdot}10^{-4}$	$1{\cdot}10^{-3}$

Table 5.6: **Test 3. CMFE-0 Method. Relative Difference in Pin-Cell Average Values.**

Assembly	Group	Pin # 1	Pin # 2	Pin # 3	Pin # 4	Pin # 5	Pin # 6	Pin # 7	Pin # 8
MOX	1	$4{\cdot}10^{-3}$	$5{\cdot}10^{-3}$	$5{\cdot}10^{-3}$	$4{\cdot}10^{-3}$	$2{\cdot}10^{-3}$	$5{\cdot}10^{-4}$	$-1{\cdot}10^{-3}$	$-2{\cdot}10^{-2}$
MOX	2	$-1{\cdot}10^{-1}$	$-1{\cdot}10^{-1}$	$-1{\cdot}10^{-1}$	$-1{\cdot}10^{-1}$	$-9{\cdot}10^{-2}$	$-2{\cdot}10^{-2}$	$1{\cdot}10^{-1}$	$3{\cdot}10^{-1}$
U	1	$-4{\cdot}10^{-4}$	$-3{\cdot}10^{-4}$	$6{\cdot}10^{-5}$	$2{\cdot}10^{-4}$	$2{\cdot}10^{-4}$	$1{\cdot}10^{-4}$	$9{\cdot}10^{-5}$	$7{\cdot}10^{-5}$
U	2	$5{\cdot}10^{-4}$	$-3{\cdot}10^{-4}$	$-4{\cdot}10^{-4}$	$-2{\cdot}10^{-4}$	$4{\cdot}10^{-5}$	$2{\cdot}10^{-4}$	$1{\cdot}10^{-4}$	$5{\cdot}10^{-5}$

Table 5.7: **Test 3. CMFE-2 Method. Relative Difference in Pin-Cell Average Values.**

Assembly	Group	Pin # 1	Pin # 2	Pin # 3	Pin # 4	Pin # 5	Pin # 6	Pin # 7	Pin # 8
MOX	1	$1{\cdot}10^{-3}$	$-9{\cdot}10^{-5}$	$-2{\cdot}10^{-3}$	$-2{\cdot}10^{-3}$	$-1{\cdot}10^{-3}$	$3{\cdot}10^{-3}$	$8{\cdot}10^{-3}$	$-7{\cdot}10^{-3}$
MOX	2	$-5{\cdot}10^{-2}$	$1{\cdot}10^{-2}$	$6{\cdot}10^{-2}$	$5{\cdot}10^{-2}$	$2{\cdot}10^{-3}$	$-6{\cdot}10^{-2}$	$-6{\cdot}10^{-2}$	$5{\cdot}10^{-2}$
U	1	$-4{\cdot}10^{-4}$	$-2{\cdot}10^{-4}$	$3{\cdot}10^{-4}$	$5{\cdot}10^{-4}$	$3{\cdot}10^{-4}$	$1{\cdot}10^{-4}$	$-2{\cdot}10^{-4}$	$-3{\cdot}10^{-4}$
U	2	$-1{\cdot}10^{-3}$	$-7{\cdot}10^{-4}$	$2{\cdot}10^{-4}$	$1{\cdot}10^{-3}$	$1{\cdot}10^{-3}$	$8{\cdot}10^{-4}$	$-3{\cdot}10^{-4}$	$-1{\cdot}10^{-3}$

Table 5.8: **Test 4. CMFE-0 Method. Relative Difference in Pin-Cell Average Values.**

Assembly	Group	Pin # 1	Pin # 2	Pin # 3	Pin # 4	Pin # 5	Pin # 6	Pin # 7	Pin # 8
MOX	1	$3{\cdot}10^{-3}$	$2{\cdot}10^{-3}$	$2{\cdot}10^{-3}$	$2{\cdot}10^{-3}$	$2{\cdot}10^{-3}$	$2{\cdot}10^{-3}$	$-9{\cdot}10^{-3}$	$-5{\cdot}10^{-3}$
MOX	2	$-1{\cdot}10^{-1}$	$-1{\cdot}10^{-1}$	$-1{\cdot}10^{-1}$	$-8{\cdot}10^{-2}$	$-5{\cdot}10^{-2}$	$3{\cdot}10^{-2}$	$1{\cdot}10^{-1}$	$1{\cdot}10^{-1}$
U	1	$2{\cdot}10^{-4}$	$-3{\cdot}10^{-4}$	$-3{\cdot}10^{-5}$	$1{\cdot}10^{-4}$	$4{\cdot}10^{-5}$	$-4{\cdot}10^{-5}$	$4{\cdot}10^{-6}$	$7{\cdot}10^{-5}$
U	2	$2{\cdot}10^{-4}$	$9{\cdot}10^{-5}$	$-5{\cdot}10^{-4}$	$-3{\cdot}10^{-4}$	$6{\cdot}10^{-5}$	$3{\cdot}10^{-4}$	$2{\cdot}10^{-4}$	$-1{\cdot}10^{-5}$

Table 5.9: **Test 4. CMFE-2 Method. Relative Difference in Pin-Cell Average Values.**

Assembly	Group	Pin # 1	Pin # 2	Pin # 3	Pin # 4	Pin # 5	Pin # 6	Pin # 7	Pin # 8
MOX	1	$5{\cdot}10^{-4}$	$-6{\cdot}10^{-4}$	$-1{\cdot}10^{-3}$	$-5{\cdot}10^{-4}$	$2{\cdot}10^{-3}$	$4{\cdot}10^{-3}$	$-5{\cdot}10^{-3}$	$1{\cdot}10^{-3}$
MOX	2	$-1{\cdot}10^{-2}$	$8{\cdot}10^{-3}$	$2{\cdot}10^{-2}$	$3{\cdot}10^{-3}$	$-2{\cdot}10^{-2}$	$-2{\cdot}10^{-2}$	$3{\cdot}10^{-2}$	$-1{\cdot}10^{-2}$
U	1	$-3{\cdot}10^{-4}$	$-5{\cdot}10^{-4}$	$2{\cdot}10^{-4}$	$6{\cdot}10^{-4}$	$5{\cdot}10^{-4}$	$2{\cdot}10^{-4}$	$-2{\cdot}10^{-4}$	$-4{\cdot}10^{-4}$
U	2	$-1{\cdot}10^{-3}$	$-3{\cdot}10^{-4}$	$1{\cdot}10^{-4}$	$9{\cdot}10^{-4}$	$1{\cdot}10^{-3}$	$8{\cdot}10^{-4}$	$-3{\cdot}10^{-4}$	$-1{\cdot}10^{-3}$

Table 5.10: **Test 5. CMFE-0 Method. Relative Difference in Pin-Cell Average Values.**

Assembly	Group	Pin # 1	Pin # 2	Pin # 3	Pin # 4	Pin # 5	Pin # 6	Pin # 7	Pin # 8
MOX	1	$1{\cdot}10^{-2}$	$2{\cdot}10^{-2}$	$1{\cdot}10^{-2}$	$-6{\cdot}10^{-2}$	$-6{\cdot}10^{-2}$	$1{\cdot}10^{-2}$	$2{\cdot}10^{-2}$	$2{\cdot}10^{-2}$
MOX	2	$-4{\cdot}10^{-1}$	$-3{\cdot}10^{-1}$	$3{\cdot}10^{-2}$	$3{\cdot}10^{-1}$	$3{\cdot}10^{-1}$	$2{\cdot}10^{-3}$	$-3{\cdot}10^{-1}$	$-4{\cdot}10^{-1}$
U	1	$1{\cdot}10^{-3}$	$-3{\cdot}10^{-4}$	$-2{\cdot}10^{-4}$	$-9{\cdot}10^{-5}$	$-2{\cdot}10^{-4}$	$-3{\cdot}10^{-4}$	$-1{\cdot}10^{-4}$	$4{\cdot}10^{-5}$
U	2	$3{\cdot}10^{-4}$	$4{\cdot}10^{-4}$	$-5{\cdot}10^{-4}$	$-4{\cdot}10^{-4}$	$4{\cdot}10^{-6}$	$2{\cdot}10^{-4}$	$1{\cdot}10^{-4}$	$-1{\cdot}10^{-4}$

Table 5.11: **Test 5. CMFE-2 Method. Relative Difference in Pin-Cell Average Values.**

Assembly	Group	Pin # 1	Pin # 2	Pin # 3	Pin # 4	Pin # 5	Pin # 6	Pin # 7	Pin # 8
MOX	1	$-9{\cdot}10^{-3}$	$1{\cdot}10^{-2}$	$3{\cdot}10^{-2}$	$-3{\cdot}10^{-2}$	$-3{\cdot}10^{-2}$	$3{\cdot}10^{-2}$	$1{\cdot}10^{-2}$	$-8{\cdot}10^{-3}$
MOX	2	$1{\cdot}10^{-1}$	$-1{\cdot}10^{-1}$	$-2{\cdot}10^{-2}$	$1{\cdot}10^{-1}$	$1{\cdot}10^{-1}$	$-1{\cdot}10^{-1}$	$-1{\cdot}10^{-1}$	$-7{\cdot}10^{-2}$
U	1	$-1{\cdot}10^{-4}$	$-8{\cdot}10^{-4}$	$5{\cdot}10^{-5}$	$6{\cdot}10^{-4}$	$6{\cdot}10^{-4}$	$3{\cdot}10^{-4}$	$-2{\cdot}10^{-4}$	$-5{\cdot}10^{-4}$
U	2	$-1{\cdot}10^{-3}$	$-1{\cdot}10^{-4}$	$6{\cdot}10^{-5}$	$8{\cdot}10^{-4}$	$1{\cdot}10^{-3}$	$8{\cdot}10^{-4}$	$-2{\cdot}10^{-4}$	$-1{\cdot}10^{-3}$

Table 5.12: **Maximum Relative Differences in Pin-Cell Average Values in MOX Assemblies.**

	CMFE-0		CMFE-2	
Test	fast group	thermal group	fast group	thermal group
1	$5{\cdot}10^{-4}$	$1{\cdot}10^{-2}$	$7{\cdot}10^{-4}$	$5{\cdot}10^{-3}$
2	$1{\cdot}10^{-3}$	$2{\cdot}10^{-3}$	$8{\cdot}10^{-4}$	$5{\cdot}10^{-3}$
3	$2{\cdot}10^{-2}$	$3{\cdot}10^{-1}$	$8{\cdot}10^{-3}$	$6{\cdot}10^{-2}$
4	$9{\cdot}10^{-3}$	$1{\cdot}10^{-1}$	$5{\cdot}10^{-3}$	$3{\cdot}10^{-2}$
5	$6{\cdot}10^{-2}$	$4{\cdot}10^{-1}$	$3{\cdot}10^{-2}$	$1{\cdot}10^{-1}$

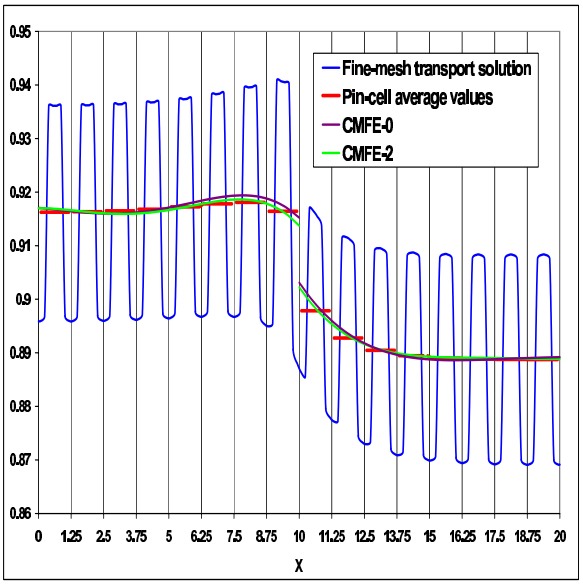

Figure 5.6: Test 1. The fast scalar flux versus position.

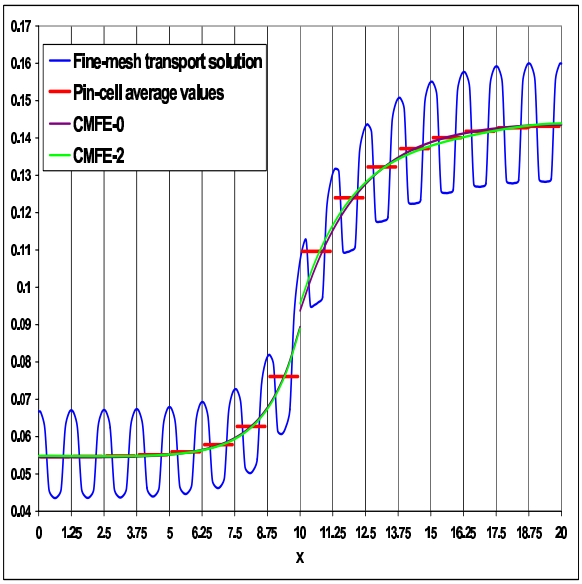

Figure 5.7: Test 1. The thermal scalar flux versus position.

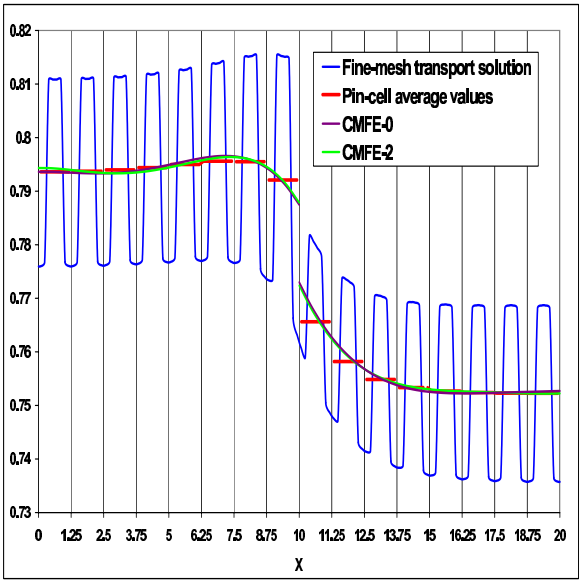

Figure 5.8: Test 2. The fast scalar flux versus position.

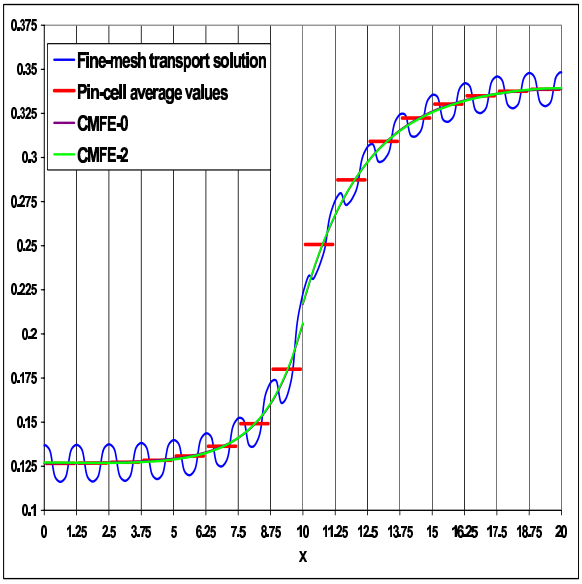

Figure 5.9: Test 2. The thermal scalar flux versus position.

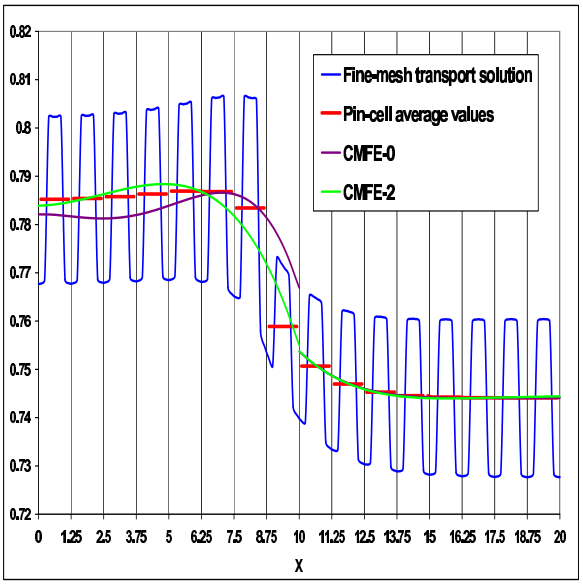

Figure 5.10: Test 3. The fast scalar flux versus position.

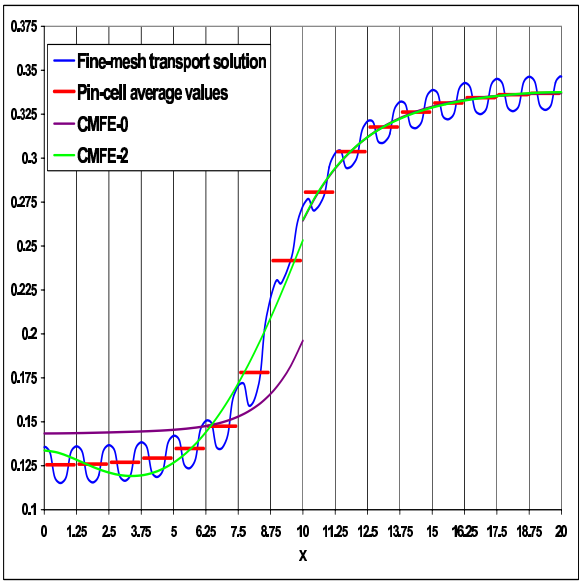

Figure 5.11: Test 3. The thermal scalar flux versus position.

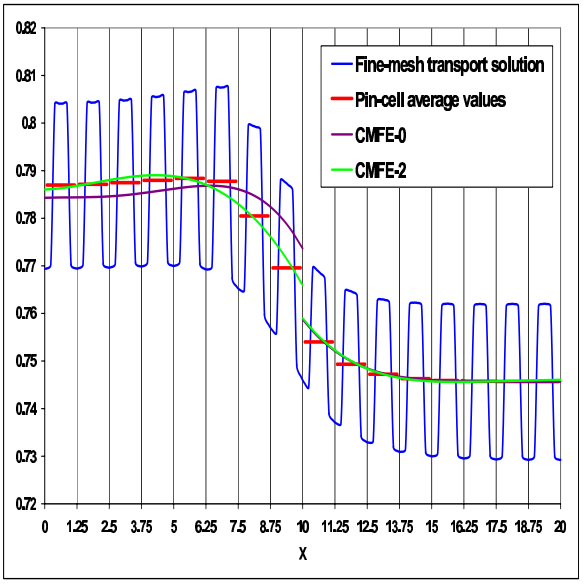

Figure 5.12: Test 4. The fast scalar flux versus position.

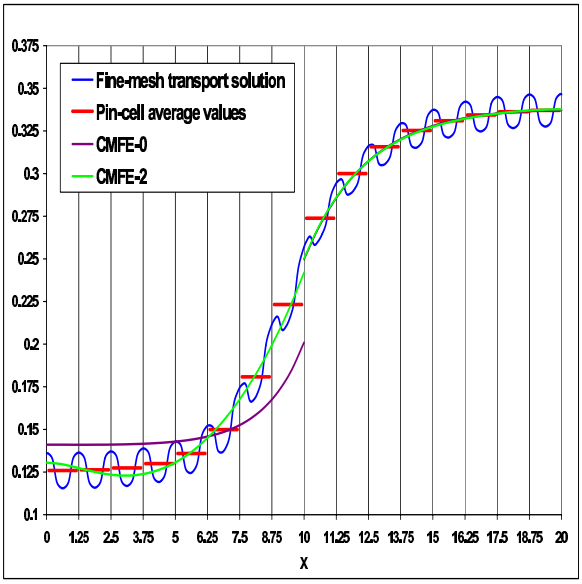

Figure 5.13: Test 4. The thermal scalar flux versus position.

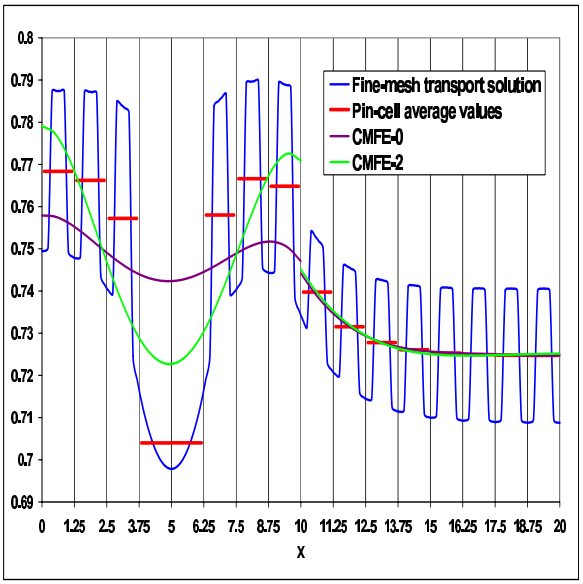

Figure 5.14: Test 5. The fast scalar flux versus position.

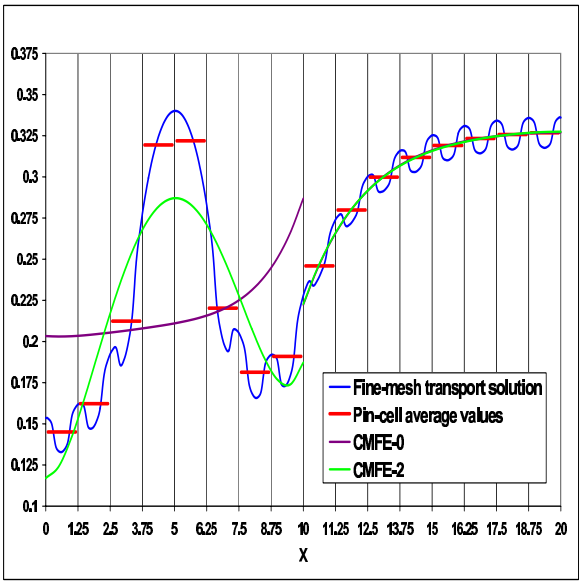

Figure 5.15: Test 5. The thermal scalar flux versus position.

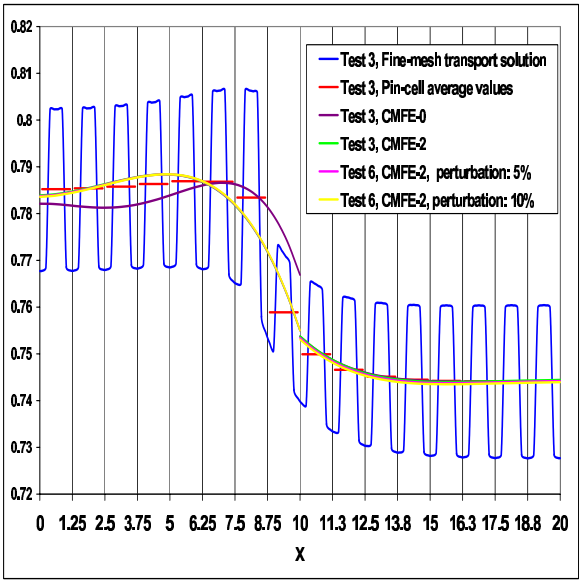

Figure 5.16: Test 6. The fast scalar flux versus position.

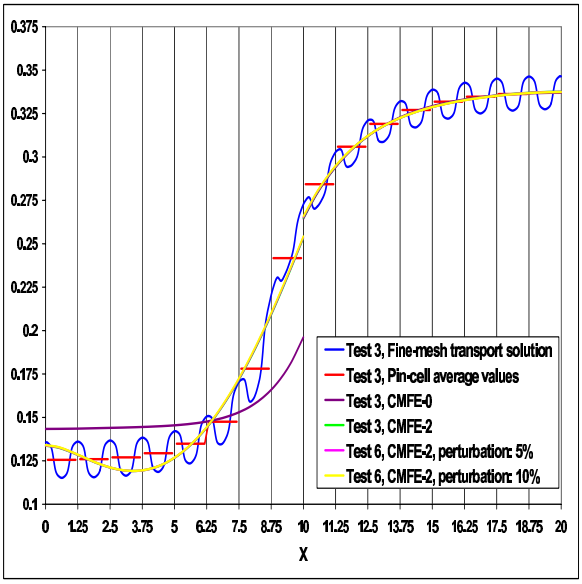

Figure 5.17: Test 6. The thermal scalar flux versus position .

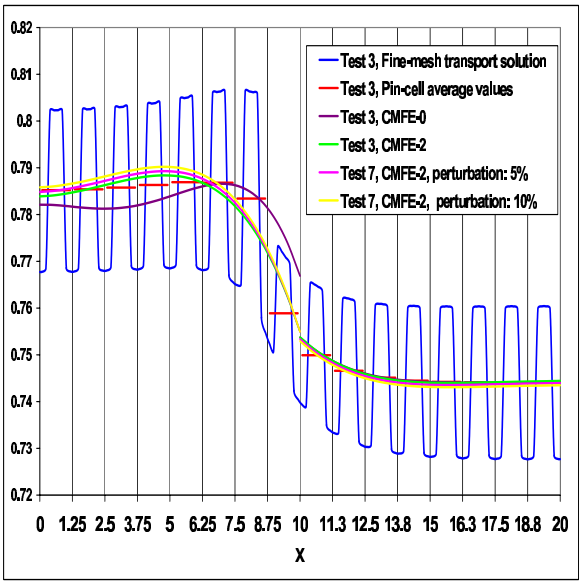

Figure 5.18: Test 7. The fast scalar flux versus position.

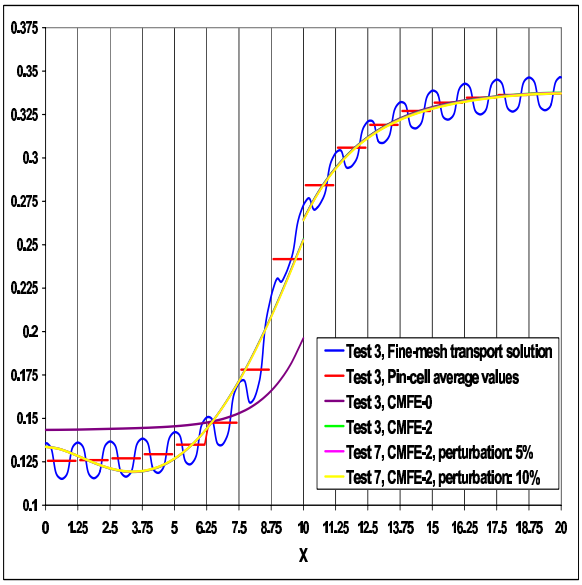

Figure 5.19: Test 7. The thermal scalar flux versus position.

Bibliography

[1] D.Y. Anistratov and M.L. Adams, "Consistent Coarse-Mesh Discretization of the Low-Order Equations of the Quasidiffusion Method," *Trans. Am. Nucl. Soc.,* **83**, 250-251 (2000).

[2] K. T. Clarno and M. L. Adams, "Improved Boundary Conditions for Assembly-Level Transport Codes," *Int. Conf. on the New Frontiers of Nuclear Technology: Reactor Physics, Safety and High-Performance Computing (PHYSOR 2002)*, Seoul, Korea, Oct. 7-10 (2002).

[3] R. Nes and T. S. Palmer, "An Advanced Nodal Discretization for the Quasi-Diffusion Low-Order Equations," *Int. Conf. on the New Frontiers of Nuclear Technology: Reactor Physics, Safety and High-Performance Computing (PHYSOR 2002)*, Seoul, Korea, Oct. 7-10 (2002).

[4] D. Y. Anistratov, "Homogenization Methodology for the Low-Order Equations of the Quasidiffusion Method," *Int. Conf. on the New Frontiers of Nuclear Technology: Reactor Physics, Safety and High-Performance Computing (PHYSOR 2002)*, Seoul, Korea, Oct. 7-10 (2002).

[5] H. Hikaru, D. Y. Anistratov, and M. L. Adams, "Splitting Method for Solving the Coarse-Mesh Discretized Low-Order Quasidiffusion Equations," *Proceedings of American Nuclear Society Topical Meeting in Mathematics & Computations, Nuclear Mathematical and Computational Sciences: A Century in Review - A Century Anew*, Gatlinburg, TN, April 6-10, 2003, 20 pp.(2003).

[6] K. T. Clarno and M. L. Adams, "Capturing the Effects of Unlike Neighbors in Single-Assembly Calculations," *Proceedings of American Nuclear Society Topical Meeting in Mathematics & Computations, Nuclear Mathematical and Computational Sciences: A Century in Review - A Century Anew*, Gatlinburg, TN, April 6-10, 2003, 20 pp.(2003).

[7] V.Ya. Gol'din, "A Quasidiffusion Method for Solving the Kinetic Equation," *USSR Comp. Math. and Math. Phys.* **4**, 136-149 (1964).

[8] N. N. Aksenov and V. Ya. Gol'din, "Computation of the Two-Dimensional Stationary Equation of Neutron Transfer by the Quasi-Diffusion Method," *USSR Comp. Math. and Math. Phys.*, **19**, No. 5, 263-266 (1979).

[9] V. Ya. Gol'din, "On Mathematical Modeling of Problems of Non-Equilibrium Transfer in Physical Systems," in *Modern Problems of Mathematical Physics and Computational Mathematics*, Nauka, Moscow, 113-127 (1982) (in Russian).

[10] K. S. Smith, "Assembly Homogenization Techniques for Light Water Reactor Analysis," *Progress in Nuclear Energy*, **17**, 303-335 (1986).

[11] D. Y. Anistratov and V. Ya. Gol'din, "Solving the Multigroup Transport Equation by the Quasidiffusion Method," *Preprint of the Keldysh Institute for Applied Mathematics*, the USSR Academy of Sciences, No. 128 (1986) (in Russian).

[12] E.N.Aristova, V.Ya. Gol'din, and A.V.Kolpakov, "Multidimensional Calculations of Radiation Transport by Nonlinear Quasi-Diffusion Method," *Proceeding of ANS International Conference on Mathematics and Computation, Reactor Physics and Environmental Analysis in Nuclear Applications*, Sept. 27-30, 1999, Madrid, Spain, 667-676 (1999).

[13] D.Y. Anistratov and V.Ya. Gol'din, "Nonlinear Methods for Solving Particle Transport Problems," *Transport Theory Statist. Phys.* **22** 42–77 (1993).

[14] K. S. Smith, *private communication.*

Chapter 6

Splitting Method for Solving the Coarse-Mesh Discretized Low-Order Quasidiffusion Equations

6.1 Abstract

In this chapter, the development is presented of a splitting method that can efficiently solve coarse-mesh discretized low-order quasidiffusion (LOQD) equations. The LOQD problem can reproduce exactly the transport scalar flux and current. To solve the LOQD equations efficiently, a splitting method is proposed. The presented method splits the LOQD problem into two parts: (i) the D-problem that captures a significant part of transport solution in the central parts of assemblies and can be reduced to a diffusion-type equation, and (ii) the Q-problem that accounts for the complicated behavior of the transport solution near assembly boundaries. Independent coarse-mesh discretizations are applied: the D-problem equations are approximated by means of a finite-element method, whereas the Q-problem equations are discretized using a finite-volume method. Numerical results demonstrate the efficiency of the presented methodology.

6.2 Introduction

The current generation of reactor physics methodology for full reactor-core calculations is based on the diffusion equation. To obtain highly accurate results using such methodology, it is necessary to address the limitations of diffusion theory. A series of significant improvements have been developed over the years by means of sophisticated methods of preparation of group cross section data, effective transport corrections at the interface of assemblies, etc [1]. An alternative approach is to create a general methodology that is based on equations that can take into account the transport effects exactly. The low-order equations of the quasidiffusion (QD) method meet this criterion [2, 3, 4]. In this paper we develop a methodology for reactor physics calculations based on the ideas of the QD method [5, 6, 7, 8].

The QD method is an efficient approach for solving particle transport problems. The

system of equations of this method consists of two parts: high-order and low-order equations. The high-order equation is the transport equation itself, and the system of the low-order equations is a set of equations for the scalar flux and current. The resulting system of equations is closed by means of linear-fractional functionals that are calculated from the solution of the high-order problem. These functionals become coefficients in the LOQD equations. They are weakly dependent on the transport solution. It is important to note that the LOQD equations generate the exact transport solution provided the functionals are exact.

The work reported here is a part of a homogenization methodology for full-core calculations that will be used in combination with assembly-level transport calculations that utilize albedo boundary conditions, without making color-set calculations, to simulate interactions with adjacent assemblies in a reactor core [6]. Note that if the albedo boundary conditions accurately represent the presence of a different neighboring assembly, then the single-assembly transport calculation accurately reproduces the correct fine-mesh solution, and all functionals calculated from the single-assembly solution will be accurate. To generate all necessary data for the coarse-mesh LOQD equations it is necessary to calculate few-group cross sections and functionals, using the fine-mesh fine-group transport solution obtained from assembly-level calculations.

The structure of the low-order quasidiffusion (LOQD) equations is similar to the structure of the P1 and diffusion equations, which partially explains the name of the method. However, the LOQD equations reproduce exactly the scalar flux and current of the transport solution provided that the functionals are exact, because no approximation is made to derive the QD equations. Another significant difference from the P1 equations (and hence the diffusion equation) is that instead of the gradient of the scalar flux the first moment equation contains the divergence of a product of a spatially dependent tensor and the scalar flux. A consequence is that the LOQD equations do not have a self-adjoint operator, unlike the diffusion equation. This feature of the LOQD equations requires special effective methods for discretizing them and solving the resulting non-symmetric system of discretized equations. A group of efficient methods have been developed that solve these issues for a certain class of problems and type of discretizations [9, 10, 11, 12]. However, in full-core reactor calculations, it is highly desirable to use methods that are very accurate on coarse meshes. Such discretizations of the LOQD equations give rise to a large system of algebraic equations with rather complicated structure. Thus, in this type of computational physics problem, it is necessary to develop an efficient new approach for solving the discretized equations.

A methodology that accounts for transport effects in reactor core calculations requires extra computational effort compared with solving the diffusion equation. It is highly desirable to minimize these extra costs. In this paper, we propose a splitting method that formulates two problems instead of one original LOQD problem. The first problem is a tensor diffusion equation, and hence existing advanced methods for diffusion problems can be used to solve it efficiently. The solution of the second problem is basically a transport correction to the first solution. We study ways to minimize costs for solving the second problem to optimize the solution of the overall LOQD problem.

Note that recently different research groups have begun developing methodologies for solving the transport equation for multidimensional full-core models on fine spatial grids and with fine energy groups. Here we develop a different kind of methodology accounting

for transport effects, which can be directly used in existing production reactor-physics codes for full-core calculations. Our goal is to obtain an excellent approximation of the fine-mesh fine-group transport solution for approximately the cost of coarse-mesh few-group diffusion.

The reminder of the paper is organized as follows. In Sec. 6.3 we formulate the few-group LOQD equations. In Sec. 6.4 we define our splitting method for solving the LOQD equations in differential form. In Sec. 6.5 we present the method for calculating discontinuity factors and formulate the interface conditions for the solution of the split problems. In Sec. 6.6 we present the discretization of equations of the splitting method. In Sec. 6.7 we demonstrate numerical solutions of test problems that simulate the interaction of MOX and uranium assemblies. We conclude with a discussion in Sec. 6.8.

6.3 The Few-Group Low-Order Quasidiffusion Equations

Let us consider a few group k-eigenvalue transport problem in 1D slab geometry. The LOQD equations for the group scalar flux ϕ^g and current J^g have the following form [4]:

$$\frac{d}{dx}J^g(x) + \Sigma_r^g(x)\phi^g(x) = \sum_{\substack{p=1\\p\neq g}}^{M_g} \Sigma_{s,0}^{p\to g}(x)\phi^p(x) + \frac{1}{k_{eff}}\chi^g(x)\sum_{p=1}^{M_g}\nu_f^p(x)\Sigma_f^p(x)\phi^p(x)\ , \tag{6.1}$$

$$\frac{d}{dx}\left(E^g(x)\phi^g(x)\right) + \Sigma_{tr}^g(x)J^g(x) = 0\ , \tag{6.2}$$

$$a \le x \le b\ , \quad g = 1, ..., M_g\ . \tag{6.3}$$

The boundary conditions are given by

$$J^g(a) = C_a^g\phi^g(a)\ , \quad J^g(b) = C_b^g\phi^g(b) \tag{6.4}$$

in case of vacuum boudaries and

$$J^g(a) = 0\ , \quad J^g(b) = 0 \tag{6.5}$$

in case of reflective boundaries. Note that for simplicity we consider problems with isotropic group-to-group scattering.

The functionals E^g, C_a^g, and C_b^g are calculated by means of the group angular flux $\psi^g(x,\mu)$ and defined as

$$E^g(x) = \int_{-1}^{1}\mu^2\psi^g(x,\mu)d\mu \Big/ \int_{-1}^{1}\psi^g(x,\mu)d\mu\ , \tag{6.6}$$

$$C_a^g = \int_{-1}^{0}\mu\psi^g(a,\mu)d\mu \Big/ \int_{-1}^{0}\psi^g(a,\mu)d\mu\ , \quad C_b^g = \int_{0}^{1}\mu\psi^g(b,\mu)d\mu \Big/ \int_{0}^{1}\psi^g(b,\mu)d\mu\ . \tag{6.7}$$

The complete system of equations of the QD method includes also the transport equation, and the resulting nonlinear problem is equivalent to the original linear transport problem.

The E^g, C_a^g, and C_b^g contain all information about the transport solution. Hence, if these functionals are known exactly, then the solution of the LOQD equations is the exact transport scalar flux and current, i.e. ϕ^g and J^g. The functional E^g is spatially dependent, and this feature of E^g makes the LOQD significantly different from P1 equations, especially in multidimensional geometries. The equations (6.1) and (6.2) can be reduced to a diffusion-like group equations for the group scalar flux

$$-\frac{d}{dx}\left(\frac{1}{\Sigma_{tr}^g(x)}\frac{d}{dx}\left(E^g(x)\phi^g(x)\right)\right)+\Sigma_r^g(x)\phi^g(x)=\sum_{\substack{p=1\\p\neq g}}^{M_g}\Sigma_{s,0}^{p\to g}(x)\phi^p(x)+\frac{1}{k_{eff}}\chi^g\sum_{p=1}^{M_g}\nu_f^p\Sigma_f^p(x)\phi^p(x)\ . \tag{6.8}$$

The important difference from the neutron diffusion equation is that the spatially dependent E^g is a factor of the scalar flux under the second derivative. In the multidimensional case, there also exist terms with mixed derivatives of elements of the QD (Eddington) tensor [2].

6.4 Splitting Method for Solving the LOQD Equations

In full-core calculations, the LOQD equations are to be solved on coarse grids each cell of which represents a part of an assembly [1]. In the new methodology the group data for each type of assembly will contain all necessary information about spatially averaged cross sections, discontinuity factors, etc., as well as quasidiffusion functionals (Eddington tensors) that are to be determined in assembly-level calculations using special albedo boundary conditions [6, 13]. Assuming that the cross sections and QD functionals are known, the iteration process for determining the k-eigenvalue and associated eigenfunction from the LOQD problem is defined as follows for a 1D problem:

$$\frac{d}{dx}J^{g[s]}+\Sigma_r^g\phi^{g[s]}=\sum_{\substack{p=1\\p\neq g}}^{M_g}\Sigma_{s,0}^{p\to g}\phi^{p[s]}+\frac{1}{k_{eff}^{[s-1]}}\chi^g\sum_{p=1}^{M_g}\nu_f^p\Sigma_f^p\phi^{p[s-1]}\ , \tag{6.9}$$

$$\frac{d}{dx}\left(E^g\phi^{g[s]}\right)+\Sigma_{tr}^g J^{g[s]}=0\ , \tag{6.10}$$

$$J^{g[s]}(a)=C_a^g\phi^{g[s]}(a)\ ,\quad J^{g[s]}(b)=C_b^g\phi^{g[s]}(b)\ , \tag{6.11}$$

$$k_{eff}^{[s]}=\frac{\sum_{p=1}^{M_g}\int_a^b\nu_f^p\Sigma_f^p\phi^{p[s]}dx}{\sum_{p=1}^{M_g}\left(J^{p[s]}(b)-J^{p[s]}(a)+\int_a^b\Sigma_a^p\phi^{p[s]}dx\right)}\ , \tag{6.12}$$

where s is the iteration index.

To develop an efficient method for solving the LOQD equations, we split this system of equations into two problems, taking advantage of the nature of the large-scale behavior of neutron transport in fuel assemblies. On each s-iteration we solve two problems. The first problem (D-problem) is defined as

$$\frac{d}{dx}J_D^{g[s]}+\Sigma_r^g\phi_D^{g[s]}=\sum_{\substack{p=1\\p\neq g}}^{M_g}\Sigma_{s,0}^{p\to g}\phi_D^{p[s]}+\frac{1}{k_{eff}^{[s-1]}}\chi^g\sum_{p=1}^{M_g}\nu_f^p\Sigma_f^p\phi^{p[s-1]}\ , \tag{6.13}$$

$$\widehat{E}^g \frac{d}{dx}\phi_D^{g[s]} + \Sigma_{tr}^g J_D^{g[s]} = 0 \ , \tag{6.14}$$

$$J_D^{g[s]}(a) = C_a^g \phi_D^{g[s]}(a) \ , \quad J_D^{g[s]}(b) = C_b^g \phi_D^{g[s]}(b) \ , \tag{6.15}$$

Here $\widehat{E}^g(x)$ is a piece-wise constant function on a set of coarse-mesh cells. The method for choosing the values of $\widehat{E}^g$ in each cell is discussed below.

The second problem (Q-problem) is given by

$$\frac{d}{dx} J_Q^{g[s]} + \Sigma_r^g \phi_Q^{g[s]} = \sum_{\substack{p=1 \\ p \neq g}}^{M_g} \Sigma_{s,0}^{p \to g} \phi_Q^{p[s]} \ , \tag{6.16}$$

$$\frac{d}{dx}\left(E^g \phi_Q^{g[s]}\right) + \Sigma_{tr}^g J_Q^{g[s]} = \frac{d}{dx}\left((\widehat{E}^g - E^g)\phi_D^{g[s]}\right) \ , \tag{6.17}$$

$$J_Q^{g[s]}(a) = C_a^g \phi_Q^{g[s]}(a) \ , \quad J_Q^{g[s]}(b) = C_b^g \phi_Q^{g[s]}(b) \ . \tag{6.18}$$

The group scalar flux and current are the sums of the corresponding solutions of the above two problems

$$\phi^{g[s]} = \phi_D^{g[s]} + \phi_Q^{g[s]} \ , \quad J^{g[s]} = J_D^{g[s]} + J_Q^{g[s]} \ . \tag{6.19}$$

The equations of the resulting D-problems are similar to P1 equations, and, thus, they can be reduced to a diffusion equation. The differential operator of the D-problem is self-adjoint. All these features of the D-problem enable one to use high-order approximations and efficient iterative methods that were previously developed for the diffusion equation. Note that if the cross sections in Eqs. (6.13)-(6.15) are constant in each cell, it is possible to obtain solutions in analytic form and use them in expansion of ϕ_D^g for the discretization of these equations [14]. This can significantly increase accuracy of the numerical solution of the overall problem. The Q-problem equations have properties that are similar to those of the original LOQD equations described above. The extension of this splitting method to multidimensional geometries is straightforward.

Figure 6.1 shows pin-cell average values of the functional E^g in the thermal group across a model assembly. The left boundary corresponds to the center of an assembly, whereas the right boundary is the interface with an unlike assembly. This figure demonstrates a typical shape of E^g within assemblies. Note that the large-scale behavior of the functional E^g is such that it is almost flat in the central part (interior) of an assembly and changes in vicinity of assembly boundaries, having a form of "bath-tub" function across the assembly. Hence, if we choose $\widehat{E}^g$ as an average value of $E^g(x)$ over the interior of the assembly (in this particular case over $0 \leq x \leq 5$), then the terms in the right-hand side of Eq. (6.17) will be small in the central part of assemblies. Thus, in our methodology we define $\widehat{E}^g$ in the following way

$$\widehat{E}^g = \frac{\int\limits_{interior} E^g(x)\phi^{g,fm}(x)dx}{\int\limits_{interior} \phi^{g,fm}(x)dx} \ , \tag{6.20}$$

where $\phi^{g,fm}$ is the fine-mesh scalar flux obtained from assembly-level transport calculations.

The solution ϕ_D of the D-problem (6.13)-(6.15) captures a significant part of the transport solution in the central parts of assemblies. The solution ϕ_Q of the Q-problem (6.16)-(6.18)

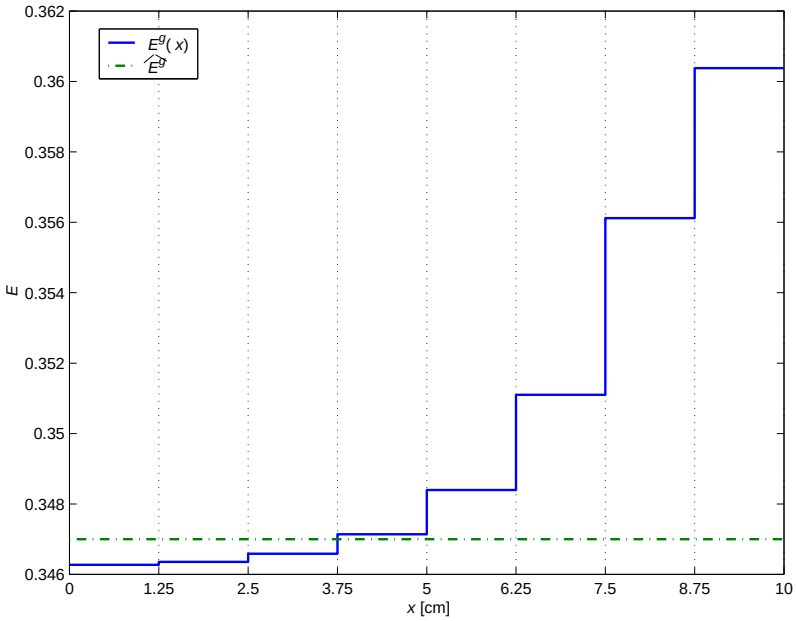

Figure 6.1: **Pin-cell average values of E^g in thermal group in a model assembly.**

accounts for the complicated behavior of the transport solution near interfaces between unlike assemblies. Note that if in the D-problem we neglect ϕ_Q, then in Eq. (6.13) $\phi = \phi_D$. Thus, the system of equations for ϕ_D is similar to P1 equations with a modified diffusion coefficient

$$D^g = \frac{\widehat{E}^g}{\Sigma^g_{tr}} \ . \tag{6.21}$$

Hereafter we refer to such problem for ϕ_D as modified diffusion.

6.5 Calculation of Discontinuity Factors and Interface Conditions for Global Calculations

6.5.1 Discontinuity Factors

The single-assembly calculations with albedo boundary conditions generate the fine-mesh fine-group transport solution, $\phi^{g,fm}$, $J^{g,fm}$, k^{fm}_{eff}, which is used to compute necessary assembly-averaged cross sections and functionals [6]. Another component of the group data is a set of discontinuity factors. To calculate them for the LOQD equations (6.1) and (6.2), one needs to solve these equations for an assembly with boundary conditions defined by the known fine-mesh currents, i.e.

$$J^g|_{x=x_\gamma} = J^{g,fm}|_{x=x_\gamma} \quad x_\gamma \in \partial\Gamma \ . \tag{6.22}$$

where $\partial\Gamma$ is the boundary of an assembly. In case of the splitting method, we need to formulate specific boundary conditions for both D- and Q-problems that will meet the following condition:

$$(J^g_D + J^g_Q)|_{x=x_\gamma} = J^{g,fm}|_{x=x_\gamma} \quad x_\gamma \in \partial\Gamma \ . \tag{6.23}$$

The choice of boundary conditions for each of two problems is not unique. We have chosen to impose the following boundary conditions:

$$J_D^g|_{x=x_\gamma} = J^{g,fm}|_{x=x_\gamma}, \quad J_Q^g|_{x=x_\gamma} = 0 \quad x_\gamma \in \partial\Gamma \ , \tag{6.24}$$

which is similar to the way the fission term was split between two problems. Note that there is no a priori information on the ratio between J_D^g and J_Q^g that could be used to split the known boundary current between the two.

Finally, to determine the discontinuity factors, we calculate auxiliary functions $\phi_D^{*,g}$ and $\phi_Q^{*,g}$ as the solution of the differential problem defined as:

$$\frac{d}{dx}J_D^{*,g} + \Sigma_r^g \phi_D^{*,g} = \sum_{\substack{p=1 \\ p\neq g}}^{M_g} \Sigma_{s,0}^{p\to g}\phi_D^{*,p} + \frac{1}{k_{eff}^{fm}}\chi^g \sum_{p=1}^{M_g} \nu_f^p \Sigma_f^p \phi^{p,fm} \ , \tag{6.25}$$

$$\widehat{E}^g \frac{d}{dx}\phi_D^{*,g} + \Sigma_{tr}^g J_D^{*,g} = 0 \ , \tag{6.26}$$

$$J_D^{*,g}|_{x=x_\gamma} = J^{g,fm}|_{x=x_\gamma} \ , \tag{6.27}$$

$$\frac{d}{dx}J_Q^{*,g} + \Sigma_r^g \phi_Q^{*,g} = \sum_{\substack{p=1 \\ p\neq g}}^{M_g} \Sigma_{s,0}^{p\to g}\phi_Q^{*,p} \ , \tag{6.28}$$

$$\frac{d}{dx}\left(E^g \phi_Q^{*,g}\right) + \Sigma_{tr}^g J_Q^{*,g} = \frac{d}{dx}\left((\widehat{E}^g - E^g)\phi_D^{*,g}\right) \ , \tag{6.29}$$

$$J_Q^{*,g}\big|_{x=x_\gamma} = 0 \ , \tag{6.30}$$

$$\phi^{*,g} = \phi_D^{*,g} + \phi_Q^{*,g} \ . \tag{6.31}$$

As a result, we obtain the auxiliary function $\phi^{*,g}$ that reproduces the fine-mesh eigenvalue, assembly-averaged scalar flux and current at boundaries of an assembly. The discontinuity factors G^g at assembly boundaries are defined as:

$$G^g = \left.\frac{\phi^{g,fm}}{\phi^{*,g}}\right|_{x=x_\gamma} \qquad x_\gamma \in \partial\Gamma \ . \tag{6.32}$$

Note that the final algorithm of calculation of the auxiliary function is defined for equations (6.25)-(6.31) in discretized form, and only zeroth moment of the fission source term is defined by means of the fine-mesh transport solution. Other algorithms can be formulated as well. They would generate auxiliary functions $\phi^{*,g}$ with different features.

6.5.2 Interface Conditions

In global calculations on a coarse mesh, it is necessary to impose interface conditions at each coarse-cell edge, $x = x_{edge}^{cell}$,

$$J^g|_{x=x_{edge}^{cell}-0} = J^g|_{x=x_{edge}^{cell}+0} \ , \tag{6.33}$$

$$[G^g\phi^g]|_{x=x_{edge}^{cell}-0} = [G^g\phi^g]|_{x=x_{edge}^{cell}+0} \tag{6.34}$$

that express current continuity and discontinuity of the coarse-mesh scalar flux at the interface between coarse cells. For the equations of splitting method, we specify interface conditions for D- and Q-components of the solution. Based on conditions (6.33) and (6.34), we define the interface conditions for D- and Q-problems as

$$J_D^g|_{x=x_{edge}^{cell}-0} = J_D^g|_{x=x_{edge}^{cell}+0}\ , \quad J_Q^g|_{x=x_{edge}^{cell}} = 0\ , \tag{6.35}$$

$$\left[G^g(\phi_D^g+\phi_Q^g)\right]\big|_{x=x_{edge}^{cell}-0} = \left[G^g(\phi_D^g+\phi_Q^g)\right]\big|_{x=x_{edge}^{cell}+0}\ . \tag{6.36}$$

Note that these interface conditions give rise to independent Q-problems in each coarse-cell, which are very inexpensive to solve.

6.6 Independent Coarse-Mesh Discretization of the LOQD Equations in Split Form

We use different methods to approximate equations of D- and Q-problems, i.e. independent discretization. The solution of the D-problem accounts for the major part of the transport solution, and we use high-order accuracy methods to discretize its equations. The structure of these equations gives us an opportunity to use sophisticated discretization methods developed for the diffusion equation. To solve the equations of the Q-problem, we apply a discretization method with second-order accuracy. Here we consider this approach in 1D case to study basic features of the proposed methodology.

6.6.1 Discretization of the D-Problem Equations

Let us define the coarse mesh $\{x_{j-1/2},\ j=1,...,N_j+1,\ x_{1/2}=a,\ x_{N_j+1/2}=b\}$. The D-problem equations (6.13)-(6.15) are discretized utilizing a high-order finite-element method based on the following expansion of the scalar flux $\Phi_{D,j}^g(x)$ in each jth coarse cell ($x_{j-1/2} \le x \le x_{j+1/2}$):

$$\Phi_{D,j}^g(x) = \sum_{l=0}^{2}(2l+1)\varphi_{D,j}^{(l),g}P_l(\zeta_j(x)) + \varphi_{D,j}^{(3),g}\sinh(\varkappa_{D,j}^g(x-x_j)) + \varphi_{D,j}^{(4),g}\cosh(\varkappa_{D,j}^g(x-x_j))\,, \tag{6.37}$$

where P_l are Legendre polynomials,

$$\zeta_j(x) = \frac{2(x-x_j)}{H_j}, \quad H_j = x_{j+1/2}-x_{j-1/2}, \quad x_j = 0.5(x_{j+1/2}+x_{j-1/2}), \quad 1 \le j \le N_j\,, \tag{6.38}$$

$$\varkappa_{D,j}^g = \sqrt{\frac{\langle\Sigma_r\rangle_j^g\langle\Sigma_{tr}\rangle_j^g}{\widehat{E}_j^g}}\,. \tag{6.39}$$

Hereafter we use brackets $\langle\bullet\rangle$ to denote the coarse-mesh averaged cross sections generated by means of fine-mesh scalar flux $\phi^{g,fm}$ obtained from assembly-level transport calculations.

To discretize the D-problem equations, we integrate the balance equation (6.13) over the jth coarse cell with Legendre polynomials as weight functions and approximate Eq. (6.14)

at coarse-cell edges using the information from pin-cells next to the boundaries of the given coarse cell [14]. Then, we formulate a set of discrete equations for Legendre moments of the coarse-cell scalar flux

$$\Phi_{D,j}^{(l),g} = \frac{1}{H_j} \int\limits_{x_{j-1/2}}^{x_{j+1/2}} P_l(\zeta_j(x)) \Phi_{D,j}^g(x) dx \,, \quad l = 0, 1, 2 \,, \tag{6.40}$$

cell-edge scalar fluxes, $\Phi_{D,j}^g(x_{j\pm1/2})$, and currents, $J_{D,j+1/2}^g \stackrel{\text{def}}{=} J_D^g(x_{j+1/2})$. The discretization scheme for the D-problem equations is defined as

$$J_{D,j+1/2}^g - J_{D,j-1/2}^g + \langle \Sigma_r \rangle_j^g H_j \Phi_{D,j}^{(0),g} = H_j \sum_{\substack{p=1 \\ p \neq g}}^{M_g} \langle \Sigma_{s,0} \rangle_j^{p \to g} \Phi_{D,j}^{(0),p} + \frac{1}{k_{eff}} H_j \sum_{p=1}^{M_g} \langle \chi \nu \Sigma_f \rangle_j^{p,g} \Phi_j^{(0),p} \,, \tag{6.41}$$

$$J_{D,j+1/2}^g + J_{D,j-1/2}^g + \frac{2\widehat{E}_j^g}{\langle \Sigma_{tr} \rangle_j^g H_j} \left(\Phi_{D,j}^g(x_{j+1/2}) - \Phi_{D,j}^g(x_{j-1/2}) \right) + \langle \Sigma_r \rangle_j^g H_j \Phi_{D,j}^{(1),g} = \tag{6.42}$$

$$H_j \sum_{\substack{p=1 \\ p \neq g}}^{M_g} \langle \Sigma_{s,0} \rangle_j^{p \to g} \Phi_{D,j}^{(1),p} + \frac{1}{k_{eff}} H_j \sum_{p=1}^{M_g} \langle \chi \nu \Sigma_f \rangle_j^{p,g} \Phi_j^{(1),p} \,,$$

$$J_{D,j+1/2}^g - J_{D,j-1/2}^g + \frac{6\widehat{E}_j^g}{\langle \Sigma_{tr} \rangle_j^g H_j} \left(\Phi_{D,j}^g(x_{j+1/2}) + \Phi_{D,j}^g(x_{j-1/2}) - 2\Phi_{D,j}^{(0),g} \right) + \langle \Sigma_r \rangle_j^g H_j \Phi_{D,j}^{(2),g} = \tag{6.43}$$

$$H_j \sum_{\substack{p=1 \\ p \neq g}}^{M_g} \langle \Sigma_{s,0} \rangle_j^{p \to g} \Phi_{D,j}^{(2),p} + \frac{1}{k_{eff}} H_j \sum_{p=1}^{M_g} \langle \chi \nu \Sigma_f \rangle_j^{p,g} \Phi_j^{(2),p} \,,$$

$$\widehat{E}_j^g \left. \frac{d\Phi_{D,j}^g}{dx} \right|_{x=x_{j-1/2}} + \{\Sigma_{tr}\}_j^{g,-} J_{D,j-1/2}^g = 0 \,, \tag{6.44}$$

$$\widehat{E}_j^g \left. \frac{d\Phi_{D,j}^g}{dx} \right|_{x=x_{j+1/2}} + \{\Sigma_{tr}\}_j^{g,+} J_{D,j+1/2}^g = 0 \,, \tag{6.45}$$

$$j = 1, ..., N_j \,,$$

$$G_j^{g,+} \left(\Phi_{D,j}^g(x_{j+1/2}) + \Phi_{Q,j}^g(x_{j+1/2}) \right) = G_{j+1}^{g,-} \left(\Phi_{D,j+1}^g(x_{j+1/2}) + \Phi_{Q,j+1}^g(x_{j+1/2}) \right) \,, \tag{6.46}$$

$$j = 1, ..., N_j - 1 \,,$$

$$J_{D,1/2}^g = C_a^g G_1^{g,-} \left(\Phi_{D,1}^g(x_{1/2}) + \Phi_{Q,1}^g(x_{1/2}) \right) \,, \tag{6.47}$$

$$J_{D,N_j+1/2}^g = C_b^g G_{N_j}^{g,+} \left(\Phi_{D,N_j}^g(x_{N_j+1/2}) + \Phi_{Q,N_j}^g(x_{N_j+1/2}) \right) \,, \tag{6.48}$$

where

$$\Phi_j^{(l),g} \stackrel{\text{def}}{=} \frac{1}{H_j} \int\limits_{x_{j-1/2}}^{x_{j+1/2}} P_l(\zeta_j(x)) \phi^g(x) dx \,. \tag{6.49}$$

Here $G_j^{g,\pm}$ are the right and left discontinuity factors, respectively, $\{\Sigma_{tr}\}_j^{g,\pm}$ are cross sections averaged over boundary pin-cell next to the right and left edges of jth coarse cell, correspondingly. Substituting the expansion (6.37) into Eqs. (6.41)-(6.48), we get the equations for the expansion coefficients $\varphi_{D,j}^{(l),g}$ (l=0,...,4) and cell-edge currents $J_{D,j-1/2}^g$.

6.6.2 Discretization of the Q-Problem Equations

Assume that a coarse-mesh cell represents half of an assembly. Such meshes are in common practice. To discretize the Q-problem equations, we divide each jth coarse cell into two subcells that are defined by $\tilde{x}_{j,i}$, i=1,2,3, where $\tilde{x}_{j,1} = x_{j-1/2}$ and $\tilde{x}_{j,3} = x_{j+1/2}$. The width of subcells is determined by the large-scale behavior of the functional E^g within a given coarse-mesh cell. A second-order finite-volume method described in previous publications [15] is used to approximate the equations (6.16)-(6.18). Note that if a coarse-mesh cell corresponds to a whole assembly, then four subcells are needed.

If we integrate Eq. (6.16) over each subcell and Eq. (6.17) over half-subcells, then make simple approximations [15], we obtain a system of discrete equations for subcell-edge currents $J_{Q,j,i}^g \stackrel{\text{def}}{=} J_Q^g(\tilde{x}_{j,i})$, coarse-cell edge scalar fluxes $\Phi_{Q,j}^{g,\pm} \stackrel{\text{def}}{=} \phi_Q^g(x_{j\pm1/2})$, and subcell-average scalar fluxes

$$\bar{\Phi}_{Q,j,i}^g \stackrel{\text{def}}{=} \frac{1}{h_{j,i}} \int_{\tilde{x}_{j,i}}^{\tilde{x}_{j,i+1}} \phi_Q^g(x)dx \,, \tag{6.50}$$

where $h_{j,i} = \tilde{x}_{j,i+1} - \tilde{x}_{j,i}$. The equations are:

$$J_{Q,j,i+1}^g - J_{Q,j,i}^g + \langle\Sigma_r\rangle_j^g h_{j,i} \bar{\Phi}_{Q,j,i}^g = h_{j,i} \sum_{\substack{p=1 \\ p\neq g}}^{M_g} \langle\Sigma_{s,0}\rangle_j^{p\to g} \bar{\Phi}_{Q,j,i}^p \,, \quad i = 1,2 \,, \tag{6.51}$$

$$\bar{E}_{j,1}^g \bar{\Phi}_{Q,j,1}^g - \{E\}_j^{g,-} \Phi_{Q,j}^{g,-} + \frac{1}{2}\langle\Sigma_{tr}\rangle_j^g h_{j,1} J_{Q,j,1}^g = \left(\widehat{E}_j^g - \bar{E}_{j,1}^g\right) \bar{\Phi}_{D,j,1}^g - \left(\widehat{E}_j^g - \{E\}_j^{g,-}\right) \Phi_{D,j}^g(x_{j-1/2}) \,, \tag{6.52}$$

$$\bar{E}_{j,2}^g \bar{\Phi}_{Q,j,2}^g - \bar{E}_{j,1}^g \bar{\Phi}_{Q,j,1}^g + \frac{1}{2}\langle\Sigma_{tr}\rangle_j^g H_j J_{Q,j,2}^g = \left(\widehat{E}_j^g - \bar{E}_{j,2}^g\right) \bar{\Phi}_{D,j,2}^g - \left(\widehat{E}_j^g - \bar{E}_{j,1}^g\right) \bar{\Phi}_{D,j,1}^g \,, \tag{6.53}$$

$$\{E\}_j^{g,+} \Phi_{Q,j}^{g,+} - \bar{E}_{j,2}^g \bar{\Phi}_{Q,j,2}^g + \frac{1}{2}\langle\Sigma_{tr}\rangle_j^g h_{j,2} J_{Q,j,3}^g = \left(\widehat{E}_j^g - \{E\}_j^{g,+}\right) \Phi_{D,j}^g(x_{j+1/2}) - \left(\widehat{E}_j^g - \bar{E}_{j,2}^g\right) \bar{\Phi}_{D,j,2}^g \,, \tag{6.54}$$

$$j = 1, ..., N_j \,,$$

$$J_{Q,j,3}^g = 0 \,, \tag{6.55}$$

$$J_{Q,j+1,1}^g = J_{Q,j,3}^g \,, \tag{6.56}$$

$$j = 1, ..., N_j - 1 \,,$$

$$J_{Q,1,1}^g = 0 \,, \quad J_{Q,N_j,3}^g = 0 \,, \tag{6.57}$$

where

$$\bar{\Phi}_{D,j,i}^g \stackrel{\text{def}}{=} \frac{1}{h_{j,i}} \int_{\tilde{x}_{j,i}}^{\tilde{x}_{j,i+1}} \phi_D^g(x)dx \tag{6.58}$$

and $\bar{E}^g_{j,i}$ is the value of functional E^g averaged by means of the fine-mesh scalar flux over the given subcell region. $\{E\}^{g,\pm}_j$ are values of the QD functional averaged over the boundary pin-cell next to the right and left edges of jth coarse cell, respectively. The quantities $\bar{\Phi}^g_{D,j,i}$ defined by Eq. (6.58) are calculated from the solution of the D-problem, i.e. in the following way:

$$\bar{\Phi}^g_{D,j,i} = \frac{1}{h_{j,i}} \int_{\tilde{x}_{j,i}}^{\tilde{x}_{j,i+1}} \Phi^g_{D,j}(x)dx \tag{6.59}$$

In order to solve the coupled systems of D- and Q- problems, we need to calculate the Legendre spatial moments of ϕ^g_Q

$$\Phi^{(l),g}_{Q,j} \stackrel{\text{def}}{=} \frac{1}{H_j} \int_{x_{j-1/2}}^{x_{j+1/2}} P_l(\zeta_j(x))\phi^g_Q(x)dx\,, \quad l = 0, 1, 2\,, \tag{6.60}$$

using the solution of the above discrete equations (6.51)-(6.57). The zeroth moment is computed as

$$\Phi^{(0),g}_{Q,j} = \frac{1}{H_j} \sum_{i=1}^{2} \bar{\Phi}^g_{Q,j,i} h_{i,j}\,. \tag{6.61}$$

The other two spatial moments are calculated, using approximation of ϕ^g_Q in jth coarse cell by means of a third-order polynomial interpolation function that fits coarse-cell edge values $\Phi^{g,\pm}_{Q,j}$ and two subcell-average values $\bar{\Phi}^g_{Q,j,i}$. As a result for $\Phi^{(l),g}_j$ (Eq. (6.49)) we get

$$\Phi^{(l),g}_j = \Phi^{(l),g}_{D,j} + \Phi^{(l),g}_{Q,j} \quad l = 0, 1, 2\,. \tag{6.62}$$

The position of interface between subcells (i.e. $\tilde{x}_{j,2}$) is chosen such that one subcell covers the region where E^g is almost flat and another subcell corresponds to the area where E^g changes significantly near the interface with neighboring assembly. For example, in the case that is shown in Figure 6.1, it is reasonable to use $\tilde{x}_{j,2} = 5$.

6.7 Numerical Results

In this section, we present the numerical results to demonstrate the performance of the proposed splitting method. We consider two test problems (Test A and B) for 1D slab geometry with two energy groups. They consist of MOX and uranium half-assemblies next to each other with reflective boundary conditions [16, 8]. The half-assembly width is 10 cm. The MOX assembly is located on the left of UO_2 assembly. Each half-assembly contains 8 fuel pin cells of the same type. The design of a fuel pin is shown in Figure 6.2. The cross sections for each test problem are listed in Tables 6.1 and 6.2. The fine-mesh solutions are calculated by the QD method using the second order finite-volume scheme for the LOQD equations and step characteristic method for the transport equation [15]. The fine mesh is uniform and consists of 128 equal cells (8 per pin cell). The angular mesh has 10 intervals. The multiplication factors in Tests A and B equal 1.5. The coarse mesh consists of one cell per half-assembly, i.e. $N_j = 2$. We recall that to solve the Q-problem, we define two

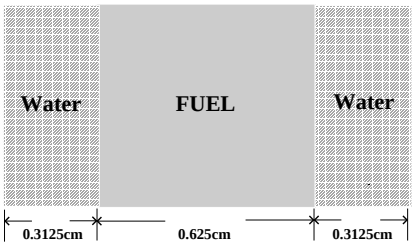

Figure 6.2: Pin-cell design.

subcells per coarse cell. Table 6.3 presents the values of $\widehat{E}^g$ used in these test problems. These values are generated by averaging fine-mesh E^g with fine-mesh scalar flux over the subcells adjacent to reflective boundaries. These subcells represent the interior assembly regions, where the functional E^g varies weakly. In our calculations, the subcells adjacent to the interface between assemblies are 3 pin cells wide, and the subcells next to reflective boundaries are 5 pin cells wide.

Table 6.1: Cross Sections for Test A.

Cross Sections	Σ_t^1	$\Sigma_{s,0}^{1\to1}$	$\Sigma_{s,0}^{1\to2}$	Σ_f^1	ν_f^1	Σ_t^2	$\Sigma_{s,0}^{2\to2}$	$\Sigma_{s,0}^{2\to1}$	Σ_f^2	ν_f^2
MOX fuel	0.2	0.2	0	0	0	0.6	0	0	0.6	1.5
Uranium fuel	0.2	0.2	0	0	0	0.2	0	0	0.2	1.5
Water	0.2	0.17	0.03	0	0	1.1	1.1	0	0	0

Table 6.2: Cross Sections for Test B.

Cross Sections	Σ_t^1	$\Sigma_{s,0}^{1\to1}$	$\Sigma_{s,0}^{1\to2}$	Σ_f^1	ν_f^1	Σ_t^2	$\Sigma_{s,0}^{2\to2}$	$\Sigma_{s,0}^{2\to1}$	Σ_f^2	ν_f^2
MOX fuel	0.2	0.185	0.015	0	0	1.2	0.9	0	0.3	1.5
Uranium fuel	0.2	0.185	0.015	0	0	1.0	0.9	0	0.1	1.5
Water	0.2	0.17	0.03	0	0	1.1	1.1	0	0	0

Table 6.3: $\widehat{E}^g$ for Test A and B.

g	Region	Test A	Test B
1	MOX	0.3330	0.3327
1	UO_2	0.3340	0.3345
2	MOX	0.3470	0.3332
2	UO_2	0.3522	0.3331

To evaluate the accuracy of the splitting method with independent discretization of equations, we use the numerical results obtained by means of a high-order finite-element (HOFE) method developed for solving LOQD equations [14]. We also apply the proposed splitting method (Eqs. (6.13)-(6.19)) to the discrete equations of the HOFE method and derived corresponding discretization of equations for D- and Q- problems, where the equations of both problems are approximated by the HOFE method. Note that this can be considered as consistent way of discretizing the equations of the splitting method. This enables us to analyze the accuracy of each part of solution, ϕ_D and ϕ_Q, by the proposed independent

discretization.

Figures 6.3, 6.4, 6.9, and 6.10 show the group scalar fluxes for Tests A and B obtained by the proposed splitting method with independent discretization and the results of the HOFE method for the LOQD equations. The x-axis gridlines correspond to pin-cell boundaries. These figures also demonstrate the solution of the diffusion equation ($E^g(x) = \frac{1}{3}$) calculated by means of the HOFE method. We note that in fast group the diffusion solution has significantly different spatial shape and, thus, its behavior is qualitatively different compared with the coarse-mesh transport solution that is represented by solution of the LOQD equations. The quantitative difference between transport and diffusion solutions in thermal group is not seen because of the scale. We explicitly demonstrate the relative difference between the transport and diffusion solutions on Figures 6.5, 6.6, 6.11, and 6.12. These graphs show that the largest relative errors in diffusion solution are the following: (a) $4{\cdot}10^{-3}$ in fast group and $2{\cdot}10^{-2}$ in thermal group for Test A, (b) $7{\cdot}10^{-3}$ in both fast and thermal groups for Test B.

The scalar fluxes of the proposed splitting method have very good agreement with those of the HOFE method. In both test problems, the maximum relative differences between the scalar fluxes obtained by the splitting and the HOFE methods are (i) Test A: $6{\cdot}10^{-4}$ in fast group and $8{\cdot}10^{-3}$ in thermal group, (ii) Test B: $8{\cdot}10^{-4}$ in fast group and $4{\cdot}10^{-3}$ in thermal group. Figures 6.7, 6.8, 6.13, and 6.14 demonstrate the relative difference between the scalar fluxes obtained by the splitting method and the HOFE method.

Figures 6.15-6.18 present the solutions of the D- and Q-problems for Test A obtained by the splitting and HOFE methods. Figures 6.19-6.22 demonstrate the same set of results for Test B. The figure for ϕ_D also show the solution of the modified diffusion. Smooth curves that represent the solution of the Q-problem calculated by the finite-volume method were obtained by means of a third-order polynomial interpolation function that fits coarse-cell edge values $\Phi^{g,\pm}_{Q,j}$ and two subcell-average values $\bar{\Phi}^g_{Q,j,i}$, i.e. the same polynomial function that is used to calculate necessary spatial moments of ϕ_Q for the fission source term in the D-problem.

These results show that the splitting method generates accurate solution for the D-problem. For the Q-problem, we used the second-order accurate finite-volume method and hence it is expected that there will be the difference compared to the results obtained by the HOFE method. In the fast group, the subcell average values and shapes of the Q-problem solutions generated by these two methods are fairly close to each other. The difference increases in the thermal group. The overall effect on the resulting scalar flux is small, and the splitting method with the considered discretization produces sufficiently accurate scalar fluxes. We note that the splitting method uses the third-order polynomial to reconstruct the Q-problem solution, whereas the HOFE utilizes more accurate approximation based on the second-order polynomial combined with hyperbolic sine and cosine.

The relative difference in pin-cell average values compared to the fine-mesh results are listed in Tables 6.4 and 6.5, where we present the results of the proposed splitting method. Pins are numbered from left to right in each assembly. In Test A, the maximum absolute values of relative differences in fast group are $1{\cdot}10^{-3}$ and $6{\cdot}10^{-4}$ for MOX and UO_2 assemblies, respectively, and in thermal group are $9{\cdot}10^{-3}$ in MOX and $1{\cdot}10^{-2}$ in UO_2. In Test B, the maximum absolute values of relative differences in fast group are $2{\cdot}10^{-3}$ in MOX and $5{\cdot}10^{-4}$ in UO_2, and in thermal group $4{\cdot}10^{-3}$ and $7{\cdot}10^{-4}$, correspondingly. These results show that the splitting method reproduces the pin-cell average values of the scalar flux with high

accuracy. Note that pin-power reconstruction using a form function will almost certainly produce even greater accuracy.

For the iteration process we used relative point-wise convergence criteria with values of 10^{-7} for the scalar flux and 10^{-8} for the eigenvalue. It took 15 and 16 iterations in case of the splitting method to calculate the solution of Test A and B, respectively. In case of the HOFE method the number of iterations are 13 and 17, correspondingly. Thus, the convergence behavior of the splitting method in these test problems is similar to that of the method without splitting.

Table 6.4: Test A. Relative difference in pin-cell average values for the splitting method

g	Region	pin #1	pin #2	pin #3	pin #4	pin # 5	pin # 6	pin #7	pin #8
1	MOX	$6{\cdot}10^{-4}$	$1{\cdot}10^{-3}$	$9{\cdot}10^{-4}$	$2{\cdot}10^{-4}$	$-7{\cdot}10^{-4}$	$-1{\cdot}10^{-3}$	$-1{\cdot}10^{-3}$	$3{\cdot}10^{-4}$
1	UO_2	$6{\cdot}10^{-4}$	$2{\cdot}10^{-4}$	$3{\cdot}10^{-4}$	$2{\cdot}10^{-4}$	$-9{\cdot}10^{-5}$	$-4{\cdot}10^{-4}$	$-5{\cdot}10^{-4}$	$-3{\cdot}10^{-4}$
2	MOX	$6{\cdot}10^{-3}$	$9{\cdot}10^{-3}$	$6{\cdot}10^{-3}$	$7{\cdot}10^{-4}$	$-4{\cdot}10^{-3}$	$-5{\cdot}10^{-3}$	$-5{\cdot}10^{-3}$	$-5{\cdot}10^{-3}$
2	UO_2	$1{\cdot}10^{-2}$	$4{\cdot}10^{-3}$	$-1{\cdot}10^{-3}$	$-3{\cdot}10^{-3}$	$-3{\cdot}10^{-3}$	$-3{\cdot}10^{-3}$	$-2{\cdot}10^{-3}$	$-1{\cdot}10^{-3}$

Table 6.5: Test B. Relative difference in pin-cell average values for the splitting method

g	Region	pin #1	pin #2	pin #3	pin #4	pin # 5	pin # 6	pin #7	pin #8
1	MOX	$7{\cdot}10^{-4}$	$1{\cdot}10^{-3}$	$1{\cdot}10^{-3}$	$2{\cdot}10^{-4}$	$-1{\cdot}10^{-3}$	$-2{\cdot}10^{-3}$	$-1{\cdot}10^{-3}$	$5{\cdot}10^{-4}$
1	UO_2	$5{\cdot}10^{-4}$	$-1{\cdot}10^{-4}$	$3{\cdot}10^{-4}$	$4{\cdot}10^{-4}$	$7{\cdot}10^{-5}$	$-3{\cdot}10^{-4}$	$-5{\cdot}10^{-4}$	$-3{\cdot}10^{-4}$
2	MOX	$1{\cdot}10^{-3}$	$3{\cdot}10^{-3}$	$1{\cdot}10^{-3}$	$-2{\cdot}10^{-3}$	$-4{\cdot}10^{-3}$	$-4{\cdot}10^{-3}$	$-2{\cdot}10^{-3}$	$4{\cdot}10^{-3}$
2	UO_2	$7{\cdot}10^{-4}$	$6{\cdot}10^{-4}$	$-5{\cdot}10^{-4}$	$-7{\cdot}10^{-4}$	$-5{\cdot}10^{-4}$	$-2{\cdot}10^{-4}$	$1{\cdot}10^{-4}$	$6{\cdot}10^{-4}$

6.8 Discussion

In this paper, we have developed a splitting method to solve the coarse-mesh discretized LOQD equations. The method effectively splits a problem into two parts. The D-problem captures a significant portion of the transport solution in the central part of assembly, and the Q-problem accounts for the complicated behavior of the transport solution in the vicinity of assembly boundaries. The calculation of discontinuity factors for the splitting method has been introduced, and corresponding interfacial conditions have been formulated for this particular method. Each part of the LOQD equations in the split form has been approximated by a different discretization scheme. The D-problem equations were approximated by means of the high-order finite element method. The Q-problem equations were discretized by using a finite volume method with second-order accuracy. Numerical results showed high accuracy of the proposed splitting method with the considered independent discretization of the equations of D- and Q- problems.

The successful performance of the splitting method in 1D geometry stimulates the efforts in extension of this method to multidimensional geometries. In 2D and 3D cases the solution of the LOQD equations discretized with high-order methods is rather computationally intensive problem. According to the proposed approach, one can split the LOQD problem into a D-problem that can be solved with current efficient methodologies for diffusion-type of equations and a Q-problem that can be discretized with a second-order finite-volume method because the solution of this problem is a small correction to solution of D-problem. Special

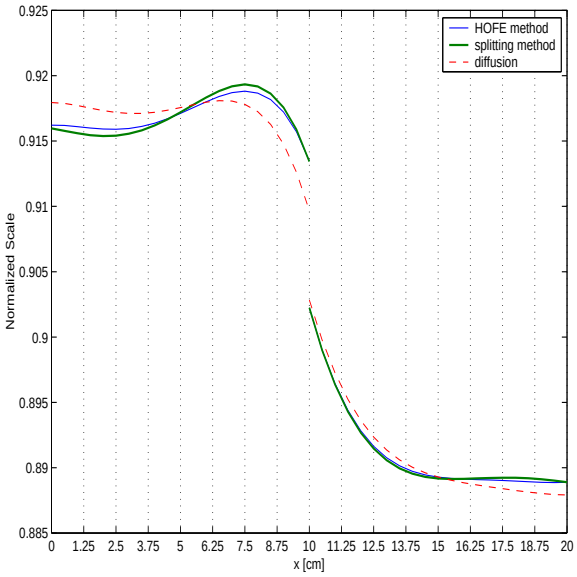

Figure 6.3: Test A. Fast scalar flux, $\phi^1(x)$.

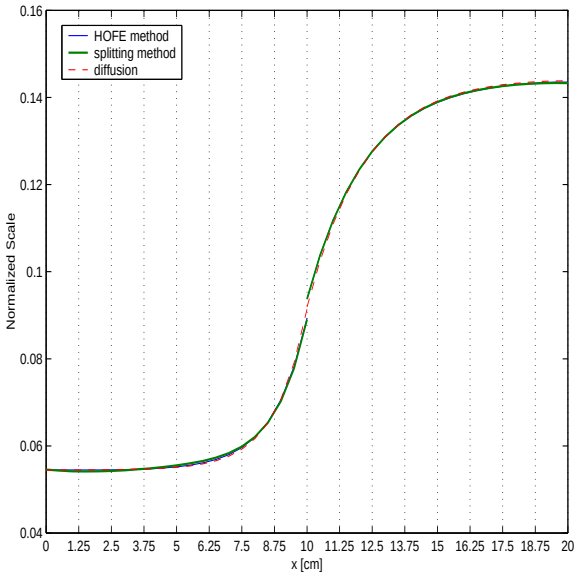

Figure 6.4: Test A. Thermal scalar flux, $\phi^2(x)$.

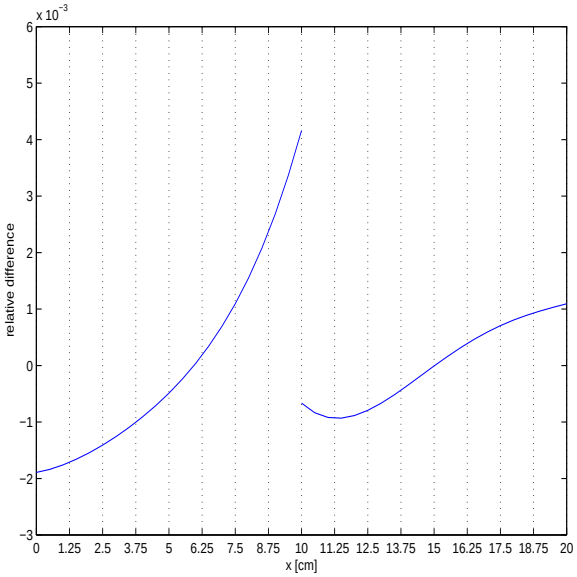

Figure 6.5: Test A. Relative difference in the fast scalar flux calculated by the diffusion equation compared to the coarse-mesh transport solution obtained from the LOQD equations.

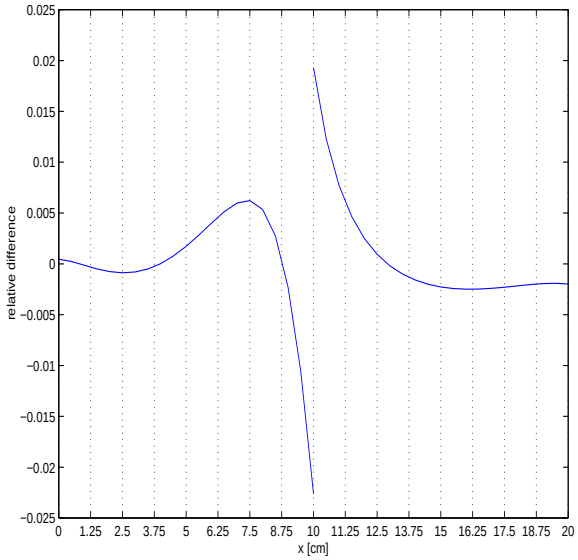

Figure 6.6: Test A. Relative difference in the thermal scalar flux calculated by the diffusion equation compared to the coarse-mesh transport solution obtained from the LOQD equations.

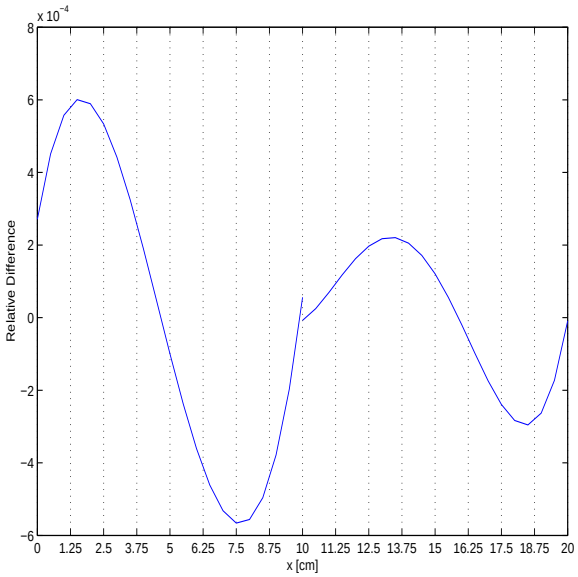

Figure 6.7: Test A. Relative difference in the fast scalar flux calculated by the splitting method compared to the results of the HOFE method.

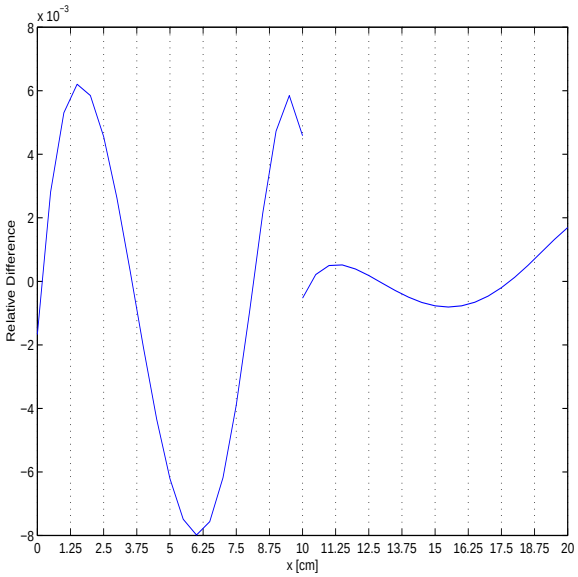

Figure 6.8: Test A. Relative difference in the thermal scalar flux calculated by the splitting method compared to the results of the HOFE method.

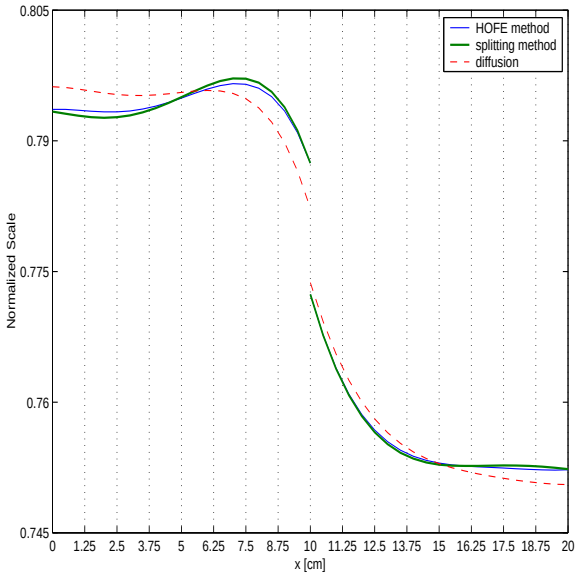

Figure 6.9: Test B. Fast scalar flux, $\phi^1(x)$.

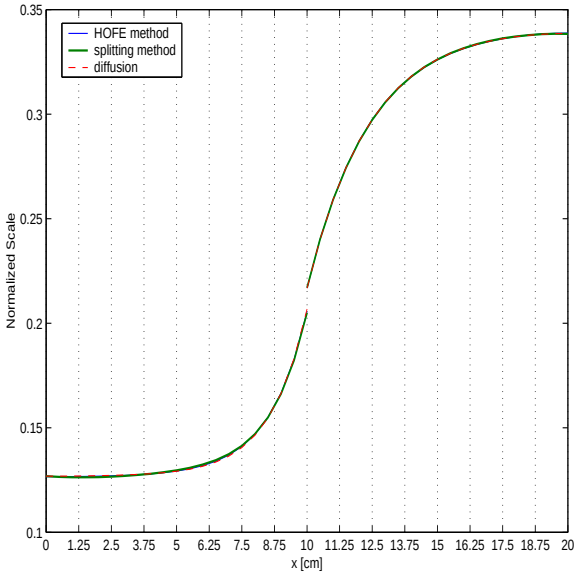

Figure 6.10: Test B. Thermal scalar flux, $\phi^2(x)$.

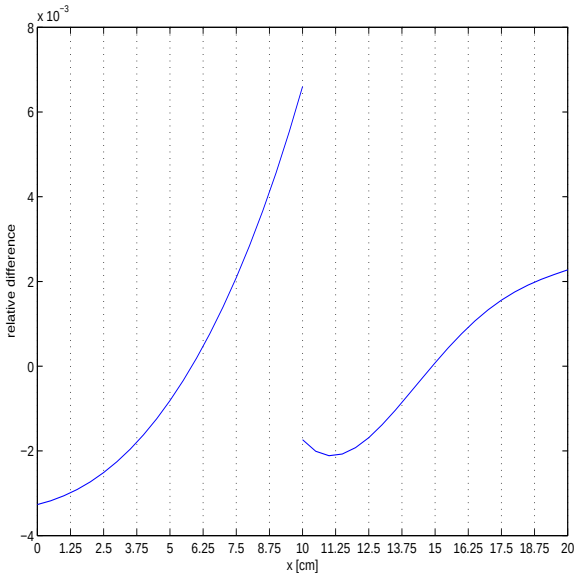

Figure 6.11: Test B. Relative difference in the fast scalar flux calculated by the diffusion equation compared to the coarse-mesh transport solution obtained from the LOQD equations.

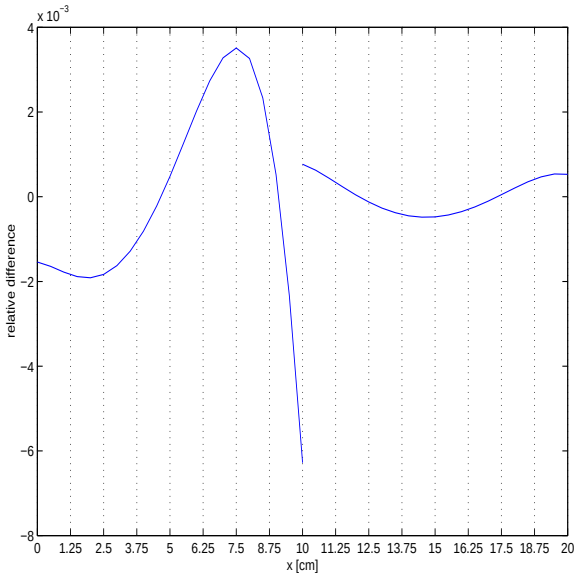

Figure 6.12: Test B. Relative difference in the thermal scalar flux calculated by the diffusion equation compared to the coarse-mesh transport solution obtained from the LOQD equations.

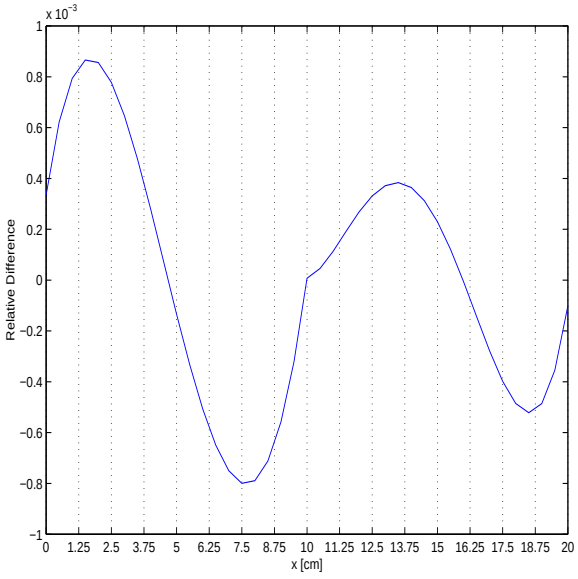

Figure 6.13: Test B. Relative difference in the fast scalar flux calculated by the splitting method compared to the results of the HOFE method.

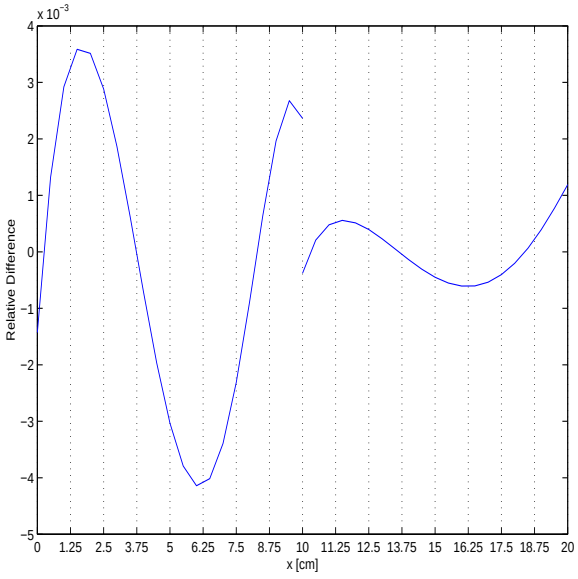

Figure 6.14: Test B. Relative difference in the thermal scalar flux calculated by the splitting method compared to the results of the HOFE method.

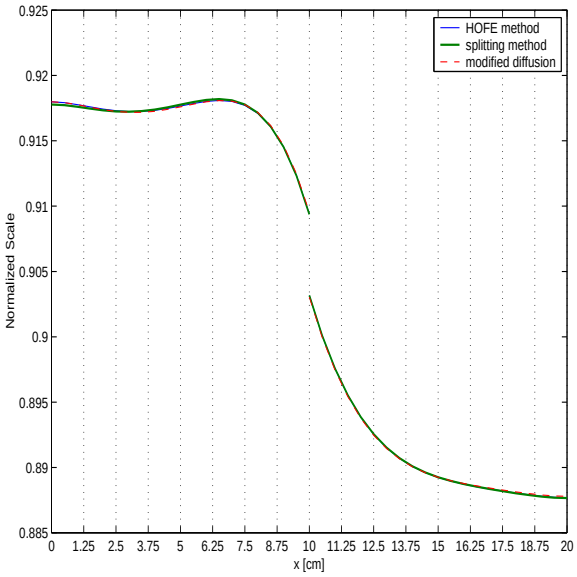

Figure 6.15: Test A. Solution of the D-problem in fast group, $\phi_D^1(x)$.

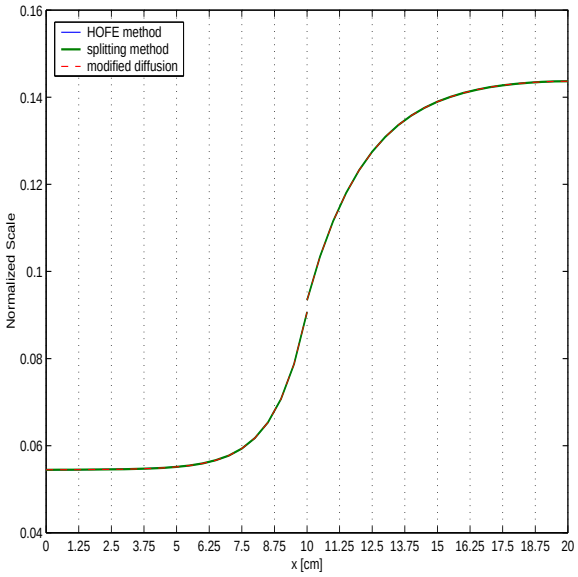

Figure 6.16: Test A. Solution of the D-problem in thermal group, $\phi_D^2(x)$.

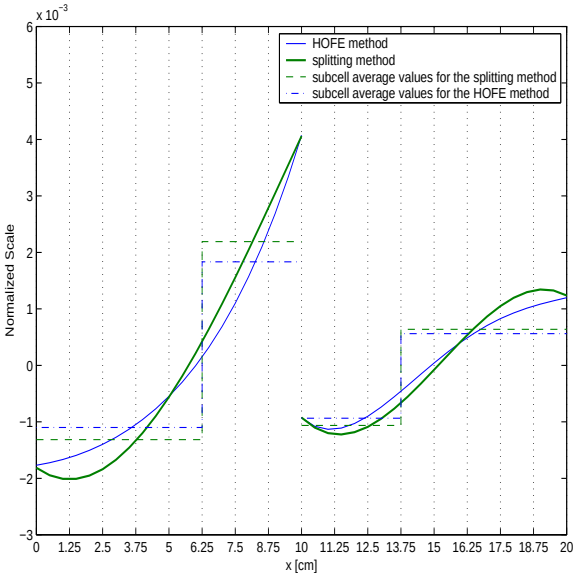

Figure 6.17: Test A. Solution of the Q-problem in fast group, $\phi_Q^1(x)$.

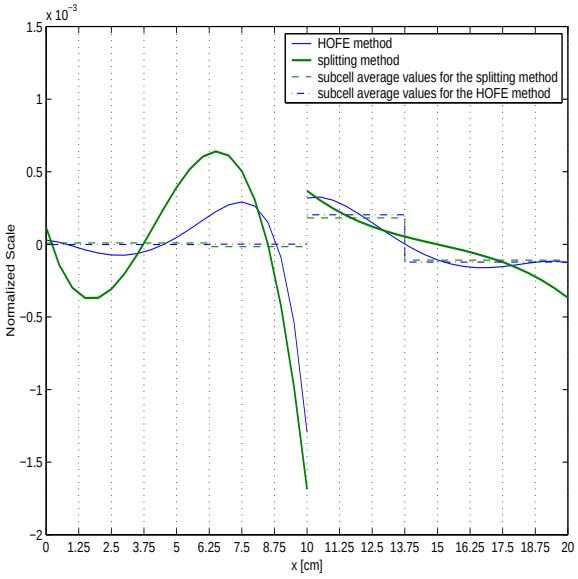

Figure 6.18: Test A. Solution of the Q-problem in thermal group, $\phi_Q^2(x)$.

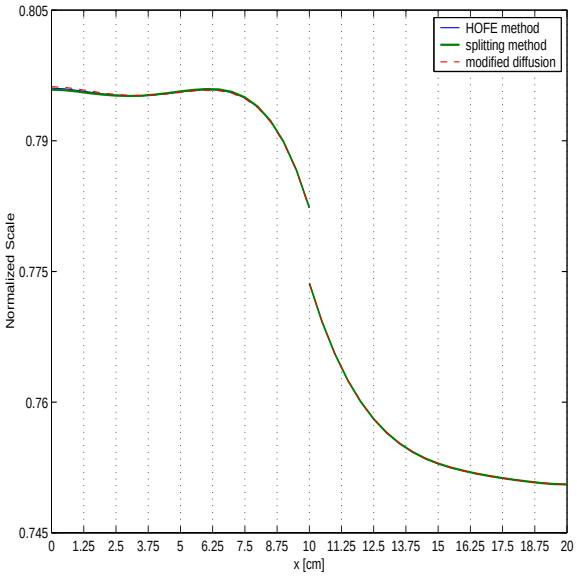

Figure 6.19: Test B. Solution of the D-problem in fast group, $\phi_D^1(x)$.

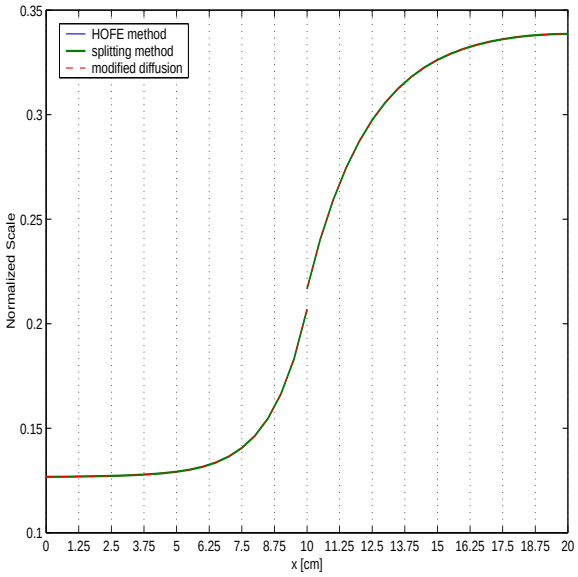

Figure 6.20: Test B. Solution of the D-problem in thermal group, $\phi_D^2(x)$.

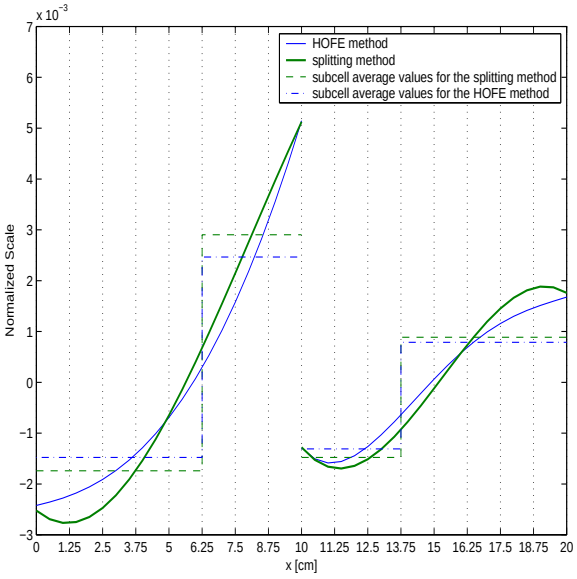

Figure 6.21: Test B. Solution of the Q-problem in fast group, $\phi_Q^1(x)$.

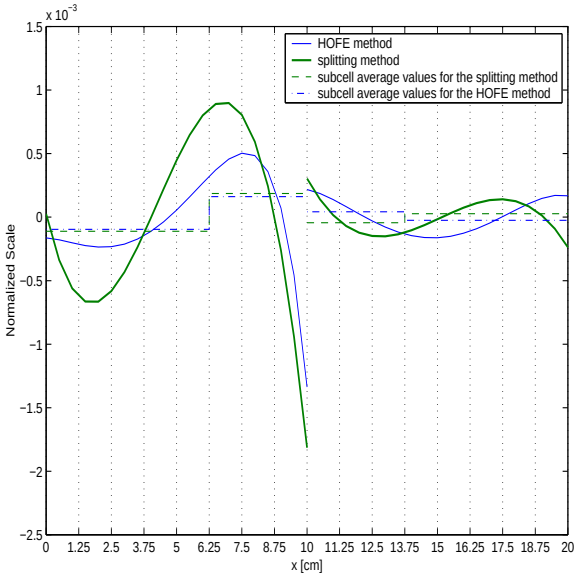

Figure 6.22: Test B. Solution of the Q-problem in thermal group, $\phi_Q^2(x)$.

interface conditions allow spatial decomposition of the Q-problem such that it can be solved in each coarse cell (part of assembly) independently of other cells. Thus, the presented splitting method enables us to reduce significantly computational costs for obtaining solution that very accurately accounts for transport effects in full-reactor calculations.

It is important to note that the proposed splitting method can be also utilized to upgrade current codes for full-reactor core calculations that are based on the diffusion theory. In such case, it is necessary to add solution of Q-problem and modify the definition of the diffusion coefficient as well as of the fission source term to account for the Q-problem solution. As a result, one gets a code based on transport theory calculations, provided that all extra group data and functionals are supplied from assembly-level calculations.

Bibliography

[1] K. S. Smith, "Assembly Homogenization Techniques for Light Water Reactor Analysis," *Progress in Nuclear Energy*, **17**, pp. 303-335 (1986).

[2] V. Y. Gol'din, "A Quasi-Diffusion Method of Solving the Kinetic Equation," *USSR Comp. Math. and Math. Phys.*, **4**, pp. 136-149 (1964).

[3] N. N. Aksenov and V. Y. Gol'din, "Computation of the Two-Dimensional Stationary Equation of Neutron Transfer by the Quasi-Diffusion Method," *USSR Comp. Math. and Math. Phys.*, **19**, No. 5, 263-266 (1979).

[4] V. Y. Gol'din, "On Mathematical Modeling of Problems of Non-Equilibrium Transfer in Physical Systems," in *Modern Problems of Mathematical Physics and Computational Mathematics*, Nauka, Moscow, 113-127 (1982) (in Russian).

[5] D. Y. Anistratov and M. L. Adams, "Consistent Coarse-Mesh Discretization of the Low-Order Equations of the Quasidiffusion Method," *Trans. Am. Nucl. Soc.,* **83**, 250-251 (2000).

[6] K. T. Clarno and M. L. Adams, "Improved Boundary Conditions for Assembly-Level Transport Codes," *Int. Conf. on the New Frontiers of Nuclear Technology: Reactor Physics, Safety and High-Performance Computing (PHYSOR 2002)*, Seoul, Korea, Oct. 7-10 (2002).

[7] R. Nes and T. S. Palmer, "An Advanced Nodal Discretization for the Quasi-Diffusion Low-Order Equations," *Int. Conf. on the New Frontiers of Nuclear Technology: Reactor Physics, Safety and High-Performance Computing (PHYSOR 2002)*, Seoul, Korea, Oct. 7-10 (2002).

[8] D. Y. Anistratov, "Homogenization Methodology for the Low-Order Equations of the Quasidiffusion Method," *Int. Conf. on the New Frontiers of Nuclear Technology: Reactor Physics, Safety and High-Performance Computing (PHYSOR 2002)*, Seoul, Korea, Oct. 7-10 (2002).

[9] V. Y. Gol'din and A. V. Kolpakov, "Nonlinear Marching Method for Solving the Multidimensional Diffusion Equation," *Preprint of the Keldysh Institute for Applied Mathematics*, the USSR Academy of Sciences, No. 22 (1982) (in Russian).

[10] V. Y. Gol'din, D. A. Gol'dina and A. V. Kolpakov, "The Solution of Two-Dimensional Stationary Quasidiffusion Problem," *Preprint of the Keldysh Institute for Applied Mathematics*, the USSR Academy of Sciences, No. 49 (1982) (in Russian).

[11] E. N. Aristova and A. V. Kolpakov, "A Combined Finite Difference Scheme for an Elliptic Operator in an Oblique-Angled Cell," *Mathematical Modeling and Computational Experiment*, **1**, 187-196 (1993).

[12] E. N. Aristova, V. Y. Gol'din, and A. V. Kolpakov, "Multidimensional Calculations of Radiation Transport by Nonlinear Quasi-Diffusion Method," *Proceeding of ANS International Conference on Mathematics and Computation, Reactor Physics and Environmental Analysis in Nuclear Applications*, Sept. 27-30, 1999, Madrid, Spain, 667-676 (1999).

[13] K. T. Clarno and M. L. Adams, "Capturing the Effects of Unlike Neighbors in Single-Assembly Calculations," *Proceedings of American Nuclear Society Topical Meeting in Mathematics & Computations, Nuclear Mathematical and Computational Sciences: A Century in Review - A Century Anew*, Gatlinburg, TN, April 6-10, 2003, 20 pp. (2003).

[14] D. Y. Anistratov, "Consistent Spatial Discretization of the Low-Order Quasidiffusion Equations on Coarse Grids," *Proceedings of American Nuclear Society Topical Meeting in Mathematics & Computations, Nuclear Mathematical and Computational Sciences: A Century in Review - A Century Anew*, Gatlinburg, TN, April 6-10, 2003, 20 pp. (2003).

[15] D. Y. Anistratov and V. Y. Gol'din, "Nonlinear Methods for Solving Particle Transport Problems," *Transport Theory and Statistical Physics*, **22**, No. 2&3, 42-77 (1993).

[16] K. S. Smith, *private communication*.

Chapter 7

A Coupled Nodal/Finite Volume Discretization of the 2D Quasidiffusion Low-Order Equations for Reactor Calculations

7.1 The Quasidiffusion Equations

The quasi-diffusion (QD) method was developed in 1964 by Gol'din[3] as a non-linear method of solving the linear Boltzmann equation. Basically, QD methods accelerate the transport schemes by using the angular flux resulted from transport sweeps to calculate the values of the scalar flux which in turn are the source of particles in the next transport sweeps. QD methods allow obtaining discrete transport solutions that are influenced by both the discretizations of the transport and the low-order diffusion-like operator. The low-order operator contains transport corrections, thus the QD-accelerated solution does not converge to unaccelerated transport solution in case of independent discretization of the low-order and transport equations [4]. However, if the size of the mesh cells tends to zero and the difference schemes for the transport and low-order equations converge, then these solutions of discretizad low-order and transport equations tend to each other and to the exact solution of the discrete-ordinates equations. Consider the general-geometry k-eigenvalue transport equation for monoenergetic neutrons with isotropic scattering

$$\hat{\Omega}\cdot\overline{\nabla}\psi(\hat{r},\hat{\Omega})+\Sigma(\hat{r})\psi(\hat{r},\hat{\Omega})=\frac{1}{4\pi}\Sigma_s(\hat{r})\Phi(\hat{r})+\frac{1}{4\pi k}\nu\Sigma_f(\hat{r})\Phi(\hat{r}) \qquad (1)$$

where

- $\hat{\Omega}$ is the particle direction unit vector
- $\psi(\hat{r},\hat{\Omega})$ is the angular neutron flux,
- $\Sigma(\hat{r})$ is the total cross section,
- $\Sigma_s(\hat{r})$ is the scattering cross section,
- $\Phi(\hat{r})$ is the scalar flux,
- k is the multiplication factor,
- ν is the number of neutrons per fission, and
- $\Sigma_f(\hat{r})$ is the fission cross section.

Integrating each term of Eq. (1) over all directions, yields[5]

$$\overline{\nabla} \cdot \overline{J} + \Sigma_r(\hat{r})\Phi(\hat{r}) = \frac{1}{4\pi} \nu\Sigma_f(\hat{r})\Phi(\hat{r}), \tag{2}$$

where we have used the definition of the scalar flux $\Phi(\hat{r})$,

$$\Phi(\hat{r}) = \int_{4\pi} \psi(\hat{r}, \hat{\Omega})\, d\Omega . \tag{3}$$

In Eq. (2), $\Sigma_r(\hat{r})$ is the removal cross-section, defined as

$$\Sigma_r(\hat{r}) = \Sigma(\hat{r}) - \Sigma_s(\hat{r}) . \tag{4}$$

Multiplying Eq. (1) by Ω_x, Ω_y, and Ω_z and integrating over all directions yields

$$J^i(\hat{r}) = -\frac{1}{\Sigma(\hat{r})} \sum_j \nabla_j (E_{ij}(\hat{r})\Phi(\hat{r})) \quad i, j = x, y, z . \tag{5}$$

In Eq. (5), $J^i(\hat{r})$ are the projections of the neutron current in each of the three dimensions and $E_{ij}(\hat{r})$ are the components of the symmetric, positive-defined Eddington tensor:

$$E_{ij}(\hat{r}) = \frac{\int_{4\pi} \Omega_i \Omega_j \psi(\hat{r}, \hat{\Omega})\, d\Omega}{\int_{4\pi} \psi(\hat{r}, \hat{\Omega})\, d\Omega} \quad i, j = x, y, z . \tag{6}$$

Equations (2) and (5) are known as the quasi-diffusion low-order (QDLO) equations. Eq. (2) is simply a balance equation and Eq. (5) is an exact definition of the transport current, which has a form similar to Fick's law.

If we consider two neutron energy groups (1=fast neutrons, 2=thermal neutrons) the QDLO equations become

$$\overline{\nabla} \cdot \overline{J_1} + \Sigma_{r1}(\hat{r})\Phi_1(\hat{r}) = \frac{1}{k}(\nu\Sigma_{f1}(\hat{r})\Phi_1(\hat{r}) + \nu\Sigma_{f2}(\hat{r})\Phi_2(\hat{r})), \tag{7}$$

$$\overline{\nabla} \cdot \overline{J_2} + \Sigma_{r2}(\hat{r})\Phi_2(\hat{r}) = \Sigma_{s12}(\hat{r})\Phi_1(\hat{r}), \tag{8}$$

and

$$J_g^i(\hat{r}) = -\frac{1}{\Sigma_g(\hat{r})} \sum_j \nabla_j (E_{g,ij}(\hat{r})\Phi_g(\hat{r})), \tag{9}$$

where

$$E_{g,ij} = \frac{\int_{4\pi} \Omega_i \Omega_j \psi_g(\hat{r},\hat{\Omega})\, d\Omega}{\int_{4\pi} \psi_g(\hat{r},\hat{\Omega})\, d\Omega} \quad \text{for } i,j = x,y,z \text{ and } g = 1,2\,. \tag{10}$$

In deriving Eqs. (7) and (8), we assumed that the only source of thermal neutrons consists of fast neutrons slowing down from group 1 to group 2 and no upscattering occurs. [In fact, an "effective" down-scattering cross section is calculated by subtracting from the downscattering cross section the upscattering cross-section times the ratio of the thermal flux to fast flux.]

7.2 The Splitting Procedure for the Solution of the QDLO Equations in 2D

We present a splitting method for solving the QDLO equations in x-y geometry, which is a natural extension of that presented in [8]. The goal of this splitting is to derive two systems of equations, whose solutions when combined will reproduce the solution of Eqs. (7)-(9). The particular choice of splitting is motivated by the spatial shape of the Eddington functionals. Observations of the spatial shape of the Eddington functionals show that they are smooth (nearly flat) in the interior of the fuel assembly, and sharply changing near the assembly boundaries. Figures 7.1-7.3 show this behavior in a MOX fuel assembly adjacent to a UO_2 fuel assembly.

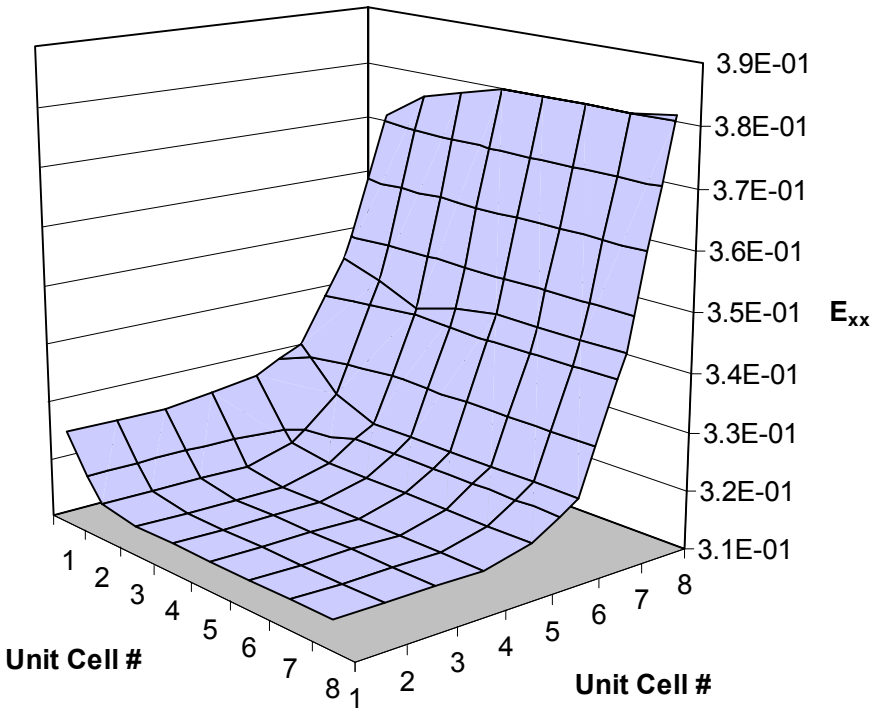

Figure 7.1: Thermal E_{xx} vs. position in a quarter MOX assembly with an unlike neighbor on one side

The QDLO equations are split into (i) a system of equations utilizing the node-averaged Eddington functional and cross-section data whose solution will be accurate in the interior of the node [the "D" problem], and (ii) a system of equations that incorporate the spatial shape of the Eddington functionals and total cross section near assembly interfaces whose solution will contain important assembly interface behavior [the "Q" problem].

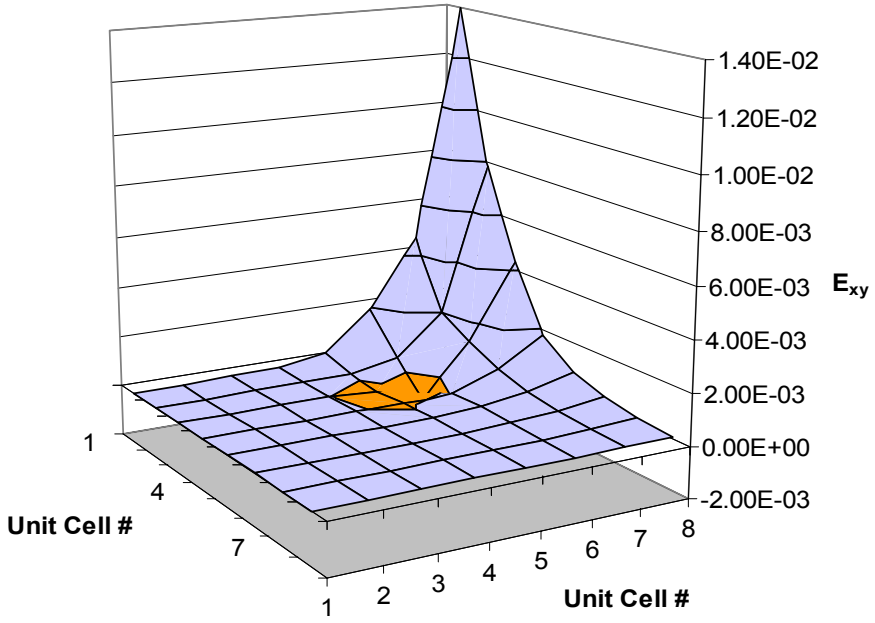

Figure 7.2: Thermal E_{xy} vs. position in a quarter MOX assembly with an unlike neighbor on one side (orange data are negative numbers)

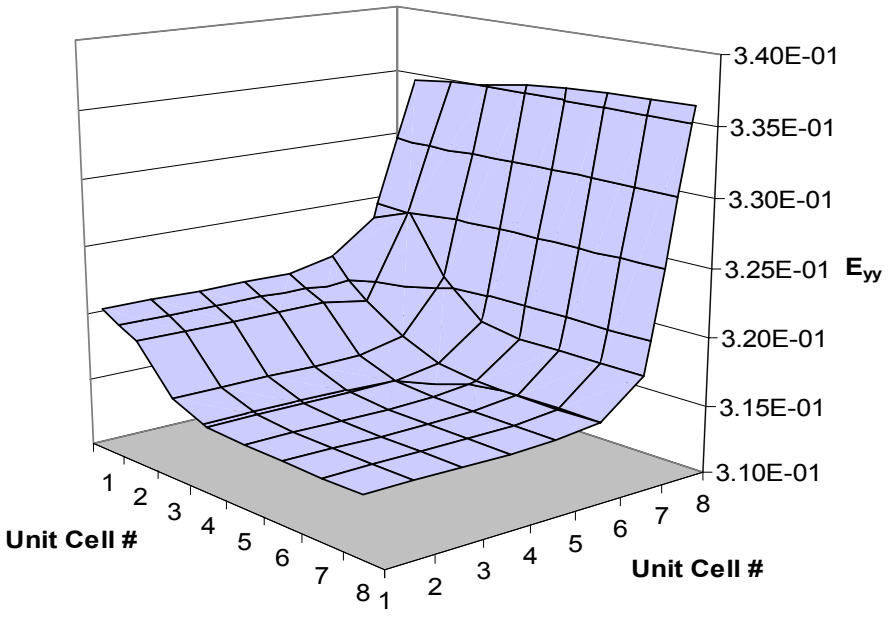

Figure 7.3: Thermal E_{yy} vs. position in a quarter MOX assembly with an unlike neighbor on one side

In x-y geometry, the "D" problem is defined by

$$\overline{\nabla} \cdot \overline{J_1^D} + \Sigma_{r1}(\hat{r})\Phi_1^D(\hat{r}) = \frac{1}{k}(\nu\Sigma_{f1}(\hat{r})[\Phi_1^D(\hat{r}) + \Phi_1^Q(\hat{r})] + \nu\Sigma_{f2}(\hat{r})[\Phi_2^D(\hat{r}) + \Phi_2^Q(\hat{r})]), \tag{11}$$

$$\overline{\nabla} \cdot \overline{J_2^D} + \Sigma_{r2}(\hat{r})\Phi_2^D(\hat{r}) = \Sigma_{s12}(\hat{r})\Phi_1^D(\hat{r}), \tag{12}$$

and

$$J_1^{D,x}(\hat{r}) = -\frac{1}{\langle\Sigma\rangle_1}[\langle E\rangle_{1,xx}\frac{\partial\Phi_1^D}{\partial x}(\hat{r}) + \langle E\rangle_{1,xy}\frac{\partial\Phi_1^D}{\partial y}(\hat{r})], \tag{13a}$$

$$J_1^{D,y}(\hat{r}) = -\frac{1}{\langle\Sigma\rangle_1}[\langle E\rangle_{1,xy}\frac{\partial\Phi_1^D}{\partial x}(\hat{r}) + \langle E\rangle_{1,yy}\frac{\partial\Phi_1^D}{\partial y}(\hat{r})], \tag{13b}$$

$$J_2^{D,x}(\hat{r}) = -\frac{1}{\langle\Sigma\rangle_2}[\langle E\rangle_{2,xx}\frac{\partial\Phi_2^D}{\partial x}(\hat{r}) + \langle E\rangle_{2,xy}\frac{\partial\Phi_2^D}{\partial y}(\hat{r})], \tag{14a}$$

$$J_2^{D,y}(\hat{r}) = -\frac{1}{\langle\Sigma\rangle_2}[\langle E\rangle_{2,xy}\frac{\partial\Phi_2^D}{\partial x}(\hat{r}) + \langle E\rangle_{2,yy}\frac{\partial\Phi_2^D}{\partial y}(\hat{r})]. \tag{14b}$$

In these equations, the angle brackets [$\langle E\rangle$ and $\langle\Sigma\rangle$] indicate node-averaged data. We will discuss the preparation of this data in a later section of this report.

The "Q" problem is defined by

$$\overline{\nabla} \cdot \overline{J_1^Q} + \Sigma_{r1}(\hat{r})\Phi_1^Q(\hat{r}) = 0\,, \tag{15}$$

$$\overline{\nabla} \cdot \overline{J_2^Q} + \Sigma_{r2}(\hat{r})\Phi_2^Q(\hat{r}) = \Sigma_{s12}(\hat{r})\Phi_1^Q(\hat{r})\,, \tag{16}$$

and

$$\begin{aligned}
J_1^{Q,x}(\hat{r}) = &-\frac{1}{\Sigma_1(\hat{r})}\left[\frac{\partial}{\partial x}\left(E_{1,xx}(\hat{r})\Phi_1^Q(\hat{r})\right) + \frac{\partial}{\partial y}\left(E_{1,xy}(\hat{r})\Phi_1^Q(\hat{r})\right)\right] \\
&+ \frac{\langle E\rangle_{1,xx}}{\langle\Sigma\rangle_1}\frac{\partial\Phi_1^D}{\partial x}(\hat{r}) - \frac{1}{\Sigma_1(\hat{r})}\frac{\partial}{\partial x}\left[E_{1,xx}(\hat{r})\Phi_1^D(\hat{r})\right] \\
&+ \frac{\langle E\rangle_{1,xy}}{\langle\Sigma\rangle_1}\frac{\partial\Phi_1^D}{\partial y}(\hat{r}) - \frac{1}{\Sigma_1(\hat{r})}\frac{\partial}{\partial y}\left[E_{1,xy}(\hat{r})\Phi_1^D(\hat{r})\right]
\end{aligned} \tag{17a}$$

$$\begin{aligned}
J_1^{Q,y}(\hat{r}) = &-\frac{1}{\Sigma_1(\hat{r})}\left[\frac{\partial}{\partial x}\left(E_{1,xy}(\hat{r})\Phi_1^Q(\hat{r})\right) + \frac{\partial}{\partial y}\left(E_{1,yy}(\hat{r})\Phi_1^Q(\hat{r})\right)\right] \\
&+ \frac{\langle E\rangle_{1,xy}}{\langle\Sigma\rangle_1}\frac{\partial\Phi_1^D}{\partial x}(\hat{r}) - \frac{1}{\Sigma_1(\hat{r})}\frac{\partial}{\partial x}\left[E_{1,xy}(\hat{r})\Phi_1^D(\hat{r})\right] \\
&+ \frac{\langle E\rangle_{1,yy}}{\langle\Sigma\rangle_1}\frac{\partial\Phi_1^D}{\partial y}(\hat{r}) - \frac{1}{\Sigma_1(\hat{r})}\frac{\partial}{\partial y}\left[E_{1,yy}(\hat{r})\Phi_1^D(\hat{r})\right]
\end{aligned} \tag{17b}$$

$$\begin{aligned}
J_2^{Q,x}(\hat{r}) = &-\frac{1}{\Sigma_2(\hat{r})}\left[\frac{\partial}{\partial x}\left(E_{2,xx}(\hat{r})\Phi_2^Q(\hat{r})\right) + \frac{\partial}{\partial y}\left(E_{2,xy}(\hat{r})\Phi_2^Q(\hat{r})\right)\right] + \\
&\frac{\langle E\rangle_{2,xx}}{\langle\Sigma\rangle_2}\frac{\partial\Phi_2^D}{\partial x}(\hat{r}) - \frac{1}{\Sigma_2(\hat{r})}\frac{\partial}{\partial x}\left[E_{2,xx}(\hat{r})\Phi_2^D(\hat{r})\right] \\
&+ \frac{\langle E\rangle_{2,xy}}{\langle\Sigma\rangle_2}\frac{\partial\Phi_2^D}{\partial y}(\hat{r}) - \frac{1}{\Sigma_2(\hat{r})}\frac{\partial}{\partial y}\left[E_{2,xy}(\hat{r})\Phi_2^D(\hat{r})\right]
\end{aligned} \tag{18a}$$

$$\begin{aligned}
J_2^{Q,y}(\hat{r}) = &-\frac{1}{\Sigma_2(\hat{r})}\left[\frac{\partial}{\partial x}\left(E_{2,xy}(\hat{r})\Phi_2^Q(\hat{r})\right) + \frac{\partial}{\partial y}\left(E_{2,yy}(\hat{r})\Phi_2^Q(\hat{r})\right)\right] \\
&+ \frac{\langle E\rangle_{2,xy}}{\langle\Sigma\rangle_2}\frac{\partial\Phi_2^D}{\partial x}(\hat{r}) - \frac{1}{\Sigma_2(\hat{r})}\frac{\partial}{\partial x}\left[E_{2,xy}(\hat{r})\Phi_2^D(\hat{r})\right] \\
&+ \frac{\langle E\rangle_{2,yy}}{\langle\Sigma\rangle_2}\frac{\partial\Phi_2^D}{\partial y}(\hat{r}) - \frac{1}{\Sigma_2(\hat{r})}\frac{\partial}{\partial y}\left[E_{2,yy}(\hat{r})\Phi_2^D(\hat{r})\right]
\end{aligned} \tag{18b}$$

The complete solution to the QDLO equations is reconstructed by summing the D and Q pieces:

$$\Phi_g(\hat{r}) = \Phi_g^D(\hat{r}) + \Phi_g^Q(\hat{r}), \quad g = 1,2 \tag{19a}$$

$$\bar{J}_g(\hat{r}) = \bar{J}_g^D(\hat{r}) + \bar{J}_g^Q(\hat{r}), \quad g = 1,2 \tag{19b}$$

We must also constrain these equations with boundary conditions on the outer boundaries of the problem. The QDLO boundary condition has the form:

$$\bar{n}(\hat{r}_s) \cdot \overline{J_g}(\hat{r}_s) = C_g(\hat{r}_s)\Phi_g(\hat{r}_s), \tag{20}$$

where $\hat{r}_s$ is a position on the problem boundary, and $C_g(\hat{r}_s)$ is a fractional functional defined by

$$C_g(\hat{r}_s) = \frac{\int_{\hat{n}(\hat{r}_s)\cdot\hat{\Omega}<0} \left|\hat{n}(\hat{r}_s)\cdot\hat{\Omega}\right| \psi(\hat{r}_s,\hat{\Omega})\, d\Omega}{\int_{\hat{n}(\hat{r}_s)\cdot\hat{\Omega}<0} \psi(\hat{r}_s,\hat{\Omega})\, d\Omega}. \tag{21}$$

While $C_g(\hat{r}_s)$ is shown as an analytic function of space, we will employ relationships that are averaged over boundary surfaces. We split Eq. (20) by using the same C_g for both the D and Q equations:

$$\bar{n}(\hat{r}_s) \cdot \overline{J_g^D}(\hat{r}_s) = C_g(\hat{r}_s)\Phi_g^D(\hat{r}_s), \tag{22a}$$

$$\bar{n}(\hat{r}_s) \cdot \overline{J_g^Q}(\hat{r}_s) = C_g(\hat{r}_s)\Phi_g^Q(\hat{r}_s). \tag{22b}$$

The D and Q problems are coupled, meaning an iteration procedure is required. In order to allow Inverse Power Iteration to be applied to the solution of the *k*-eigenvalue problem, we employ the following iteration procedure:

1. Begin with an initial guess for *k* and the fission source,
2. Solve Eqs. (12)-(14) subject to boundary conditions Eq. (22a) for Φ_g^D,
3. Solve Eqs. (15)-(18) subject to boundary conditions Eq. (22b) for Φ_g^Q, using Φ_g^D from step 2.
4. Compute a new estimate of *k* from this relationship:

$$k = \frac{\int_V [\nu\Sigma_{f1}(\Phi_1^D + \Phi_1^Q) + \nu\Sigma_{f2}(\Phi_2^D + \Phi_2^Q)]\, dV}{\int_{\partial V} [\hat{n}\cdot(\bar{J}_1^D + \bar{J}_1^Q) + \hat{n}\cdot(\bar{J}_2^D + \bar{J}_2^Q)]\, dA + \int_V [\Sigma_{a1}(\Phi_1^D + \Phi_1^Q) + \Sigma_{a2}(\Phi_2^D + \Phi_2^Q)]\, dV} \tag{23}$$

where ∂V and V indicate the boundary and domain of the problem respectively.

It is important to note that the hyperbolic basis functions are the analytic solution of the zero-source thermal QDLO equation with constant Eddington functionals and cross sections. We have made a slight modification [11] to the splitting methodology to account for the within-node spatial variation of the total cross section.

There are two types of calculations to be performed in the characterization of the reactor core. The first is the calculation of surface and corner discontinuity factors, and the second is the global core calculation that incorporates the discontinuity factors at node interfaces.

In the discontinuity factor calculation, we use the *k*-eigenvalue, total fission source, and node surface net currents from the fine-mesh, fine-group transport calculation as a source to calculate the spatial shape of the two group fluxes. This means that we no longer perform an Inverse Power iteration to find the eigenvalue and power distribution. [Using the node-averaged cross-sections, eigenvalue, total fission source and net currents ensures that we will preserve the transport node averaged flux.] The D and Q problems are still coupled through fission term, and an iteration is still necessary. The transport net currents are used as the boundary condition for the D solution, and zero current boundary conditions are used in the Q problem. This is one possible splitting of the boundary condition; others have been considered, but this splitting has proven successful in one dimension so we extend it here to 2D. Surface and corner discontinuity factors are defined by

$$G_g^{s,c} = \left. \frac{\Phi_g^{fm}}{\left(\Phi_g^D + \Phi_g^Q\right)} \right|_{s,c}, \tag{24}$$

where *s* refers to surface average quantities, and *c* refers to evaluation at a corner of the node.

In the global calculation, we impose continuity conditions on the current at node interfaces and discontinuity conditions on the scalar flux at node interfaces and corners:

$$\begin{aligned} J_g^{x,s}\Big|_{\hat{r}=\text{vertical surface-0}} &= J_g^{x,s}\Big|_{\hat{r}=\text{vertical surface+0}}, \\ J_g^{y,s}\Big|_{\hat{r}=\text{horizontal surface-0}} &= J_g^{y,s}\Big|_{\hat{r}=\text{horizontal surface+0}}, \end{aligned} \tag{25}$$

$$\begin{aligned} G_g^s \Phi_g^s\Big|_{\hat{r}=\text{surface-0}} &= G_g^s \Phi_g^s\Big|_{\hat{r}=\text{surface+0}}, \\ G_g^c \Phi_g^c\Big|_{\hat{r}=\text{corner-0}} &= G_g^c \Phi_g^c\Big|_{\hat{r}=\text{corner+0}}. \end{aligned} \tag{26}$$

We choose the following splitting of these equations:

$$
\begin{aligned}
J_g^{D,x,s}\Big|_{\hat{r}=\text{vertical surface-0}} &= J_g^{D,x,s}\Big|_{\hat{r}=\text{vertical surface+0}}, \\
J_g^{D,y,s}\Big|_{\hat{r}=\text{horizontal surface-0}} &= J_g^{D,y,s}\Big|_{\hat{r}=\text{horizontal surface+0}}, \\
J_g^{Q,x,s}\Big|_{\hat{r}=\text{surface}} &= J_g^{Q,x,s}\Big|_{\hat{r}=\text{surface}} = 0,
\end{aligned}
\tag{27}
$$

$$
\begin{aligned}
G_g^s\left(\Phi_g^{D,s} + \Phi_g^{Q,s}\right)_{\hat{r}=\text{surface-0}} &= G_g^s\left(\Phi_g^{D,s} + \Phi_g^{Q,s}\right)_{\hat{r}=\text{surface+0}}, \\
G_g^c\left(\Phi_g^{D,c} + \Phi_g^{Q,c}\right)_{\hat{r}=\text{corner-0}} &= G_g^c\left(\Phi_g^{D,c} + \Phi_g^{Q,c}\right)_{\hat{r}=\text{corner+0}}.
\end{aligned}
\tag{28}
$$

7.3 Discretizing the "D" Problem: Extending the Advanced Nodal Discretization of Palmtag

In this section, we describe a nodal discretization of the "D" problem. This nodal method is an extension of the weighted residual method described by Palmtag, and uses polynomial basis functions to represent the fast flux, and both polynomial and hyperbolic basis functions to represent the scalar flux. The hyperbolic basis functions are chosen to be the analytic solutions of the thermal group modified tensor diffusion equation with zero source. Incorporating these hyperbolic functions into the expansion for the thermal flux permits the thermal polynomial coefficients to be written directly as a function of the fast polynomial coefficients, reducing the number of unknowns that must be computed in each node.

Other discretizations of the "D" problem are possible; in fact, Hiruta and Anistratov [9] have developed a finite element discretization with polynomial and hyperbolic basis functions for the 1D QDLO equations and are currently working to extend this method to two dimensions.

We begin by defining the problem domain as the $x-y$ plane divided into non-overlapping

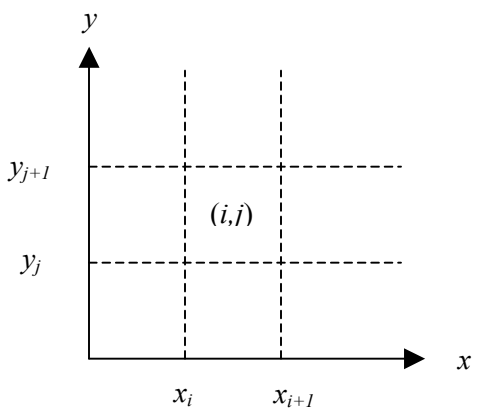

Figure 7.4: 2-D representation of a square node located at position x_i, y_j

square regions (nodes) of dimension h. Non-dimensional coordinates (u,v) are introduced, and Figure 7.4 illustrates these for a square node that occupies the position (i,j) in a regular array.

Based on the geometry of the problem, the coordinates (u,v) are defined by

$$u = \frac{2x - x_{i+1} - x_i}{2h}, \tag{29}$$

and

$$v = \frac{2y - y_{j+1} - y_j}{2h}. \tag{30}$$

Using these coordinates, assuming constant cross-sections and Eddington tensor components, and inserting the neutron currents given by Eqs. (13)-(14) into Eqs. (11) and (12), the balance equations become

$$\begin{aligned} -\frac{1}{h^2}\Big(&\frac{\langle E\rangle_{1,xx}}{\langle\Sigma\rangle_1}\frac{\partial^2\Phi_1^D(u,v)}{\partial u^2} + 2\frac{\langle E\rangle_{1,xy}}{\langle\Sigma\rangle_1}\frac{\partial^2\Phi_1^D(u,v)}{\partial u\partial v} + \\ &\frac{\langle E\rangle_{1,yy}}{\langle\Sigma\rangle_1}\frac{\partial^2\Phi_1^D(u,v)}{\partial v^2}\Big) + \Sigma_{r1}\Phi_1^D(u,v) \\ = \frac{1}{k}\big(&\nu\Sigma_{f1}(\Phi_1^D(u,v) + \Phi_1^Q(u,v)) + \nu\Sigma_{f2}(\Phi_2^D(u,v) + \Phi_2^Q(u,v))\big), \end{aligned} \tag{31}$$

and

$$\begin{aligned} -\frac{1}{h^2}\Big(&\frac{\langle E\rangle_{2,xx}}{\langle\Sigma\rangle_2}\frac{\partial^2\Phi_2^D(u,v)}{\partial u^2} + 2\frac{\langle E\rangle_{2,xy}}{\langle\Sigma\rangle_2}\frac{\partial^2\Phi_2^D(u,v)}{\partial u\partial v} + \\ &\frac{\langle E\rangle_{2,yy}}{\langle\Sigma\rangle_2}\frac{\partial^2\Phi_2^D(u,v)}{\partial v^2}\Big) + \Sigma_{r2}\Phi_2^D(u,v) \\ &= \Sigma_{s12}\Phi_1^D(u,v). \end{aligned} \tag{32}$$

[We have, for the moment ignored the Q component of the flux in the fission source in Eqs. (31) and (32). We discuss this omission later in this section.] The Eddington functionals in these D equations are averages over the interior region of the node, where their spatial shapes are relatively smooth. The removal, fission and downscattering cross sections are true node averages, and the total cross sections are averages over the node outer boundary pin cell rows.

The method used to spatially discretize equations (31) and (32) is the method of weighted residuals (MWR). The fast flux in the interior of each node is approximated by a 2-D, non-separable expansion of polynomial functions:

$$\Phi_1^D(u,v) = \sum_{m=0}^{4}\sum_{n=0}^{4} a_{mn} f_m(u) f_n(v) \,. \tag{33}$$

The functions f_m are polynomial basis functions of the form

$$\begin{aligned} f_0(\xi) &= 1, \\ f_1(\xi) &= \xi, \\ f_2(\xi) &= 3\xi^2 - \frac{1}{4}, \\ f_3(\xi) &= 4\xi(\xi + \frac{1}{2})(\xi - \frac{1}{2}), \\ f_4(\xi) &= (\xi^2 - \frac{1}{20})(\xi + \frac{1}{2})(\xi - \frac{1}{2}). \end{aligned} \tag{34}$$

The thermal flux is approximated by a 2-D, non-separable, expansion of polynomial and hyperbolic functions

$$\Phi_2^D(u,v) = \sum_{m=0}^{4}\sum_{n=0}^{4} b_{mn} f_m(u) f_n(v) + \sum_{l=1}^{8} c_l g_l(u,v). \tag{35}$$

In Eqs. (33) and (35) only 15 of 25 a_{mn} coefficients and 19 of 25 b_{mn} coefficients are non-zero.

The hyperbolic basis functions used in (35) are

$$
\begin{aligned}
g_1(u,v) &= \cosh(\gamma_1 u),\\
g_2(u,v) &= \sinh(\gamma_1 u),\\
g_3(u,v) &= \cosh(\gamma_2 v),\\
g_4(u,v) &= \cosh(\gamma_2 v),\\
g_5(u,v) &= \cosh(\gamma_3 (v-\theta_1 u)/\sqrt{2}),\\
g_6(u,v) &= \sinh(\gamma_3 (v-\theta_1 u)/\sqrt{2}),\\
g_7(u,v) &= \cosh(\gamma_3 (v-\theta_2 u)/\sqrt{2}),\\
g_8(u,v) &= \sinh(\gamma_3 (v-\theta_2 u)/\sqrt{2}),
\end{aligned}
\tag{36}
$$

with

$$
\begin{aligned}
\gamma_1 &= \sqrt{\frac{h^2 \Sigma_{r2} \langle \Sigma \rangle_2}{\langle E \rangle_{2xx}}},\\
\gamma_2 &= \sqrt{\frac{h^2 \Sigma_{r2} \langle \Sigma \rangle_2}{\langle E \rangle_{2yy}}},\\
\gamma_3 &= \sqrt{\frac{h^2 \Sigma_{r2} \langle \Sigma \rangle_2 \langle E \rangle_{2xx}}{\langle E \rangle_{2xx} \langle E \rangle_{2yy} - \langle E \rangle_{2xy}^2}},\\
\theta_1 &= \frac{\langle E \rangle_{2xy} + \sqrt{-\langle E \rangle_{2xy}^2 + \langle E \rangle_{2xx} \langle E \rangle_{2yy}}}{\langle E \rangle_{2xx}},\\
\theta_2 &= \frac{\langle E \rangle_{2xy} - \sqrt{-\langle E \rangle_{2xy}^2 + \langle E \rangle_{2xx} \langle E \rangle_{2yy}}}{\langle E \rangle_{2xx}}.
\end{aligned}
\tag{37}
$$

These functions are exact (analytic) solutions of the zero-source thermal neutron balance equation [Eq. (32)] given constant cross sections and Eddington functionals.

The weighted residual method requires a set of weight functions, which we choose to be the low-order polynomials:

$$
\begin{aligned}
w_0(u,v) &= 1,\\
w_1(u,v) &= f_1(u),\\
w_2(u,v) &= f_1(v),\\
w_3(u,v) &= 144 f_1(u) f_1(v),\\
w_4(u,v) &= 4 f_2(u),\\
w_5(u,v) &= 4 f_2(v),\\
w_6(u,v) &= 16 f_2(u) f_2(v).
\end{aligned}
\tag{38}
$$

We define the *n*-th weighted moment of a function $R(u,v)$ by

$$\left\langle w_n(u,v), R(u,v)\right\rangle = \int_{-1/2}^{1/2}\int_{-1/2}^{1/2} R(u,v)\, w_n(u,v)\, du\, dv\,. \tag{39}$$

The zero-th weighted moment of the fast and thermal neutron fluxes represent node-averaged quantities. The average fast flux is thus $\overline{\overline{\Phi_1}} = a_{00}$ and the average thermal flux is given by

$$\begin{aligned}\overline{\overline{\Phi_2}} &= b_{00} + \frac{2}{\gamma_1} c_1 \sinh(\frac{\gamma_1}{2}) + \frac{2}{\gamma_2} c_3 \sinh(\frac{\gamma_2}{2}) \\ &+ \frac{8}{\gamma_3^2\theta_1} c_5 \sinh(\frac{\gamma_3}{2\sqrt{2}})\sinh(\frac{\gamma_3\theta_1}{2\sqrt{2}}) + \frac{8}{\gamma_3^2\theta_2} c_7 \sinh(\frac{\gamma_3}{2\sqrt{2}})\sinh(\frac{\gamma_3\theta_2}{2\sqrt{2}}).\end{aligned} \tag{40}$$

In order to solve the quasidiffusion low-order equations by the MWR, 23 equations for 23 coefficients are needed for each node of the problem. The 23 equations are generated from the following conditions:

- 7 weighted residual moments in the fast group
- 4 surface-averaged continuity conditions in the fast group
- 4 surface-averaged continuity conditions in the thermal group
- 4 corner conditions in the fast group
- 4 corner conditions in the thermal group.

The 19 thermal polynomial expansion coefficients are expressed in terms of the 15 fast flux expansion coefficients based on fact that the hyperbolic basis functions [Eq. (27)] are analytic solutions of the zero-source thermal neutron balance equations with spatially constant components of the Eddington tensor and cross-sections.

The previously reported one-dimensional splitting procedure [8] used a finite element discretization of the fast and thermal D equations, and the thermal polynomial coefficients were not represented directly in terms of the fast polynomial coefficients. Our 2D procedure will require fewer unknowns to be computed in each node of the global matrix than that of a comparable finite element procedure (23 unknowns vs 30 if both thermal and fast fluxes are expanded in terms of 15 polynomial coefficients).

The coupling of the D and Q problems through the fission source in Eq. (11) implies that weighted moments of the Q solution will be required to iterate the system to convergence. In the next section we describe the discretization of the Q problem, and introduce a procedure for calculating these moments.

7.4 Discretizing the "Q" Problem: Applying the Finite Volume Methodology of Gol'din

To solve the Q problem, we subdivide each node (the coarse mesh) into four subcells and apply the finite volume methodology of Gol'din. Figure 7.2 shows a single node (1/4 of a fuel assembly with N^2 unit cells) and the associated subcell mesh we use to discretize the Q problem. We have chosen a $(N-2)\times(N-2)$ interior subcell, a 2×2 corner subcell, and two edge subcells.

The black lines in the interior of the square node on the right of Figure 7.2 are the submesh cell boundaries. The red and green dotted lines, in combination with the black lines, indicate the volumes used to calculate the submesh surface Eddington functionals and total cross section (transport cross section if anisotropic scattering is included).

Gol'din's finite volume discretization involves integrations of the coupled first-order form of the Q equations [Eqs. (15)-(18)]. First, we integrate Eqs. (15) and (16) over each of the four subcell volumes:

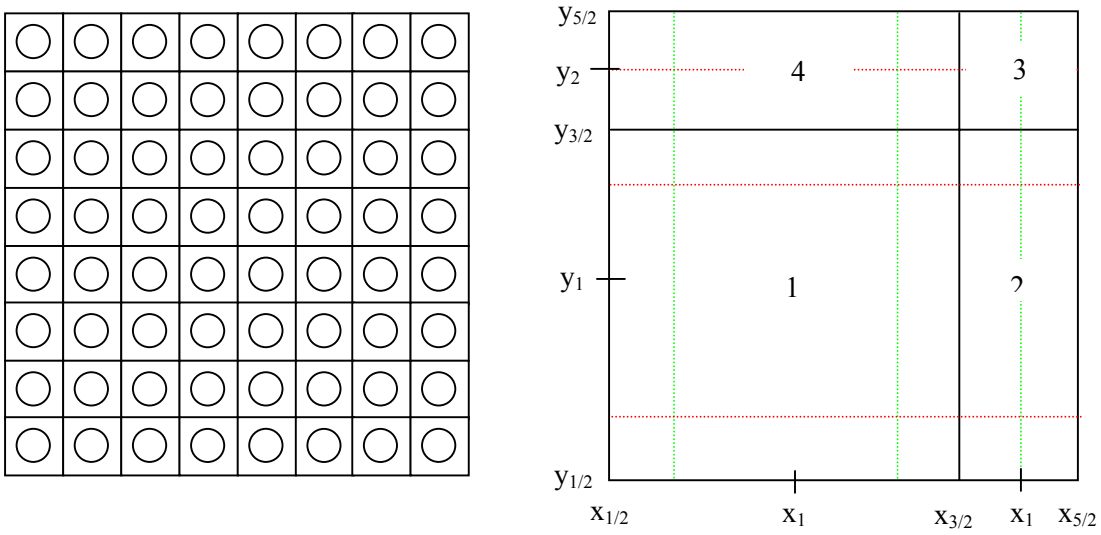

Figure 7.5: A quarter assembly node and the subcell mesh used to discretize the Q problem

$$\Delta y_j[J^{Q,x}_{g,i+1/2,j}-J^{Q,x}_{g,i-1/2,j}]+\Delta x_j[J^{Q,y}_{g,i,j+1/2}-J^{Q,y}_{g,i,j-1/2}]+\Sigma_{r,g,i,j}\Phi^{Q}_{g,i,j}=\begin{cases}0, & g=1\\ \Sigma_{s12,g,i,j}\Phi^{Q}_{1,i,j}, & g=2\end{cases} \tag{42}$$

for subcell mesh indices $i,j=1,2$ and groups $g=1,2$. This equation relates subcell average values of Q scalar flux to subcell surface values of Q current. To generate

equations for the subcell surface currents, we integrate Eqs. (17) and (18) over subcell half-volumes. For example, to generate an equation for the x-component of the fast Q current on surface (i=1/2, j=1), we integrate Eq. (17a) over x from $x_{1/2}$ to x_1 and over y from $y_{1/2}$ to $y_{3/2}$:

$$\begin{aligned}
\frac{\Delta x_1 \Delta y_1}{2}\widetilde{\Sigma}_{1,1/2,1}J^{Q,x}_{1,1/2,1} &= -\Delta y_1\left[\widetilde{E}_{1,xx,1,1}\Phi^{Q}_{1,1,1}-\widetilde{E}_{1,xx,1/2,1}\Phi^{Q}_{1,1/2,1}\right] \\
&\quad -\frac{\Delta x_1}{2}\left[\widetilde{E}_{1,xy,1,3/2}\Phi^{Q}_{1,1,3/2}-\widetilde{E}_{1,xy,1,1/2}\Phi^{Q}_{1,1,1/2}\right] \\
&\quad +\Delta y_1\left[\left(\frac{\widetilde{\Sigma}_{1,1,1}\langle E\rangle_{1,xx}}{\langle\Sigma\rangle_1}-\widetilde{E}_{1,xx,1,1}\right)\Phi^{D}_{1,1,1}-\left(\frac{\widetilde{\Sigma}_{1,1/2,1}\langle E\rangle_{1,xx}}{\langle\Sigma\rangle_1}-\widetilde{E}_{1,xx,1/2,1}\right)\Phi^{D}_{1,1/2,1}\right] \\
&\quad +\frac{\Delta x_1}{2}\left[\left(\frac{\widetilde{\Sigma}_{1,1,3/2}\langle E\rangle_{1,xy}}{\langle\Sigma\rangle_1}-\widetilde{E}_{1,xy,1,3/2}\right)\Phi^{D}_{1,1,3/2}-\left(\frac{\widetilde{\Sigma}_{1,1,1/2}\langle E\rangle_{1,xy}}{\langle\Sigma\rangle_1}-\widetilde{E}_{1,xy,1,1/2}\right)\Phi^{D}_{1,1,1/2}\right]
\end{aligned} \tag{43}$$

This equation relates subcell surface Q currents to subcell average and surface Q and D fluxes. The D fluxes in this equation are obtained by performing the appropriate averaging of the basis function expansions using the most recent values of the expansion coefficients from step (2) of our iterative procedure.

We can derive a similar equation for the y-component of the fast Q current on the surface (i=1, j=1/2), by integrating Eq. (17b) over x from $x_{1/2}$ to $x_{3/2}$ and over y from $y_{1/2}$ to y_1:

$$\begin{aligned}
\frac{\Delta x_1 \Delta y_1}{2}\widetilde{\Sigma}_{1,1,1/2}J^{Q,y}_{1,1,1/2} &= -\Delta x_1\left[\widetilde{E}_{1,yy,1,1}\Phi^{Q}_{1,1,1}-\widetilde{E}_{1,yy,1,1/2}\Phi^{Q}_{1,1,1/2}\right] \\
&\quad -\frac{\Delta y_1}{2}\left[\widetilde{E}_{1,xy,3/2,1}\Phi^{Q}_{1,3/2,1}-\widetilde{E}_{1,xy,1/2,1}\Phi^{Q}_{1,1/2,1}\right] \\
&\quad +\Delta x_1\left[\left(\frac{\widetilde{\Sigma}_{1,1,1}\langle E\rangle_{1,yy}}{\langle\Sigma\rangle_1}-\widetilde{E}_{1,yy,1,1}\right)\Phi^{D}_{1,1,1}-\left(\frac{\widetilde{\Sigma}_{1,1,1/2}\langle E\rangle_{1,yy}}{\langle\Sigma\rangle_1}-\widetilde{E}_{1,yy,1,1/2}\right)\Phi^{D}_{1,1,1/2}\right] \\
&\quad +\frac{\Delta y_1}{2}\left[\left(\frac{\widetilde{\Sigma}_{1,3/2,1}\langle E\rangle_{1,yy}}{\langle\Sigma\rangle_1}-\widetilde{E}_{1,xy,3/2,1}\right)\Phi^{D}_{1,3/2,1}-\left(\frac{\widetilde{\Sigma}_{1,1/2,1}\langle E\rangle_{1,yy}}{\langle\Sigma\rangle_1}-\widetilde{E}_{1,xy,1/2,1}\right)\Phi^{D}_{1,1/2,1}\right]
\end{aligned} \tag{44}$$

Subcell surface Q currents in the interior of the node have somewhat more complicated equations. For example, the x-component of the fast Q current on the surface (i=3/2, j=1), is generated by integrating Eq. (17a) over x from x_1 to x_2 and over y from $y_{1/2}$ to $y_{3/2}$:

$$\left(\frac{\Delta x_1+\Delta x_2}{2}\right)\Delta y_1\widetilde{\Sigma}_{1,3/2,1}J^{Q,x}_{1,3/2,1}=-\Delta y_1\left[\widetilde{E}_{1,xx,2,1}\Phi^{Q}_{1,2,1}-\widetilde{E}_{1,xx,1,1}\Phi^{Q}_{1,1,1}\right]$$
$$-\frac{\Delta x_1}{2}\left[\widetilde{E}_{1,xy,1,3/2}\Phi^{Q}_{1,1,3/2}-\widetilde{E}_{1,xy,1,1/2}\Phi^{Q}_{1,1,1/2}\right]$$
$$-\frac{\Delta x_2}{2}\left[\widetilde{E}_{1,xy,2,3/2}\Phi^{Q}_{1,2,3/2}-\widetilde{E}_{1,xy,2,1/2}\Phi^{Q}_{1,2,1/2}\right]$$
$$+\Delta y_1\left[\left(\frac{\widetilde{\Sigma}_{1,2,1}\langle E\rangle_{1,xx}}{\langle\Sigma\rangle_1}-\widetilde{E}_{1,xx,2,1}\right)\Phi^{D}_{1,2,1}-\left(\frac{\widetilde{\Sigma}_{1,1,1}\langle E\rangle_{1,xx}}{\langle\Sigma\rangle_1}-\widetilde{E}_{1,xx,1,1}\right)\Phi^{D}_{1,1,1}\right] \quad (45)$$
$$+\frac{\Delta x_1}{2}\left[\left(\frac{\widetilde{\Sigma}_{1,1,3/2}\langle E\rangle_{1,xy}}{\langle\Sigma\rangle_1}-\widetilde{E}_{1,xy,1,3/2}\right)\Phi^{D}_{1,1,3/2}-\left(\frac{\widetilde{\Sigma}_{1,1,1/2}\langle E\rangle_{1,xy}}{\langle\Sigma\rangle_1}-\widetilde{E}_{1,xy,1,1/2}\right)\Phi^{D}_{1,1,1/2}\right]$$
$$+\frac{\Delta x_2}{2}\left[\left(\frac{\widetilde{\Sigma}_{1,2,3/2}\langle E\rangle_{1,xy}}{\langle\Sigma\rangle_1}-\widetilde{E}_{1,xy,2,3/2}\right)\Phi^{D}_{1,2,3/2}-\left(\frac{\widetilde{\Sigma}_{1,2,1/2}\langle E\rangle_{1,xy}}{\langle\Sigma\rangle_1}-\widetilde{E}_{1,xy,2,1/2}\right)\Phi^{D}_{1,2,1/2}\right]$$

A similar expression can be obtained for y-component of the fast Q current on the surface (i=1, j=3/2):

$$\left(\frac{\Delta y_1+\Delta y_2}{2}\right)\Delta x_1\widetilde{\Sigma}_{1,1,3/2}J^{Q,y}_{1,1,3/2}=-\Delta x_1\left[\widetilde{E}_{1,yy,1,2}\Phi^{Q}_{1,1,2}-\widetilde{E}_{1,yy,1,1}\Phi^{Q}_{1,1,1}\right]$$
$$-\frac{\Delta y_1}{2}\left[\widetilde{E}_{1,xy,3/2,1}\Phi^{Q}_{1,3/2,1}-\widetilde{E}_{1,xy,1,1/2,1}\Phi^{Q}_{1,1/2,1}\right]$$
$$-\frac{\Delta y_2}{2}\left[\widetilde{E}_{1,xy,3/2,2}\Phi^{Q}_{1,3/2,2}-\widetilde{E}_{1,xy,1/2,2}\Phi^{Q}_{1,1/2,2}\right]$$
$$+\Delta x_1\left[\left(\frac{\widetilde{\Sigma}_{1,1,2}\langle E\rangle_{1,yy}}{\langle\Sigma\rangle_1}-\widetilde{E}_{1,yy,1,2}\right)\Phi^{D}_{1,1,2}-\left(\frac{\widetilde{\Sigma}_{1,1,1}\langle E\rangle_{1,yy}}{\langle\Sigma\rangle_1}-\widetilde{E}_{1,yy,1,1}\right)\Phi^{D}_{1,1,1}\right] \quad (46)$$
$$+\frac{\Delta y_1}{2}\left[\left(\frac{\widetilde{\Sigma}_{1,3/2,1}\langle E\rangle_{1,xy}}{\langle\Sigma\rangle_1}-\widetilde{E}_{1,xy,3/2,1}\right)\Phi^{D}_{1,3/2,1}-\left(\frac{\widetilde{\Sigma}_{1,1/2,1}\langle E\rangle_{1,xy}}{\langle\Sigma\rangle_1}-\widetilde{E}_{1,xy,1/2,1}\right)\Phi^{D}_{1,1/2,1}\right]$$
$$+\frac{\Delta y_2}{2}\left[\left(\frac{\widetilde{\Sigma}_{1,3/2,2}\langle E\rangle_{1,xy}}{\langle\Sigma\rangle_1}-\widetilde{E}_{1,xy,3/2,2}\right)\Phi^{D}_{1,3/2,2}-\left(\frac{\widetilde{\Sigma}_{1,1/2,2}\langle E\rangle_{1,xy}}{\langle\Sigma\rangle_1}-\widetilde{E}_{1,xy,1/2,2}\right)\Phi^{D}_{1,1/2,2}\right]$$

The $\widetilde{\Sigma}$'s and $\widetilde{E}$'s in these discretized Q equations are averages over pin cell rows nearest the surface, if their indices are fractional, or averages over subcell volumes if their indices are integers.

Using the subcell surface current definitions, it is possible to formulate a system of equations containing only the subcell surface and subcell average Q fluxes -- a total of 16 unknowns in each node. These equations are solved via a marching method called

"$\mu - \tau - \sigma$" iteration [10], given the previously specified zero-current boundary conditions. These Q problems are "local" in that the Q solution in each node depends only on the within-node D solution – not on Q solutions from neighboring nodes. This means that the additional computational expense to solve the Q equations is very small compared to cost of the D solution.

It is important to remember that, because the D and Q problems are coupled through the fission source, weighted moments of the Q solution will be required to iterate the QDLO equations to convergence. To compute these weighted residuals, we fit the 12 subcell surface and 4 subcell average fluxes to a bi-cubic polynomial, and then use this functional form in the 7 weighted residual equations that constrain the polynomial coefficients of the fast D flux expansion.

7.5 Testing the Nodal Methodology for the "D" Problem

In this section we present the results of a variety of one and multi-node test problems to verify the properties of our nodal discretization of the D equations. We solve several diffusion (diagonal Eddington tensor with diagonal entries equal to 1/3), and "transport" (Eddington tensor with diagonal entries different from one-third and general off-diagonal components) test problems. In the transport problems, the Eddington functionals are chosen to be within the range of values representative of two-node UO_2-MOX fuel assembly transport calculations.

The method provides accurate solutions (multiplication factor k and thermal to fast flux ratio) for one-node, constant cross-section and Eddington tensor component problems, with zero-flux or zero-current boundary conditions.

The two-node problems assume a UO_2-fueled assembly next to a MOX-fueled assembly[2]. This configuration is chosen because UO_2 and MOX have significantly different neutronic properties, so UO_2/MOX systems are excellent for investigating the behavior of neutron fluxes at the surface between unlike assemblies. Zero current boundary conditions are applied to the boundaries of the configurations, as shown in Figure 7.6.

Various configurations are obtained by using UO_2 and MOX fuels of various enrichments in ^{235}U and Pu, respectively.

Table 7.1 shows, in columns 1 to 4, the multiplication factor, UO_2 assembly power and their relative errors from QDLO calculations using the two-group, single assembly cross sections from Table 7.2. These results are compared to CASMO-4 14-group, fine-mesh diffusion calculation results[2] which are reproduced here in columns 5 and 6. In Table 7.1 U_x and M_y stand for x %-enriched UO_2 and y %-enriched MOX.

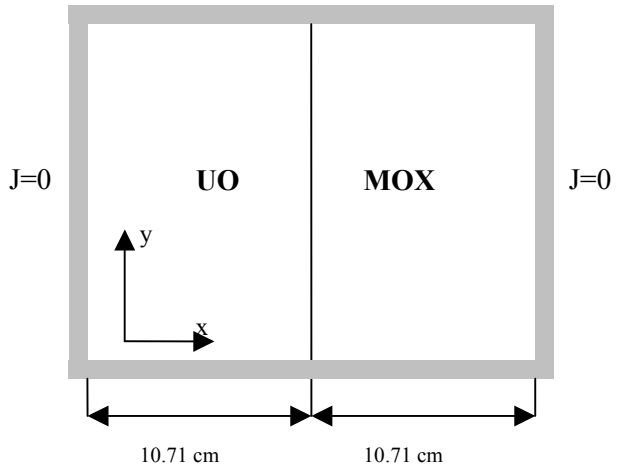

Figure 7.6: UO_2-MOX configuration

The fast and thermal neutron flux shapes for the UO_2 (3%)-MOX (12%) configuration are presented in Figure 7.3 and Figure 7.4, respectively. In both figures, the UO_2 fuel assembly is the closest to the viewer. The fast flux is higher in the MOX assembly, due to its higher fission cross-sections. The steepest variation is observed near the surface between the two assemblies, smoothing out as the reflecting boundaries are approached. The smallest errors occur for the case of two UO_2 assemblies. The thermal flux varies strongly at the surface between nodes mainly due to Σ_{a2}, which is higher in the UO_2 assembly than in the MOX assembly. Better results are obtained if, instead of two-group single-assembly cross-sections, 14-group cross-sections are collapsed to two-group with the actual spectrum[2].

Table 7.1 Two-node UO_2-MOX assembly, multiplication factor and power calculations

Config.	**k**	**Relative error k (%)**	**UO_2 assembly power**	**Relative error (%) UO_2**	**Reference k**	**Reference UO_2 power**
0	**1**	**2**	**3**	**4**	**5**	**6**
U_3/U_4	1.29121	$6.2\text{x}10^{-3}$	0.93167	0.74	1.29113	0.9386
U_4/U_5	1.34542	$2.2\text{x}10^{-3}$	0.93569	2.3	1.34545	0.9580
U_3/U_5	1.31531	$8.4\text{x}10^{-3}$	0.88585	1.2	1.31520	0.8969
U_3/M_8	1.21959	0.2	0.94005	0.9	1.21721	0.9312
U_3/M_{12}	1.23201	0.25	0.90553	0.7	1.22896	0.8986
U_4/M_8	1.25176	0.28	1.01040	1.6	1.24830	0.994
U_4/M_{12}	1.26292	0.32	0.97583	1.5	1.25888	0.9611
U_5/M_8	1.27410	0.3	1.05199	1.5	1.27035	1.0372
U_5/M_{12}	1.28502	0.38	1.02376	2.0	1.28014	1.0042

Table 7.2 Two-group single assembly cross sections

Property	Assembly type					
	UO_2 3%	**UO_2 4%**	**UO_2 5%**	**MOX 4%**	**MOX 8%**	**MOX 12%**
Σ_1	0.286867	0.286714	0.204091	0.286466	0.285875	0.285233
Σ_2	0.97970	0.980551	0.987944	1.07985	1.16774	1.23263
Σ_{12}	0.016756	0.016229	0.015738	0.013630	0.011853	0.010644
Σ_{a1}	0.009530	0.010234	0.010895	0.012956	0.015327	0.017049
Σ_{a2}	0.082606	0.098603	0.113317	0.197823	0.290164	0.350338
$\upsilon\Sigma_{f1}$	0.006758	0.008092	0.009357	0.008436	0.012259	0.015427
$\upsilon\Sigma_{f2}$	0.129545	0.163555	0.194709	0.321278	0.483443	0.587795
k_{inf}	1.256776	1.323053	1.366686	1.149925	1.177585	1.201939

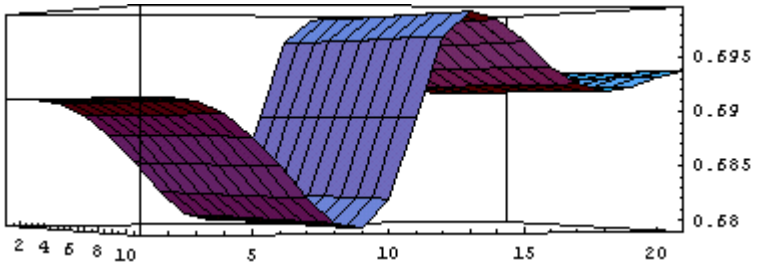

Figure 7.3 Fast neutron flux in UO_2 (3%)-MOX (12%) configuration

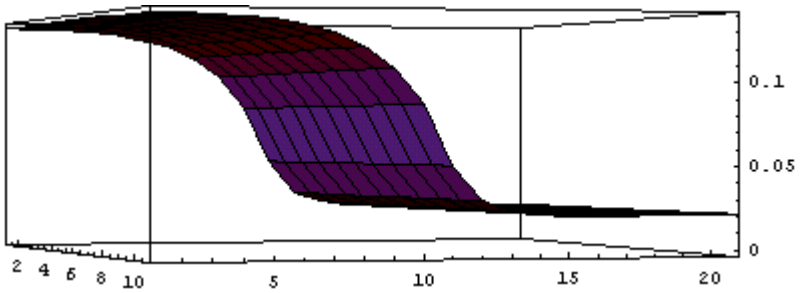

Figure 7.4 Thermal neutron flux in UO_2 (3%)-MOX (12%) configuration

In the multiple-node problems, the k-eigenvalues and power distributions are calculated for configurations of UO_2 (UX), MOX (PX), and water (R) presented in Figure 7.5.

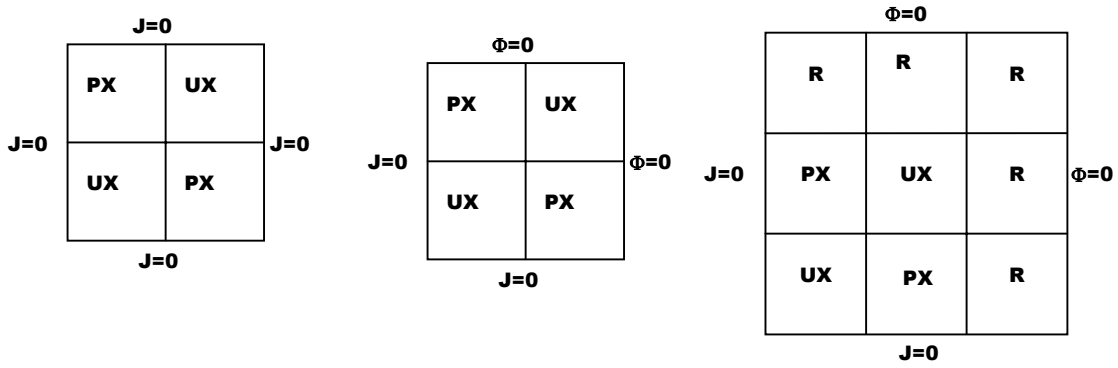

(C1) (C2) (C3)

Figure 7.5 UO_2-MOX (C1, C2) and UO_2-MOX-water (C3) configurations

Cross-section data for these problems come from single assembly NEACRP benchmark calculations (zero-current boundary conditions)[2], and are presented in Table 7.3. Results from QDLO calculations of these problems are shown in Table 7.4, columns 2 through 4. The relative errors, columns 5 through 7, are calculated with respect to reference k-eigenvalues and normalized assembly powers presented in Table 7.5[2] The reference solution (Table 7.5) for each configuration is a 2-D, 2-group, heterogeneous static diffusion calculation performed using one node per fuel pin[2].

Table 7.3 Assembly homogenization results for NEACRP benchmark

Homogenized parameter	**Assembly type**	
	UX	**PX**
$k_{\inf}$	0.998181	1.026669
Σ_1	0.277778	0.277778
Σ_2	0.833333	0.833333
Σ_{a1}	0.009226	0.013791
Σ_{a2}	0.092663	0.231691
$\upsilon\Sigma_{f1}$	0.004570	0.006852
$\upsilon\Sigma_{f2}$	0.113537	0.344583
Σ_{21}	0.020430	0.015864

Table 7.4.1 NEACRP benchmark, homogenized node calculations

Config.	**N**	**k**	**Assembly Power**		**Error (%)**		
			UX	**PX**	**k**	**UX**	**PX**
0	**1**	**2**	**3**	**4**	**5**	**6**	**7**
C_1	60	1.01986	0.87142	1.12860	$7.1\text{x}10^{-2}$	0.37	0.39
C_2	40	0.90831	1.02452	0.97548	0.16	0.39	0.39
C_3	48	0.93904	0.91283	1.0872	0.10	0.36	0.37

Table 7.4.2 NEACRP benchmark, homogenized node calculations, using discontinuity factors

Config.	N	k	Assembly Power		Error (%)		
			UX	PX	k	UX	PX
0	1	2	3	4	5	6	7
C_1	52	1.01927	0.87575	1.12425	$1.3\text{x}10^{-2}$	0.12	0.09
C_2	40	0.90791	1.03012	0.96988	0.12	0.26	0.19
C_3	48	0.93806	0.91842	1.08158	0.05	0.21	0.19

Table 7.5 NEACRP benchmark, homogenized node calculations, reference values

Config.	Reference values [2]		
	k	UX	PX
0	7	8	9
C_1	1.01914	0.8747	1.1253
C_2	0.90685	1.0282	0.9718
C_3	0.93806	0.9165	1.0835

Compared to the two-group, 2-D, static diffusion code STENCIL that uses non-separable polynomial and hyperbolic function expansions [2], the QDLO results from Tables 7.4.1 and 4.2 are reproducing the reference values, Table 7.5, with close or the same accuracy when discontinuity factors are included in QDLO calculations. Palmtag[2] shows also the results produced by other methods (CONQUEST, SIMULATE-3, and PANTHER). QDLO yields results comparable to these other codes for assembly powers, and k-eigenvalues are predicted as accurately as Palmtag's STENCIL code.

In the QD problem with realistic Eddington tensor components we consider a 4-node domain with semi-reflecting boundaries as shown in Figure 7.6. Each node corresponds to a fuel assembly, all assemblies being identical.

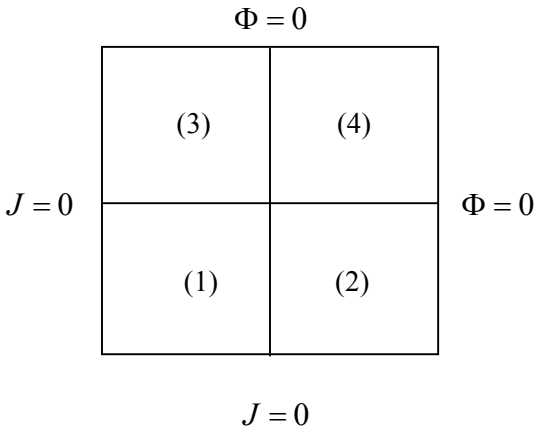

Figure 7.6 Semi-reflecting boundaries, four-node problem

The multiplication factor k of this configuration is calculated by using the nodal QDLO methodology for $E^{ij}_{g,xx} = E^{ij}_{g,yy}$ from 0.30 to 0.36 and $E^{ij}_{g,xy} = E^{ij}_{g,yx}$ from 0.0 to 0.04. Cross-sections are the ones in Table 7.3, for PX assemblies. The results show that k decreases when Eddington functionals increase. This behavior is due to increased leakage, directly related to bigger functional values. The calculated values for k and the dependence of k on **E** are shown in Table 7.6 and Figure 7.7.

Table 7.6 Calculated multiplication factors for various Eddington functionals

E^{ij}_{gxy}	$E^{ij}_{gxx} = E^{ij}_{gyy}$			
	0.30	0.32	0.34	0.36
0.00	0.928595	0.922699	0.916875	0.911121
0.01	0.927200	0.921318	0.915508	0.909769
0.02	0.925912	0.920036	0.914233	0.908502
0.03	0.924729	0.918852	0.913050	0.907321
0.04	0.923653	0.917766	0.911958	0.906225

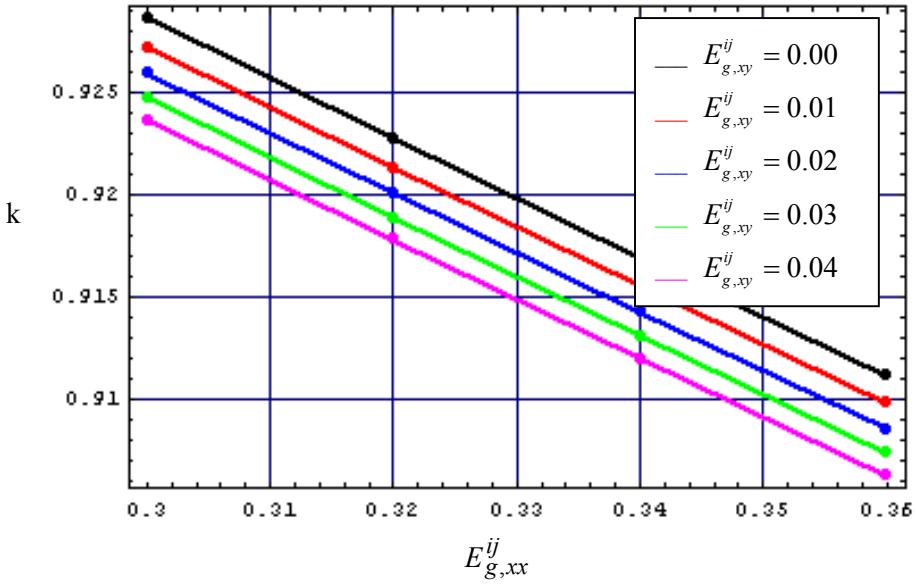

Figure 7.7 Multiplication factor versus diagonal components at various values of off-diagonal components of Eddington tensor

Increased off-diagonal Eddington tensor components also affect the power distribution between nodes by enhancing the flow of neutrons towards certain nodes. For example in our problem the power in node 4 increases with increasing $E^{ij}_{g,xy}$, while power in nodes 1, 2 and 3 decreases. Table 7.7 summarizes these results, showing the variation of node-averaged, normalized power (P) and its rate of variation $\left(\frac{dP}{dE^{ij}_{g,xy}}\right)$. In Figure 7.8 node averaged power is plotted against off-diagonal Eddington functionals.

Table 7.7 The effect of off-diagonal Eddington tensor components on the power distribution

$E^{ij}_{g,xy}$	Node 1		Node 2, 3		Node 4	
	P	$\frac{dP}{dE^{ij}_{g,xy}}$	P	$\frac{dP}{dE^{ij}_{g,xy}}$	P	$\frac{dP}{dE^{ij}_{g,xy}}$
0.00	0.28215	-0.4065	0.11687	-0.1465	0.48410	0.6965
0.01	0.27818	-0.3855	0.11541	-0.1450	0.49098	0.6805
0.02	0.27440	-0.3705	0.11396	-0.1455	0.49769	0.6600
0.03	0.27077	-0.3555	0.11251	-0.1445	0.50421	0.6440
0.04	0.26729	-0.3405	0.11107	-0.1435	0.51057	0.6280

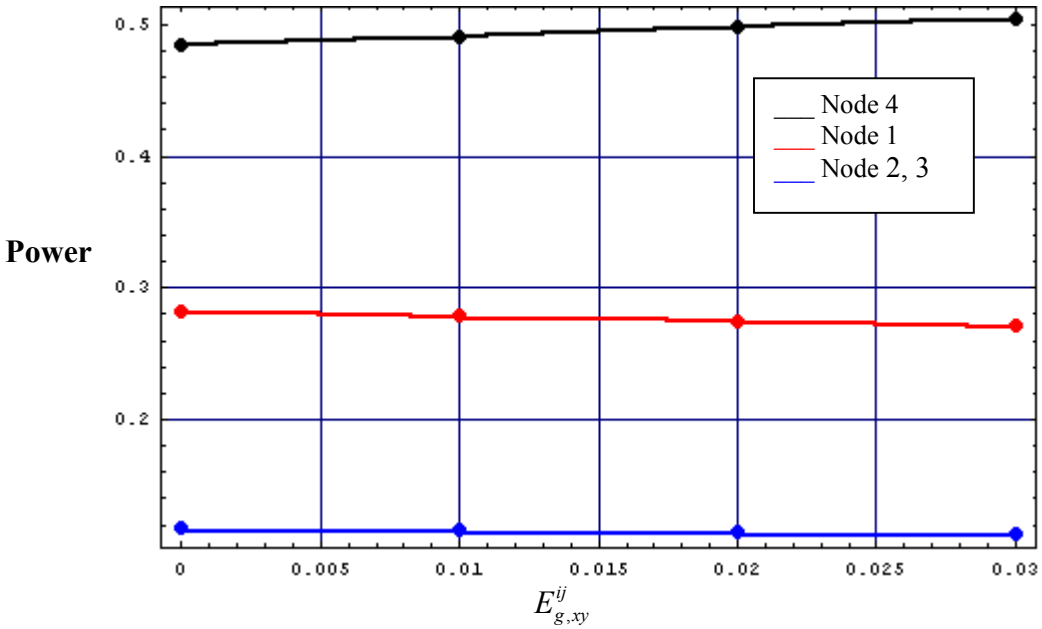

Figure7. 8 Node-averaged power versus off-diagonal Eddington tensor elements

7.6 Testing the Coupled Methodology

Our ongoing (and future) work is focused on the testing of a FORTRAN code that incorporates the previously described methodology to solve the coupled D and Q problems. At this time, we are debugging the code for the calculation of the discontinuity factors, and our plan is to have a working code for global reactor core calculations by September 1, 2003. We will extensively test the full methodology on a variety of four node (node = quarter assembly) problems. Results of this testing will be presented at the 2004 PHYSOR Topical Meeting in Chicago in April, 2004.

Initially, we will be using Eddington functionals and cross-section data from a transport calculation that contains the correctly represents neighboring fuel assemblies. These

calculations will contain the most accurate eigenvalue and power density predictions our methodology can produce, given the absence of tabular interpolation on neighbor type. In current reactor methodologies, single assembly transport calculations are performed for a variety of conditions the fuel assembly will experience over its in-core life. These cross sections (and other data) are then parameterized as a function of the conditions (void fraction, fuel and moderator temperature, exposure, boron concentration, control rod insertion, etc.) to allow for quick calculation of nodal data in the global code. This parameterization introduces an error into the global calculation. We will also test the accuracy of our methodology given the parameterization of the assembly data.

References

1. D.Y. Anistratov, M.L. Adams, T.S. Palmer, K.S. Smith, "An Innovative Reactor Analysis Methodology Based on a Quasidiffusion Nodal Core Model", *DOE NERI Proposal* (1999).

2. S.Palmtag, "Advanced Nodal Methods for MOX Fuel Analysis", PhD Thesis, MIT (1997)

3. V.Ya. Goldin, "A Quasi-Diffusion Method of Solving the Kinetic Equation ", *USSR Comp. Math. and Math. Phys.*, **4**, pp.136-149 (1967)

4. Adams, M.L. and Larsen, E.W., "Fast Iterative Methods for Discrete Ordinates Particle Transport Calculations", *Progress in Nuclear Energy*, **40**, No.1, pp 3-159 (2002)

5. M.M. Miften, E.W.Larsen, "A Symmetrized Quasidiffusion Method for Solving Transport Problems in Multidimensional Geometries", *Joint International Conference on Mathematical Methods and Supercomputing in Nuclear Applications*, Karlsruhe, 19-23 April, Germany, Vol.1,pp. 702-711 (1993)

6. Rade, L. and Westergren, B., "*Beta Mathematics Handbook*", CRC Press, Boca Raton US (1992)

7. S.Wolfram, "*Mathematica, A System for Doing Mathematics by Computer*", Second Edition, Addison-Wesley (1991)

8. Hiruta, H., Anistratov, D.Y. and Adams, M.L., "Splitting Method for Solving the Coarse-Mesh Discretized Low-Order Quasidiffusion Equations," *Proc. of the ANS Topical Meeting on Nuclear Mathematical and Computational Sciences: A Century in Review, A Century Anew*, Gatlinburg, TN, April 6-11, 2003.

9. Anistratov, D.Y., private communication (2003).

10. Gol'din, V.Y. and Kolpakov, A.V., "Nonlinear Marching Method for Solving the Multidimensional Diffusion Equation," Preprint of the Keldysh Institute for Applied Mathematics, the USSR Academy of Sciences, No. 22 (1982) (in Russian).

11. Anistratov, D.Y., private communication (2003).